1 SEPTEMBER 2025

TU Delft

AERODYNAMICS OF A VERTICAL-AXIS WIND TURBINE BLADE IN SINUSOIDAL INFLOW CONDITIONS

AN EXPERIMENTAL INVESTIGATION

1
Characterization of the Wind Tunnel at the DCSC Lab

2
Design and Construction of a Vertical-Axis Wind Turbine (VAWT)

3
Experimental Analysis of Wave Effects on Turbine Efficiency

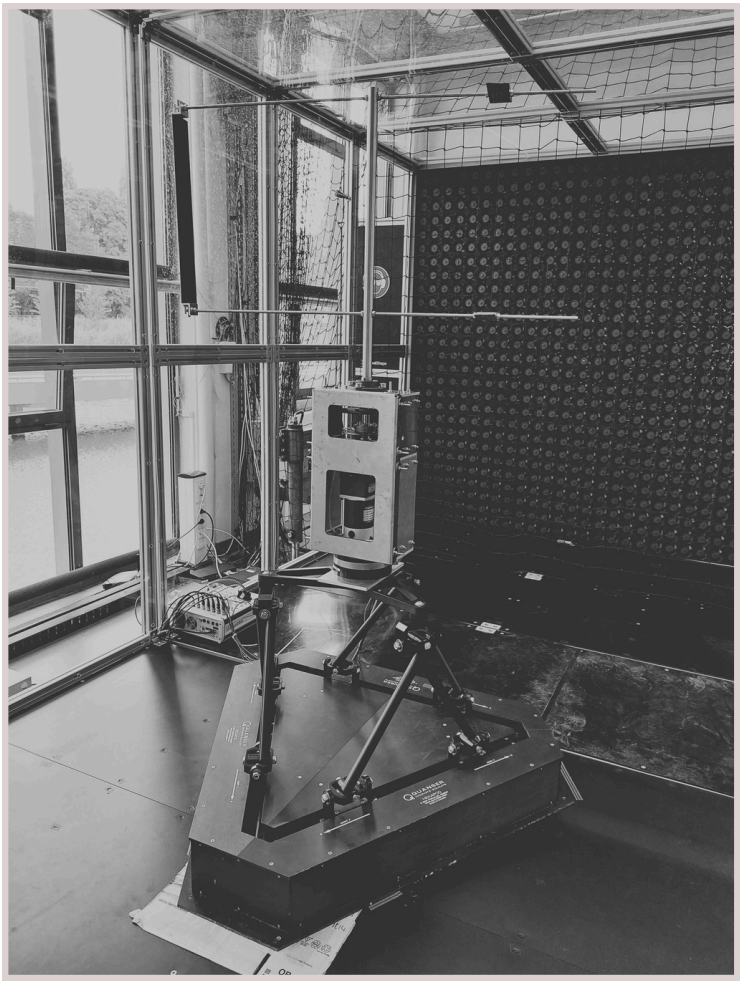

Author:
Milo de Leeuw

Master's Student, Faculty of Mechanical Engineering

Supervisor:
Dr. A.J.L.L. Buchner

Master Thesis

Department of Mechanical Engineering

Aerodynamics of a Vertical-Axis Wind Turbine Blade in Sinusoidal Inflow Conditions

An Experimental Investigation

Author:	Milo de Leeuw
Student Number:	4885910
Supervisor:	Dr. A.J.L.L. Buchner
Thesis Committee:	Prof.dr.ir. J. Westerweel (Chair)
	Prof.dr. K. Hooman
	Dr. A.J.L.L. Buchner
	PhD candidate T.J. Crumpton

To be defended: 15 September 2025

TU Delft

Abstract

Climate change motivates the transition from fossil fuels to low-carbon energy sources, and wind power is a key option. Among wind-energy technologies, vertical-axis wind turbines (VAWTs) offer advantages for offshore and urban applications due to their omnidirectional wind acceptance and simpler structural requirements. In offshore floating platforms, the motion of the structure can induce periodic variations in the apparent wind velocity, which may influence turbine performance. This thesis also investigates whether such periodic (sinusoidal) wind velocities can alter the energy production of VAWTs, and examines the influence of the tip-speed ratio (λ), the dimensionless wind-velocity amplitude (A^*), and the dimensionless wind-velocity frequency (ω^*) on these effects, without seeking their optimization.

The work follows three stages: (1) characterization of the wind-tunnel test section, (2) design and construction of a single-bladed H-Darrieus VAWT with adjustable solidity, and (3) wind-tunnel experiments under steady and sinusoidal inflow conditions. Because the tunnel could not reliably reproduce the desired sinusoidal profiles, a hexapod was used to oscillate the turbine and simulate unsteady inflow. Measurements show that periodic inflow induces phase-dependent blade loading and subtle torque fluctuations, but produces no statistically significant increase in period-averaged power. Efficiency remained primarily controlled by λ, with only minor, inconclusive deviations near peak operating conditions due to ω^*. Recommendations include utilizing a low-turbulence-intensity wind tunnel, employing precision-aligned bearings, and conducting tests at higher tip speed ratios ($\lambda > 3.0$) to better resolve potential unsteady effects.

Acknowledgements

I would like to thank **Dr. A.J.L.L. Buchner** for his supervision of this thesis, and **T.J. Crumpton** for his valuable insights during discussions.

I am also grateful to the **DCSC** and **EFPT** laboratories for their contributions to bringing the turbine to life.

In particular, I want to acknowledge **W.J.M. van Geest**, **W.H.A. Wien**, **R.J.M. Willekes**, **Jasper Ruijgrok**, and **GertJan Mulder** for their support and efforts.

Finally, I would like to thank my parents and my close friends for making this life so wonderful.

Contents

Nomenclature

Greek Symbols / Dimensionless Numbers

α	Angle of Attack [°]
θ	Azimuthal Angle [°]
λ	Tip Speed Ratio [-]
$\bar{\tau}$	Average Aerodynamic Torque [Nm]
ν	Kinematic Viscosity of the Air [m^2/s]
ρ	Density of Air [kg/m^3]
σ	Solidity Ratio [-]
ω^*	Frequency Ratio [-]
A^*	Freestream Variation Amplitude [-]
v_i	Freestream Variation Amplitude [-]
Re	Reynolds Number [-]
$C_D(\alpha)$	Drag Coefficient of the Blade [-]
$C_L(\alpha)$	Lift Coefficient of the Blade [-]

Physical Quantities

A	Blade Area [m^2]
L	Chord Length of the Airfoil [m]
R	Rotor Radius [m]
C_p	Power Coefficient [-]
Ω	Rotational speed [rad/s]
RPM	Revolutions per Minute

Forces

F Aerodynamic Force Acting on the Turbine [N]

F_D Drag Force Acting on the Blade [N]

F_L Lift Force Acting on the Blade [N]

F_N Normal Force Acting on the Blade [N]

F_T Tangential Force Acting on the Blade [N]

Velocities / Flow Properties

U_∞ Wind velocity approaching the turbine [m/s]

U_{rel} Relative Velocity [m/s]

$\bar{U}$ Average Velocity of the Oncoming Wind [m/s]

Acronyms / Facilities / Methods

CAD Computer-Aided Design

CFD Computational Fluid Dynamics

DCSC Delft Centre for Systems and Control

HAWT Horizontal-Axis Wind Turbines

VAWT Vertical-Axis Wind Turbines

LDA Laser Doppler Anemometry

PIV Particle Image Velocimetry

RMS Root Mean Square

SEM Standard Error of the Mean

TI Turbulence Intensity

List of Figures

List of Tables

1. Introduction

In 2024, one of the most devastating storms in recent years struck the Valencia region in Spain, resulting in 229 fatalities and widespread destruction [1]. The rainfall was about 12% heavier and twice as likely compared to the 1.3°C cooler preindustrial climate [2], highlighting that climate change poses one of the greatest challenges to humanity today. The primary driver of this climate change is the burning of fossil fuels (coal, oil, and gas) which account for over 75% of global greenhouse gas emissions and nearly 90% of all carbon dioxide emissions [3].

Wind energy has emerged as a promising alternative, preventing up to 1100 million tons of CO_2 emissions annually [4]. Two main types of wind turbines dominate the field: Horizontal-Axis Wind Turbines (HAWTs) and Vertical-Axis Wind Turbines (VAWTs). See Figure 1.1 for a comparison. HAWTs extract energy by aligning their rotor with the wind direction using complex yaw mechanisms, whereas VAWTs operate independently of wind direction due to their vertical design. This design simplicity eliminates the need for yaw systems, reducing maintenance costs and increasing robustness in turbulent or multidirectional wind [5].

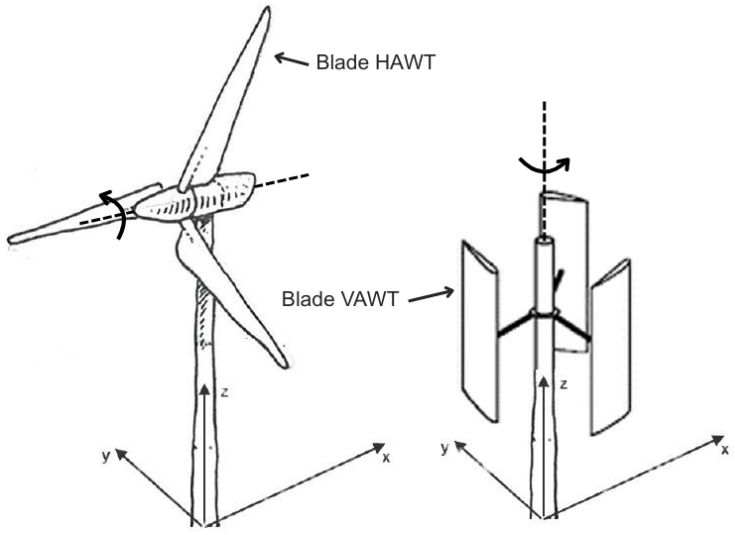

Figure 1.1: Comparison of a HAWT (left) and a VAWT (right), from [6]. The HAWT uses a yaw mechanism to align with the incoming wind, assumed to flow along the positive x-direction. In contrast, the VAWT operates independently of wind direction due to its vertical rotor axis, with H-Darrieus blades attached as a common configuration. Stippled lines indicate the rotation axes, arrows show the rotational direction.

Despite their mechanical simplicity and robustness, VAWTs face significant aerodynamic and structural challenges. The continuous variation in blade angle of attack leads to fluctuating aerodynamic loads, which over time can cause structural fatigue [5]. These fluctuations also reduce aerodynamic efficiency compared to HAWTs under steady wind conditions [7], partly due to dynamic stall. Together, these aerodynamic and structural issues limit the widespread adoption of VAWTs. Understanding and controlling these unsteady characteristics is therefore crucial to improving efficiency and reducing structural fatigue.

A promising approach to enhance VAWT efficiency involves studying their response to sinusoidal wind patterns. In offshore environments, the rocking motions of floating platforms cause the turbine to move relative to the wind, creating an apparent temporal variation in wind speed from the turbine's frame of reference, even though the ambient wind speed remains constant. These unsteady conditions could potentially enable VAWTs to harness additional energy by synchronizing their rotational speed with wind fluctuations.

Recent experiments on HAWTs have investigated the effect of sinusoidal motion by physically moving the turbine platform forward and backward to simulate surge conditions (oscillatory motion in the direction of the incoming wind); see Figure 1.2. Under these conditions, a period-averaged power increase of up to 6.4% was observed at high tip-speed ratios [8]. Whether similar gains can be achieved with VAWTs remains an open question.

To date, few studies have examined the impact of periodic wind speed fluctuations on VAWT performance under controlled laboratory conditions. This study addresses that gap by investigating the following research question:

> *How do periodic wind velocities impact the energy output of vertical-axis wind turbines, and how can this be optimized using the tip speed ratio (λ)?*

To explore this question, three main steps were taken: (1) characterizing the wind conditions in the Windshape test facility at TU Delft, (2) designing and constructing a single-bladed vertical-axis wind turbine (VAWT) for wind tunnel experiments, and (3) evaluating its performance under both steady and sinusoidal inflow conditions.

The thesis is structured as follows: section 2 presents the theoretical background. A detailed literature review relevant to each goal is provided in section 3. The characterization of the WindAI facility's nominal test section is described in section 4. The turbine design process is detailed in section 5, followed by the experimental setup and sinusoidal wind experiments in section 6. Finally, section 7 presents the overall conclusions and final remarks of the thesis.

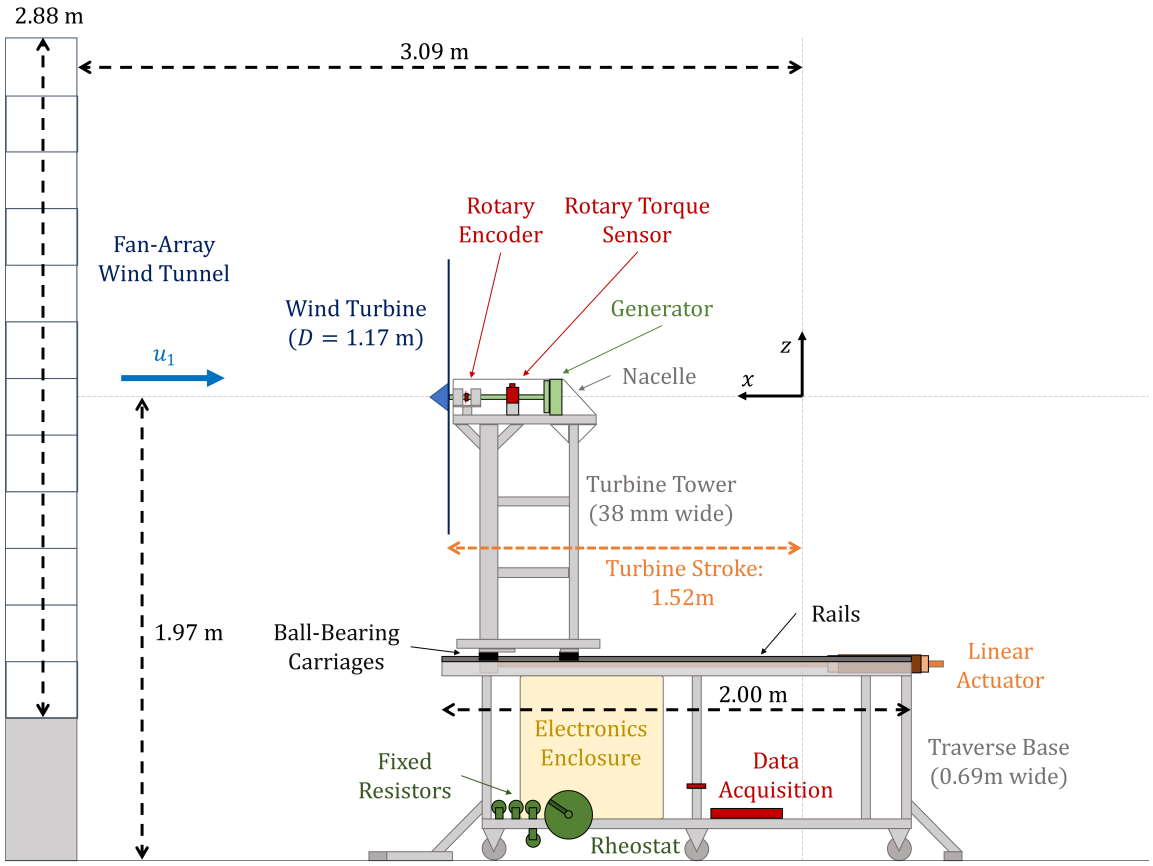

Figure 1.2: Illustration of the experimental setup used by Wei and Dabiri [8], where a horizontal-axis wind turbine was moved forward and backward along rails to simulate periodically surging wind.

2. Basic Theory and Principles

Building on the motivation outlined in the introduction, this section presents the fundamental concepts necessary to understand wind energy conversion and turbine operation. It compares Horizontal- and Vertical-Axis Wind Turbines (HAWT & VAWT), focusing on the H-Darrieus VAWT as the subject of this study. Additionally, a review of historical research on VAWT aerodynamics and control strategies provides context and highlights the gaps this work aims to address.

2.1 Fundamentals of Wind Energy Extraction

At its core, a wind turbine functions by converting the kinetic energy of moving air into mechanical energy, which can then be transformed into electricity. This energy conversion process involves several key stages:

1. **Kinetic Energy of Wind**
   It all starts with wind: moving air that contains kinetic energy, which depends on the air's density and velocity. The power available in the wind increases with the cube of its velocity and is given by:

$$P_{\text{wind}} = \frac{1}{2}\rho A U_\infty^3 \tag{1}$$

   where ρ is air density, A the swept area, and U_∞ the oncoming wind speed [9].

2. **Energy Capture by the Rotor Blades**
   This kinetic energy is captured by the specially designed rotor blades of a wind turbine (see Figure 1.1). As wind flows over the airfoil-shaped blades, the blade geometry and angle of attack alter the airflow, producing a pressure difference between the upper and lower surfaces. This pressure difference manifests as a lift force perpendicular to the relative wind direction. The tangential component of this aerodynamic force drives blade rotation. Many turbines operate primarily based on aerodynamic lift, the same principle that enables airplanes to fly. While pressure differences dominate the force generation, viscous drag effects also influence blade performance, particularly near the surface and at low Reynolds numbers, but are generally less significant for large-scale turbines. This is because higher Reynolds numbers reduce the relative impact of viscous forces compared to inertial forces in large turbines. Blade design, especially shape and angle of attack, is critical for maximizing energy capture because these factors control the aerodynamic forces that drive rotation and influence efficiency and stability.

However, not all wind turbines rely on lift; some utilize drag forces to generate power. A notable example is the Savonius rotor, a type of VAWT with an S-shaped cross-section that primarily operates on drag principles (see Figure 2.3). Its blades experience a large pressure difference between the concave and convex sides as they interact with the wind, producing torque primarily through form drag (pressure drag) rather than aerodynamic lift. While some lift is generated, its contribution is minor compared to drag. As a result, Savonius rotors generally achieve lower efficiencies than lift-driven turbines [10], since drag-based operation inherently involves stronger resistive forces opposing rotation, limiting torque production and reducing overall efficiency.

3. **Mechanical Energy Conversion**
   The captured energy spins the rotor blades, turning a shaft connected to a generator housed within the turbine casing. This motion transfers mechanical energy from the rotating shaft to the generator.

4. **Generation of Electricity**
   The generator converts mechanical energy from the turbine into electrical energy through electromagnetic induction, where the rotation of the rotor induces an electrical current in the coils [10]. This electrical energy can then be utilized as an alternative to fossil fuels.

While the conversion of wind energy into electricity is conceptually straightforward, the efficiency of this process is fundamentally constrained by aerodynamic principles. In particular, the efficiency of wind turbines is constrained by the Betz limit, which states that no turbine can extract more than 59.3% of the wind's kinetic energy. This limit is based on the conservation of mass and momentum in the airflow, demonstrating that extracting more energy would excessively slow the wind and reduce the flow through the rotor, thereby limiting power generation [11]. For a detailed derivation and discussion, see Blackwood [12].

2.2 Horizontal-Axis Wind Turbines (HAWT)

Having introduced the basic aerodynamic principles, we now turn to a more detailed discussion of turbine designs, beginning with HAWTs. These turbines orient their rotors to face the prevailing wind and generate torque primarily through aerodynamic lift. To maintain this orientation as wind direction changes, they employ yaw mechanisms that continuously adjust the turbine to face the wind.

HAWT blades generate lift by following classical airfoil theory. Unlike aircraft wings, the blade's shape and geometry vary along its length to optimize torque production. Lift results from pressure differences across the blade surfaces, arising from the circulation of airflow around the blade, and can be described using aerodynamic models such as lifting line theory [13]. The relative wind experienced by each blade combines the oncoming wind and the blade's rotational motion, and the resulting aerodynamic forces produce the torque that drives the turbine.

The orientation of the blade relative to this airflow is described by the angle of attack, defined as the angle between the chord line (the straight line connecting the leading and trailing edges of the airfoil) and the direction of the relative wind. This angle is crucial in determining the amount of lift and drag generated. Together with a drag component, the lift creates a net aerodynamic force that acts through the center of pressure, generating a torque that drives blade rotation, as illustrated in Figure 2.1

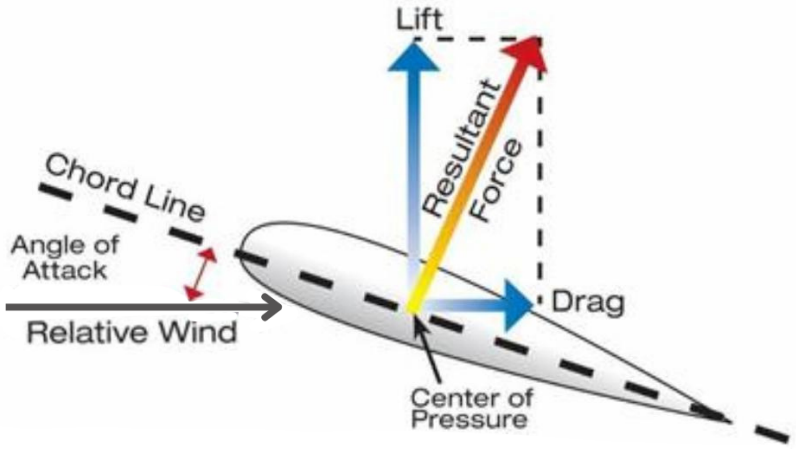

Figure 2.1: Aerodynamic forces on an airfoil. Lift and drag arise from pressure differences across the surfaces. The chord line, angle of attack (between the chord and the relative wind), and center of pressure are also shown. (Adapted from [14])

.

This variation directly influences the power coefficient (C_p), a key metric used to evaluate the efficiency of a wind turbine in converting wind energy into usable power. The power coefficient is defined as:

$$C_p = \frac{\text{Output Power}}{\text{Available Wind Power}} = \frac{P}{\frac{1}{2}\rho A_{area} U_\infty^3} \tag{2}$$

where P is the mechanical power output, ρ is the air density, A_{area} is the rotor swept area, and U_∞ is the freestream wind velocity. Other metrics include the

torque coefficient, which describes torque relative to wind conditions; the thrust coefficient, representing the axial force on the rotor; and the capacity factor, which measures actual versus maximum energy output over time. The power coefficient is preferred for assessing aerodynamic efficiency because it directly relates power output to available wind power, while the other metrics focus on mechanical loads or long-term performance.

To better understand turbine efficiency, researchers analyze the power coefficient with respect to the tip speed ratio (λ) because the tip speed ratio critically influences aerodynamic performance and energy capture [15]. The tip speed ratio is defined as the ratio of the blade tip velocity to the wind velocity:

$$\lambda = \frac{\text{Speed of the tip of the blade}}{\text{Speed of the wind}} = \frac{\Omega R}{U_\infty} \tag{3}$$

Here, Ω is the rotational speed, R is the rotor radius. The power coefficient indicates how efficiently a wind turbine converts wind energy into mechanical energy. Figure 2.2 illustrates the relationship between the power coefficient and the tip speed ratio for different turbine designs.

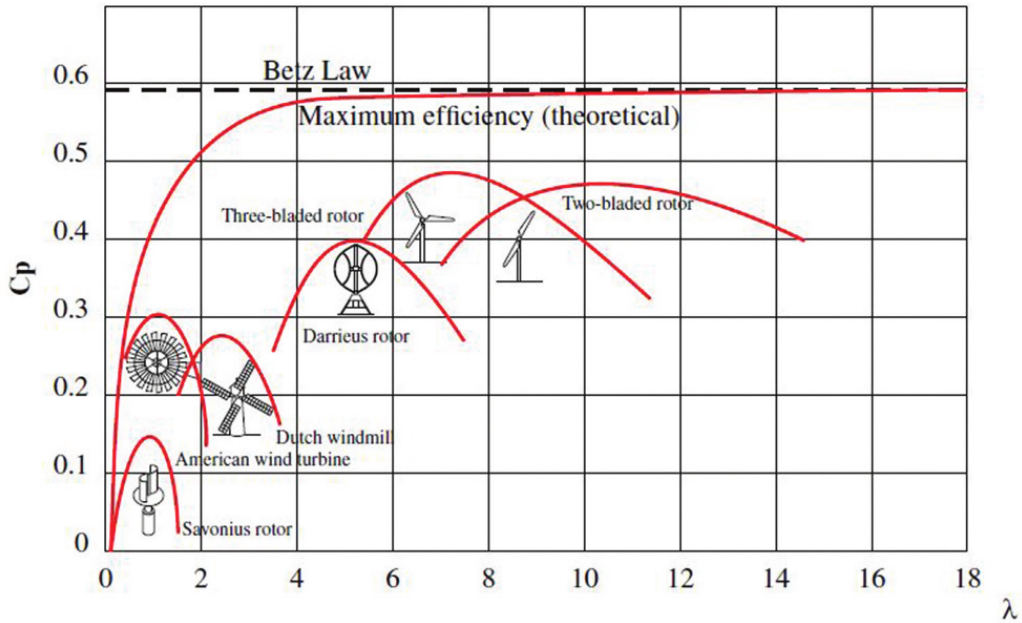

Figure 2.2: Power coefficient (C_p) versus tip speed ratio (λ) for different wind turbine designs. The Darrieus rotor, a lift-based VAWT, is included alongside HAWTs, which typically achieve performance closest to the Betz limit. The Savonius rotor, a drag-based vertical-axis wind turbine (VAWT), is also shown. Data adapted from Pujari et al. [16], referencing Wood [7].

2.3 Vertical-Axis Wind Turbines (VAWT)

Having introduced Horizontal-Axis Wind Turbines and their performance characteristics, the focus now shifts to Vertical-Axis Wind Turbines. This section discusses the reasons for selecting VAWT over HAWT, compares their advantages and limitations, and then explains the operating principles of the chosen VAWT design.

2.3.1 Rationale for Choosing Vertical-Axis Wind Turbines

Although VAWTs are generally less efficient than HAWTs (see Figure 2.2), they offer several distinct advantages for oceanic applications. Traditional offshore wind typically refers to installations in shallower waters (e.g., the North Sea), where monopile foundations and HAWTs dominate. In contrast, oceanic or deep-water environments require floating platforms. The benefits of VAWTs in these challenging settings include:

- *Omni-directional capabilities*: VAWTs can capture wind from any direction, eliminating the need for a yaw mechanism. This is particularly useful in areas with fluctuating wind and a 6 degrees of freedom (6 DOF) inflow problem caused by waves and currents [17], such as oceanic environments [18].

- *Lower manufacturing costs*: VAWTs have simpler designs, reducing production costs compared to HAWTs [5]. They also require less maintenance, leading to lower operational costs [19], but blade fatigue from unsteady aerodynamic forces (see Figure 2.6) remains a key challenge also for maintenance.

- *Reduced noise emissions*: VAWTs are known to produce lower noise levels compared to HAWTs [19], which can contribute to a less disruptive environment for oceanic wildlife.

- *Higher power density in compact arrangements*: Dabiri [20] demonstrated that counter-rotating VAWT arrays can achieve significantly higher power densities compared to traditional HAWT farms. This increase is attributed to advantageous interactions between turbine wakes, which can enhance the performance of downstream turbines. Specifically, field tests showed that VAWT arrays can produce power densities ranging from 21 to 47 $\mathrm{W/m^2}$, an order of magnitude greater than the 2–3 $\mathrm{W/m^2}$ typical of HAWT farms.

2.3.2 Selection of the H-Darrieus Design

Having established the advantages of VAWTs, the next step is to identify a specific configuration suitable for experimental investigation. Various VAWT designs exist, as illustrated in Figure 2.3. On the left is a Savonius turbine, which harnesses wind energy using scooped blades that rely primarily on drag forces acting on their concave surfaces (see Section 2.1). The middle and right designs represent variations of the Darrieus turbine, which operates using aerodynamic lift forces. These lift-based designs are capable of achieving higher efficiencies, as shown in Figure 2.2.

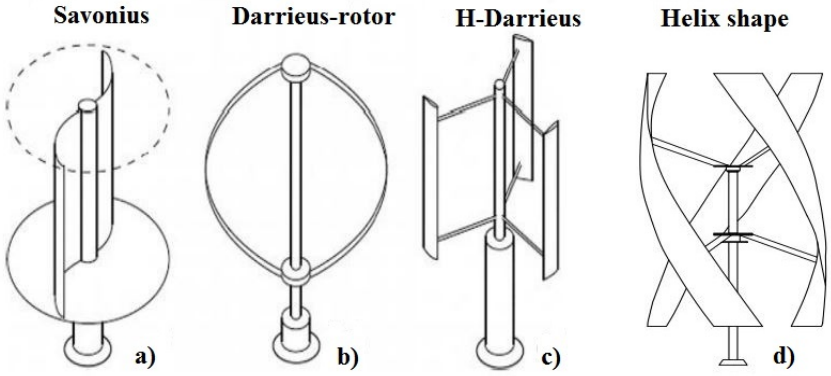

Figure 2.3: Examples of VAWT designs [21]. Left: Savonius Turbine; Middle and Right: Variations of Darrieus Turbines.

For this research, a Darrieus turbine was selected due to its superior efficiency compared to the Savonius type (Figure 2.2), and therefore greater potential for eventual practical application. Among the Darrieus configurations, the H-type was chosen for its structural simplicity [22], which facilitates construction and makes it especially suitable for experimentally investigating the effects of sinusoidal wind patterns on turbine performance.

2.3.3 Operating Principles of the H-Darrieus VAWT

Understanding energy extraction in H-Darrieus VAWTs (inspired by [23], [24]) requires examining the velocity components acting on a rotating blade. Figure 2.4 shows the key velocities for an H-Darrieus VAWT blade section. The free-stream wind velocity is given by U_∞, while blade rotation introduces a tangential velocity

$$U_{\text{tip}} = \Omega R, \tag{4}$$

where Ω is the angular velocity of the rotor (in radians per second), and R is the rotor radius (the distance from the center of rotation to the blade tip). In the blade's rotating reference frame, this velocity appears as $-\vec{U}_{\text{tip}}$, opposing the direction of rotation. The vector sum of U_∞ and $-\vec{U}_{\text{tip}}$ yields the blade-relative velocity $\vec{U}_{\text{rel}}$, which governs the aerodynamic forces on the blade.

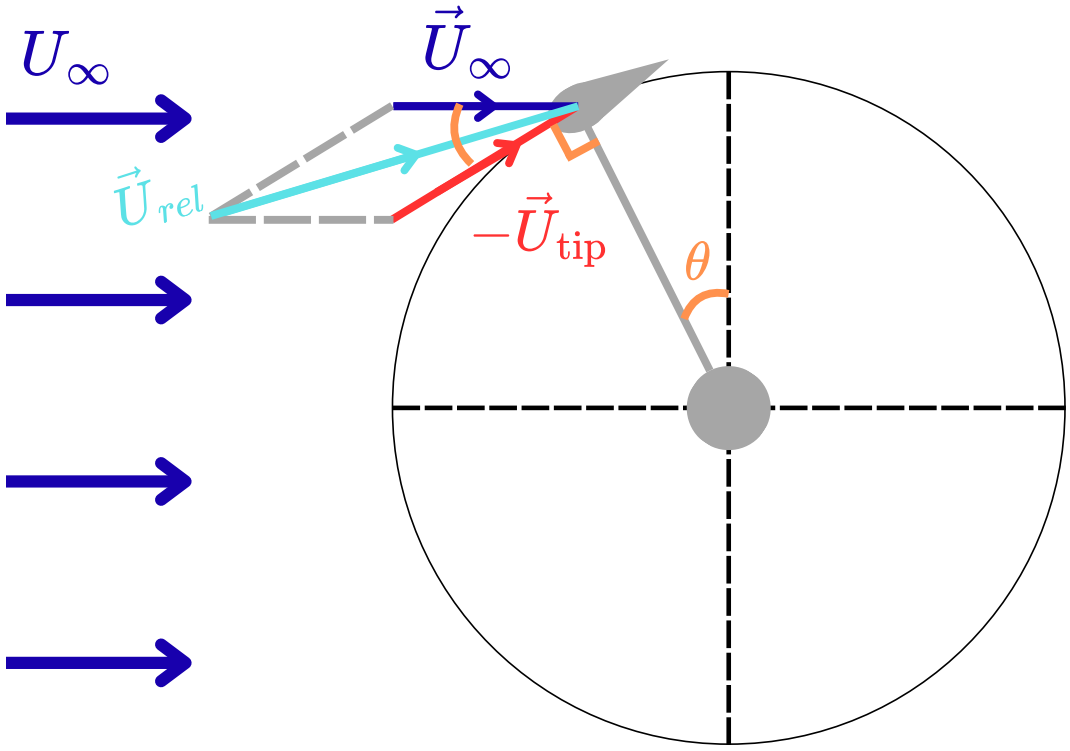

Figure 2.4: The azimuthal angle (θ) denotes the blade's position along its circular path, measured from a fixed reference (usually the upwind direction). At each θ, the free-stream velocity ($\vec{U}_\infty$) combines with the changing rotational tip velocity ($\vec{U}_{tip}$) to form the relative velocity ($\vec{U}_{rel}$) acting on the blade. This changing velocity geometry drives the periodic variation in aerodynamic forces characteristic of VAWTs.

The free-stream velocity $\vec{U}_\infty$ can be decomposed into two orthogonal components: a normal component $U_{\infty,n} = U_\infty \sin\theta$ and a tangential component $U_{\infty,t} = U_\infty \cos\theta$, where θ is the blade's azimuthal angle (Figure 2.5, left). These components, together with the tip velocity, form a triangle from which both the angle of attack α_{rel} and the relative velocity magnitude U_{rel} can be geometrically determined (Figure 2.5, right).

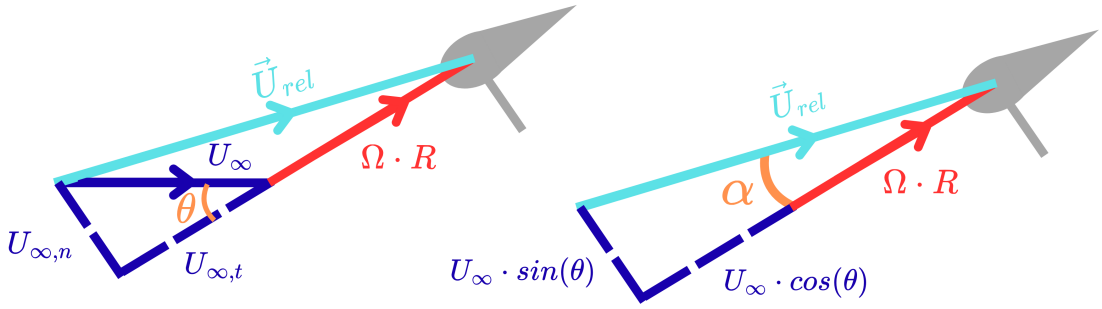

$$\alpha = tan^{-1}\left(\frac{U_\infty sin(\theta)}{\Omega \cdot R + U_\infty cos(\theta)}\right) = tan^{-1}\left(\frac{sin(\theta)}{\frac{\Omega \cdot R}{U_\infty} + cos(\theta)}\right) = tan^{-1}\left(\frac{sin(\theta)}{\lambda + cos(\theta)}\right) \quad (5)$$

$$U_{rel} = U_{inf}\sqrt{(\lambda + cos\theta)^2 + sin^2\theta} \quad (6)$$

Figure 2.5: Derivation of the relative velocity and angle of attack from velocity components. Left: Decomposition of U_∞ into tangential and normal components. Right: Construction of the relative velocity vector U_{rel} and the resulting angle of attack α. The equations below define both α and the magnitude of U_{rel}.

The theoretical angle of attack and relative velocity experienced by a VAWT blade are shown in Figure 2.6, respectively. These plots highlight key reasons for VAWTs' generally lower efficiency compared to HAWTs:

1. **Cyclic Angle of Attack (α) Variation**: As seen in the top of Figure 2.6, VAWT blades experience a wide and rapidly changing angle of attack over a revolution. Unlike HAWTs, which maintain a more constant and optimal α, VAWT blades operate at suboptimal angles, often entering stall, which reduces average aerodynamic efficiency.

2. **Varying Relative Velocity ($U_{\mathbf{rel}}$)**: Bottom of Figure 2.6 demonstrates significant fluctuations in U_{rel}. Notably, on the downwind side (around $\theta = 180°$), U_{rel} drops considerably (to zero for $\lambda = 1$). This period of reduced effective wind speed means less kinetic energy is available for conversion to power, as power is proportional to U_{rel}^3.

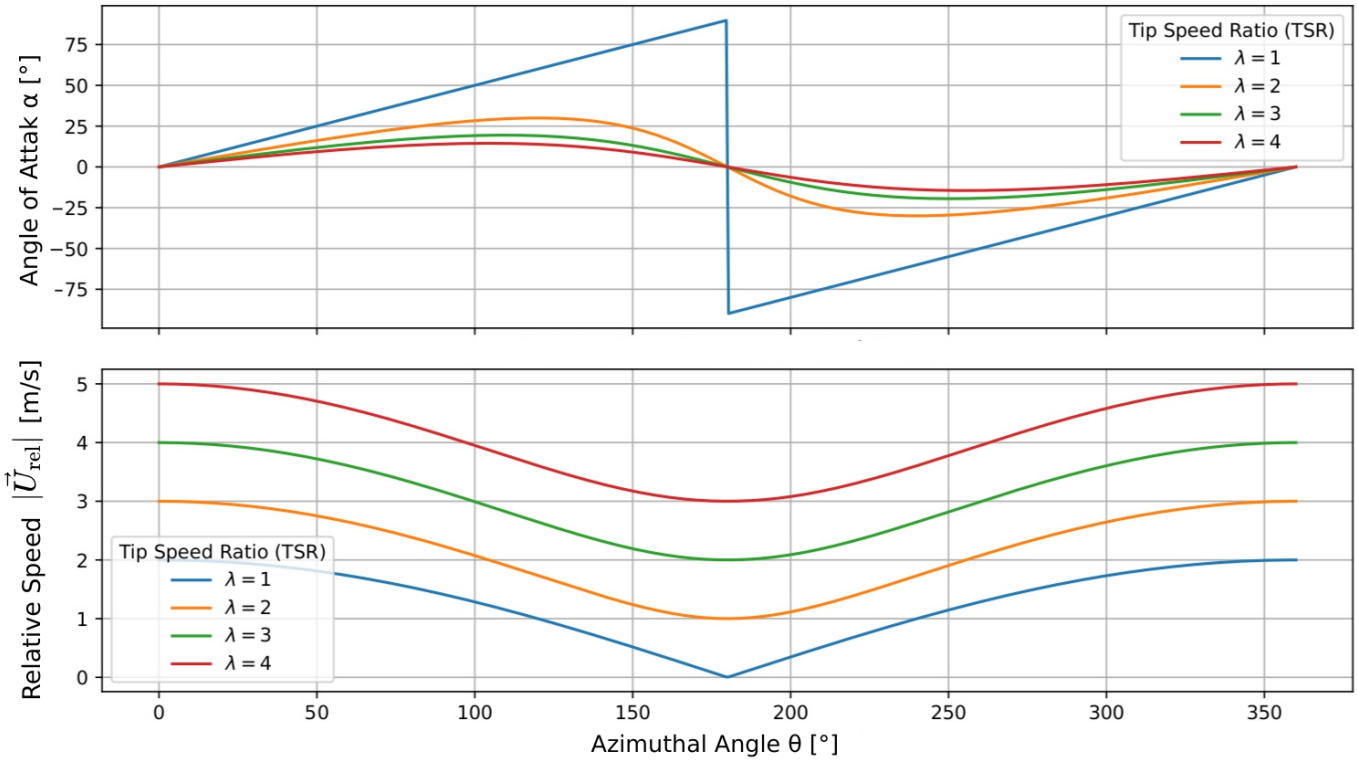

Figure 2.6: Top: Angle of Attack (α) and Bottom: Magnitude of the Blade-Relative Velocity ($|\vec{U}_{rel}|$) versus Azimuthal Angle (θ) for different tip speed ratios (λ). The freestream wind velocity is $U_\infty = 1$ m/s. The NACA 0015 airfoil typically achieves maximum lift-to-drag ratio at an AoA of about 6°–10° based on XFoil polar data from AirfoilTools [25], making these angles at the highest relative velocity most desirable for performance.

Then, using the calculated angle of attack (α) and relative velocity (U_{rel}), the blade element experiences lift (F_L) and drag (F_D) forces. As shown in Figure 2.7 (left), these forces are determined by the relative velocity, angle of attack, air density (ρ), blade area (A), and the airfoil's lift and drag coefficients ($C_L(\alpha)$) and ($C_D(\alpha)$). These lift and drag forces are then resolved into tangential (F_T) and normal (F_N) components relative to the blade's circular path, as illustrated in Figure 2.7 (right). The tangential force (F_T) generates rotor torque, while (F_N) contributes to blade bending moments.

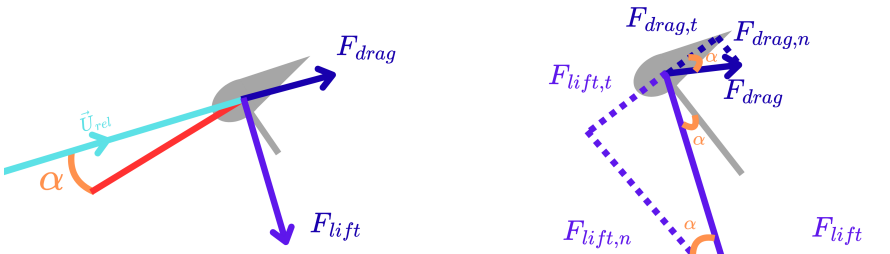

$$F_{drag} = \frac{1}{2}\rho A_{blade} C_D(\alpha) |\vec{U}_{rel}|^2 \quad (7)$$

$$F_{lift} = \frac{1}{2}\rho A_{blade} C_L(\alpha) |\vec{U}_{rel}|^2 \quad (8)$$

$$F_{lift,t} = F_{lift} \cdot sin(\alpha) \quad (9)$$

$$F_{drag,t} = F_{lift} \cdot cos(\alpha) \quad (10)$$

Figure 2.7: Aerodynamic force decomposition on a VAWT blade element. Left: Calculation of lift and drag from relative velocity and angle of attack. Right: Resolution of lift and drag into tangential and normal forces.

Then, as depicted on the left side of Figure 2.8, these forces are vectorially summed to obtain the net force in the tangential direction. This net tangential force, shown on the right side of the figure, is subsequently multiplied by the radius of the VAWT arm to determine the torque experienced by the wind turbine. The power generated is then calculated by multiplying this torque by the angular velocity. This calculated power is utilized to estimate the power coefficient (see Equation 2).

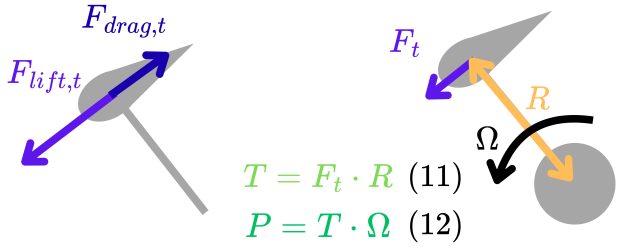

$$T = F_t \cdot R \quad (11)$$

$$P = T \cdot \Omega \quad (12)$$

Figure 2.8: Illustration of force composition, torque generation, and power estimation in a VAWT. (Left) Summation of forces to obtain net tangential force. (Right) Calculation of torque by multiplying tangential force by the VAWT arm radius.

The instantaneous torque produced by a VAWT blade varies significantly with its azimuthal position due to cyclic changes in relative velocity and angle of attack throughout a revolution. For a two-bladed rotor, this results in a characteristic torque profile with two distinct peaks and two troughs per rotation, as shown in Figure 2.9 and predicted by aerodynamic models.

In general, an N-bladed rotor produces $2N$ torque oscillations per revolution, since each blade contributes two fluctuations per cycle. For higher blade counts, these oscillations overlap, yielding a smoother overall torque profile. As an example, the two-bladed rotor shown in Figure 2.9 exhibits two peaks and two troughs per revolution. At azimuthal positions near $\theta = 0°$ and $180°$, the relative velocity is oriented such that the effective angle of attack is unfavorable (nearly perpendicular to the blade chord) resulting in high drag, low lift, and torque dips. At intermediate angles, more favorable aerodynamic conditions generate higher lift and torque peaks.

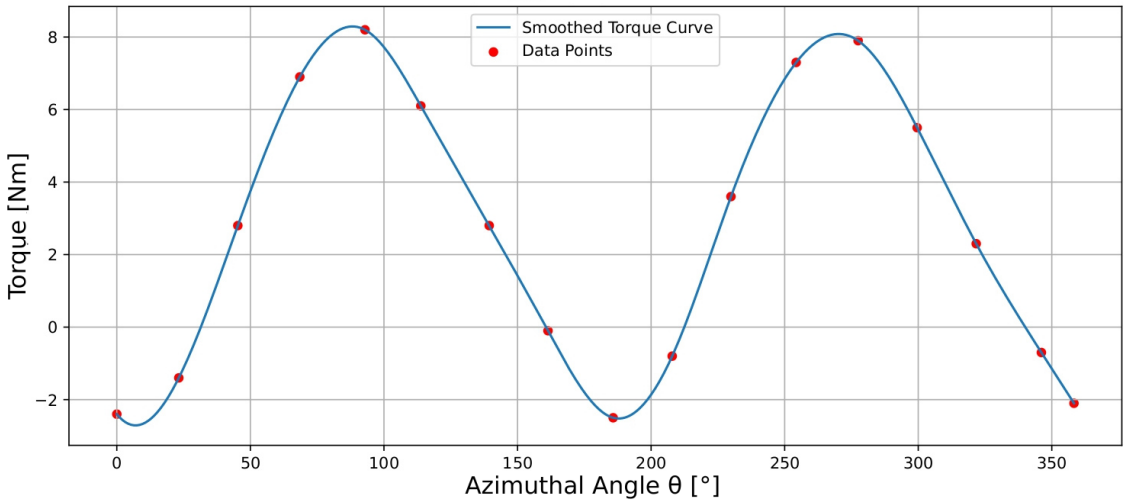

Figure 2.9: Torque distribution over the azimuthal angle for a two-bladed H-Darrieus turbine at solidity $\sigma = 0.3$ and tip speed ratio $\lambda = 3.6$, based on 3D unsteady numerical simulations. Solidity quantifies the blade area relative to the swept area. Aerodynamic interactions and flow unsteadiness cause asymmetric torque over a full rotation [26].

These torque fluctuations affect overall turbine performance, typically summarized by the power coefficient (C_p) versus tip speed ratio (λ), as previously noted for HAWTs. Figure 2.10 shows a typical C_p-λ curve for a Darrieus rotor with four key operational regions. The variation in blade angle of attack with λ, illustrated in Figure 2.6, is crucial to understanding these regions:

- **Deep Stall:** At low λ, blades experience very high angles of attack, causing flow separation and stall, which leads to low power output.
- **Dynamic Stall:** At moderate λ, rapid changes in angle of attack cause unsteady aerodynamic effects, temporarily increasing lift but also causing oscillations and losses.

- **Ideal Operation:** At optimal λ, blades maintain steady, moderate angles of attack with mostly attached flow, maximizing lift and minimizing drag to achieve peak C_p.
- **Drag Region:** At high λ, angles of attack are small, reducing lift; drag forces dominate and C_p decreases.

These regions capture how blade aerodynamics vary during rotation, influencing turbine performance and mechanical loads.

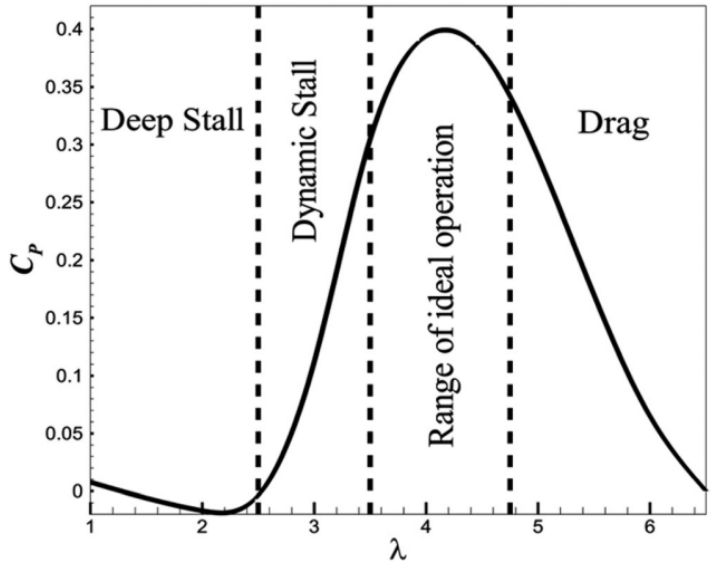

Figure 2.10: Example typical Darrieus rotor performance: power coefficient C_p versus tip speed ratio (λ), indicating Deep Stall, Dynamic Stall, Ideal Operation, and Drag regions [27].

Thus, aerodynamic variations in angular velocity and relative wind speed can reduce VAWT efficiency under steady conditions. However, the strong dependence of relative velocity and angle of attack on the free-stream wind speed U_∞ makes VAWTs ideal for studying performance during wind surges. The cyclical power extraction presents both challenges and opportunities; understanding the interaction between relative wind speed and angle of attack is essential to maximize benefits while minimizing drawbacks and improving overall performance.

2.4 Research Context and Historical Literature Overview

The previous section examined VAWT blade aerodynamics under steady inflow, where angle-of-attack variation stems purely from rotation. However, in offshore applications, particularly floating VAWTs, unsteady inflow due to wave motion and turbulence introduces additional aerodynamic complexity. Understanding these effects forms the basis of this research and is explored further through relevant theoretical and historical work.

2.4.1 Early Developments (1973–2008)

In 1973 Gormont's seminal work [28] introduced a mathematical framework to model dynamic stall, where delayed flow separation at high angles of attack causes transient lift peaks followed by rapid stall. He showed that neglecting dynamic stall results in inaccurate predictions of rotor loads and performance under unsteady conditions, proving it must be included in accurate aerodynamic models. Though developed for helicopter rotors, these principles apply to VAWTs, which also experience strongly varying angles of attack. Fluctuating wind conditions intensify these effects, highlighting the critical impact of dynamic stall on VAWT performance and the need for further research on how such unsteady winds affect turbine aerodynamics and power output.

Building on the foundational work of Gormont (1973), McIntosh et al. [29] numerically investigated VAWT performance under unsteady freestream conditions using a two-dimensional, Lagrangian-based free vortex model. While previously validated for steady inflow, it was applied to synthetic sinusoidal fluctuations and a 300-second sample of measured wind data. Comparing the unsteady vortex model with a quasi-steady model (where power depends only on tip speed ratio) revealed that unsteady inflow can enhance energy extraction beyond steady predictions, primarily due to turbine–wake interactions. However, this analysis was limited to a two-dimensional numerical model without experimental validation, motivating the present study to experimentally investigate VAWT aerodynamics in sinusoidal wind conditions.

Their results show a net increase in the energy extraction coefficient (C_e), defined as the ratio of extracted energy to available wind energy over the period T,

$$C_e = \frac{E_{\text{turb}}}{E_{\text{wind}}} = \frac{\int_0^T C_p(\lambda) U^3 \, dt}{\int_0^T U(t)^3 \, dt}, \tag{13}$$

under conditions of sinusoidally varying freestream velocities, where U is the fluctuating wind speed. At low perturbation frequencies ($k_{turb} = 0.01$), the unsteady vortex

model closely matches steady-state C_e predictions. However, at higher frequencies ($k_{turb} = 0.1$), the unsteady model produces pronounced hysteresis loops in C_e, with time-averaged values exceeding those from steady inflow conditions. Although the article does not explicitly define k, it is likely given by

$$k_{turb} \approx \frac{\Omega \times l_{chord}}{U_{\text{mean}}}, \tag{14}$$

where Ω is angular velocity and U_{mean} is the mean inflow velocity.

While dynamic stall is often considered detrimental due to associated aerodynamic losses and structural fatigue, these findings suggest it can improve performance under certain unsteady inflow conditions. This effect is illustrated in Figure 2.11, where the dynamic stall model is inactive on the left, meaning important effects like dynamic stall vortices are not accounted for, and active on the right, capturing these transient aerodynamic phenomena and their positive impact on energy extraction. Dynamic stall vortices are rotating pockets of airflow that form on the blade during rapid changes in angle of attack, temporarily increasing lift before shedding away.

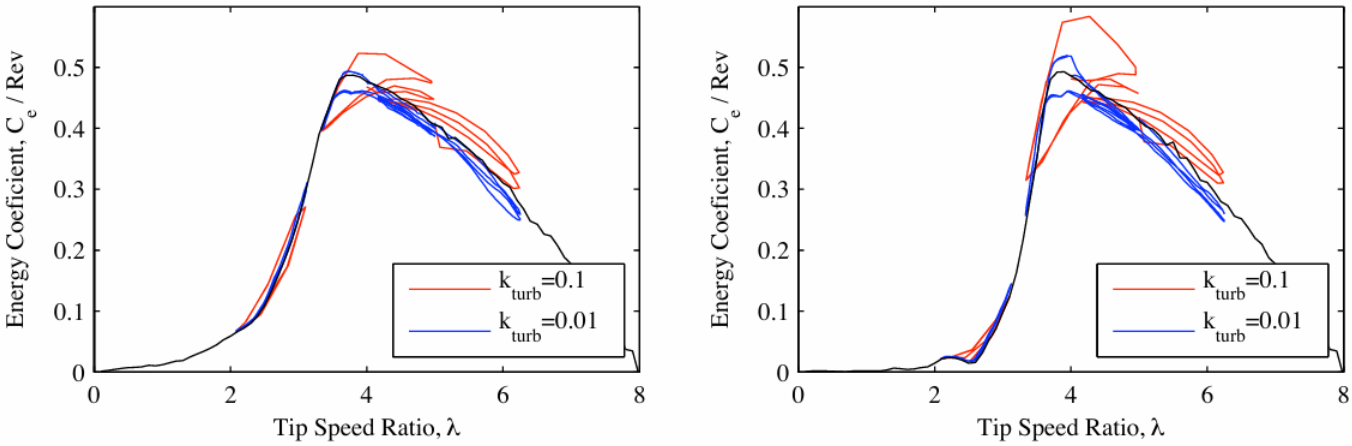

(a) With dynamic stall (b) Without dynamic stall

Figure 2.11: Hysteresis loops of the energy extraction coefficient (C_e) under 20% sinusoidal freestream velocity fluctuations for turbines at different tip speed ratios (λ_∞ = 2.5, 4, and 5.5; defined as $\lambda_\infty = \Omega R/U_\infty$) with constant angular velocity control. The black line represents the stationary (steady inflow) case, the blue line corresponds to $k_{turb} = \Omega l_{chord}/U_{mean} = 0.01$, and the red line to $k_{turb} = 0.1$, the dimensionless turbine reduced frequency (Equation 14). Left: dynamic stall model inactive (no dynamic stall vortices). Right: dynamic stall model active, capturing transient aerodynamic effects that enhance energy extraction. Adapted from McIntosh et al. [29].

2.4.2 Intermediate Developments (2010–2013)

Following the early work, Danao and Howell (2012) [30] numerically studied VAWTs under unsteady wind inflow and found significant performance degradation when wind fluctuation frequencies approached the turbine's rotational frequency. This resonant interaction led to a notable drop in power coefficient (C_p), emphasizing the importance of aligning turbine parameters, such as rotational speed and tip speed ratio (λ), to avoid such conditions. These results highlight the need for adaptive control strategies that mitigate resonant effects and maintain performance under fluctuating winds.

Building on this understanding of unsteady wind effects, Danao et al. (2013) [31] conducted a comprehensive Computational Fluid Dynamics (CFD) analysis of VAWT aerodynamics under fluctuating wind conditions.

In Figure 2.12, they investigated a characteristic freestream fluctuation frequency of $f_c = 0.5$ Hz with velocity amplitude $U_{\text{amp}} = \pm 12\%$. Different tip speed ratios (λ), varied via turbine speed, showed higher or lower cycle-averaged power coefficients (C_p) compared to the steady case. As f_c is dimensional (Hz), the results depend on the relative interaction between turbine rotation and wind fluctuations, so they should be interpreted with caution.

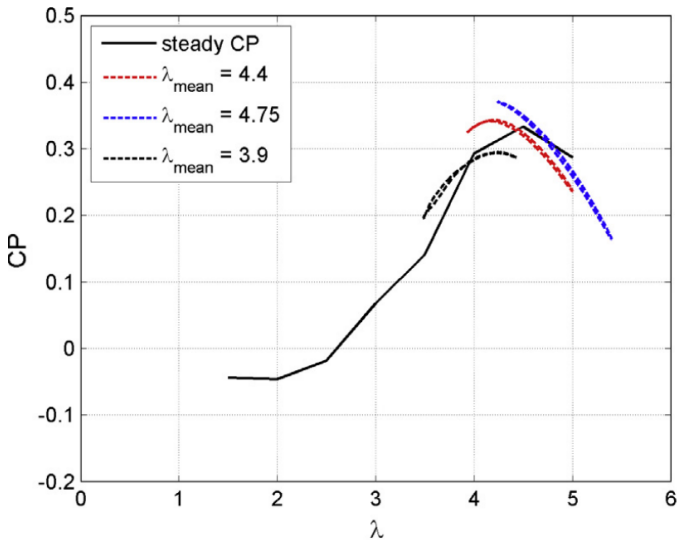

Figure 2.12: Cycle-averaged power coefficient (C_p) versus tip speed ratio (λ) for fluctuating wind at $f_c = 0.5$ Hz and $U_{amp} = \pm 12\%$. Results show a clear dependence of C_p on λ under unsteady wind [31].

In Figure 2.13, three amplitudes were tested: $U_{\text{amp}} = \pm 7\%$ (± 0.49 m/s), $U_{\text{amp}} = \pm 12\%$ (± 0.84 m/s), and $U_{\text{amp}} = \pm 30\%$ (± 2.1 m/s). While the general C_p-λ trend remains consistent across amplitudes, the overall cycle-averaged C_p decreases with increasing amplitude, yielding values of approximately 0.35, 0.33, and 0.25, respectively. This suggests a degradation in performance as the amplitude of wind fluctuation increases.

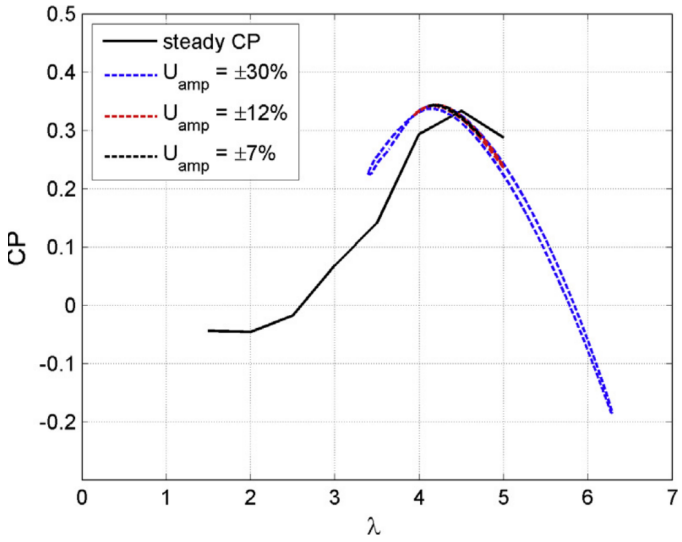

Figure 2.13: Effect of different wind fluctuation amplitudes ($\pm 7\%$, $\pm 12\%$, $\pm 30\%$) on cycle-averaged C_p. The shape of the C_p curve remains consistent, but average performance decreases with increasing amplitude [31].

Figure 2.14 presents vorticity-based flow visualizations for selected rotor cycles during the first quarter of the wind fluctuation period at $\theta = 130°$ and an average velocity of 7.9 m/s. The case with the largest amplitude ($U_{\text{amp}} = \pm 30\%$) shows significantly different stalling behavior, transitioning from shallow stall to deeper and more prolonged separation. This likely explains the pronounced drop in C_p.

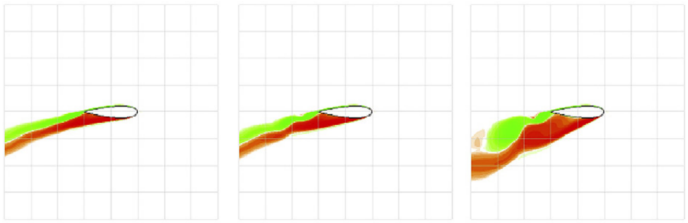

Figure 2.14: Vorticity contour snapshots at $\theta = 130°$ for different wind fluctuation amplitudes ($\pm 7\%$, $\pm 12\%$, $\pm 30\%$) values, showing stall development. High-amplitude cases ($\pm 30\%$) show stronger separation, leading to average performance loss [31].

Finally, Figure 2.15 investigates the effects of fluctuation frequency by comparing $f_c = 0.5$ Hz, 1 Hz, and 2 Hz, at a fixed amplitude of $U_{\text{amp}} = \pm 12\%$. The results suggest that within the tested parameter range, the differences in performance due to fluctuation frequency are negligible.

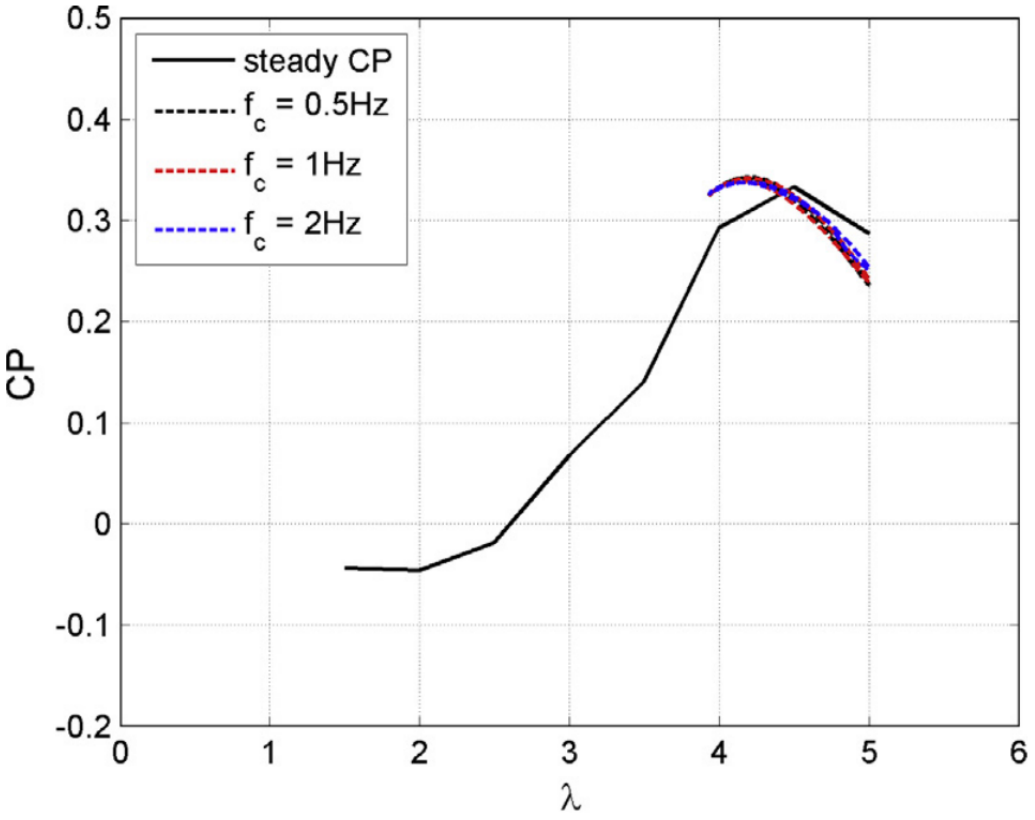

Figure 2.15: Cycle-averaged C_p at different fluctuation frequencies ($f_c = 0.5$, 1, 2 Hz) for $U_{amp} = \pm 12\%$. Results show minimal variation, indicating weak dependence on f_c in this range [31].

Complementing these findings, Howell [32] highlights the influence of roughness and dynamic stall on the aerodynamic performance of three-bladed VAWTs in an experimental study. Figure 2.16 illustrates how surface roughness can trip the boundary layer to turbulence, altering the local flow around the blades and thereby affecting torque characteristics. These effects exhibit a nonlinear relationship with flow velocity, emphasizing the importance of characterizing the flow state to ensure accurate comparisons between experimental cases.

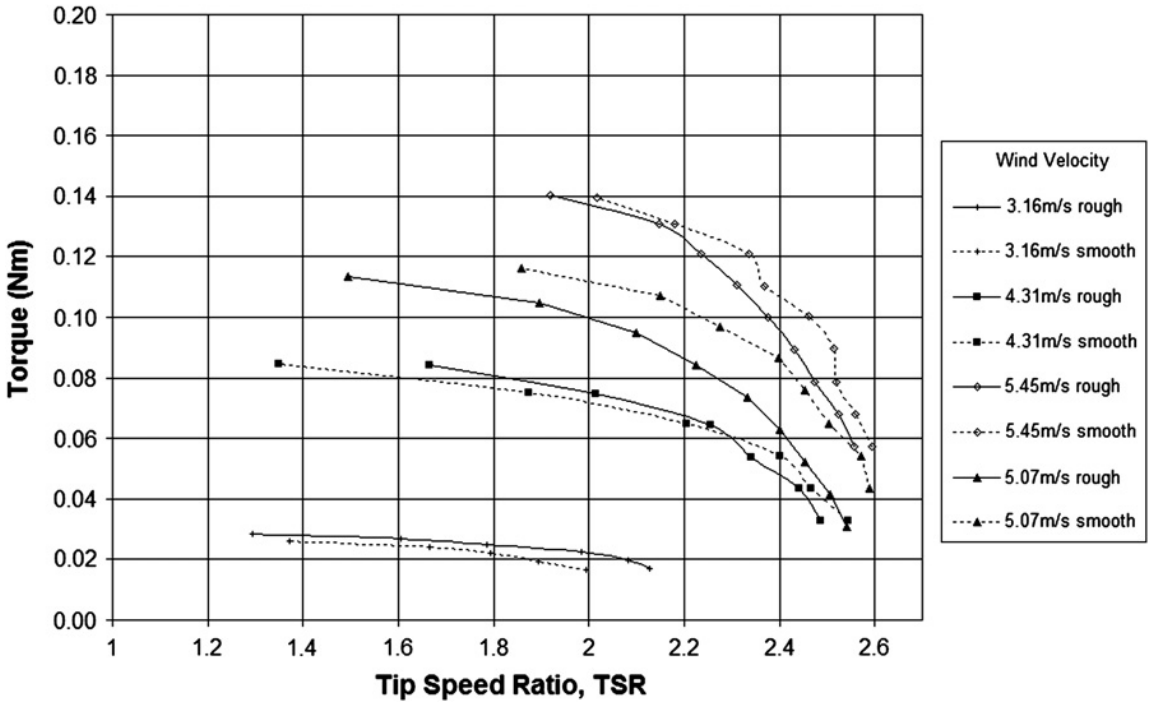

Figure 2.16: Influence of surface roughness on the torque of VAWT rotor blades, based on Howell [32]. At lower flow velocities, increased surface roughness promotes earlier transition to a turbulent boundary layer, improving flow attachment and increasing torque generation. However, at higher velocities, the same roughness can induce premature flow separation or stall, resulting in a reduction in torque. This highlights the significant and nonlinear influence of surface roughness on the aerodynamic performance of VAWTs.

2.4.3 Recent Advances (2014–2024)

Recent research has focused on improving the aerodynamic efficiency of VAWTs by adapting their design to unsteady wind conditions. Wekesa et al. [33] investigated the performance of VAWTs equipped with NACA 0022 and NACA 0015 symmetric airfoils under fluctuating wind conditions (see Figure 2.17). They concluded that thicker airfoils offer better resistance to stall. Their findings showed that the maximum unsteady C_p of VAWTs with thicker blades can exceed the steady-state C_p at λ slightly below the steady-state optimum. In contrast, thinner blades experience a slight reduction in C_p within the same λ range.

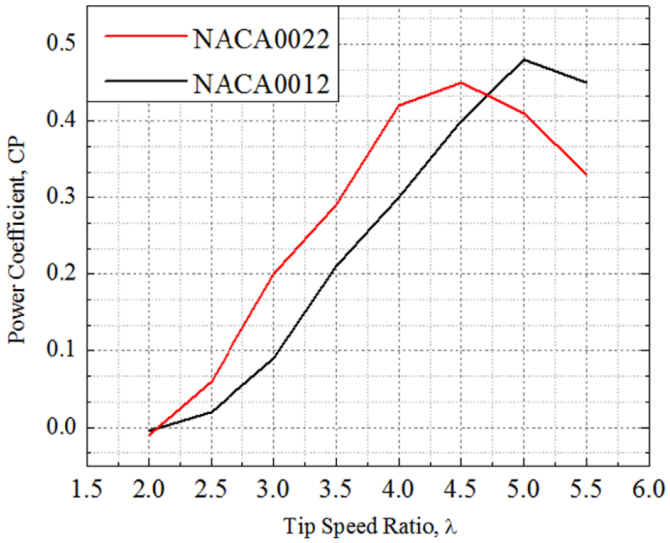

Figure 2.17: Comparison of power coefficient (C_p) versus tip speed ratio (λ) for NACA 0022 and NACA 0015 airfoils under unsteady wind conditions (constant freestream velocity $U_\infty = 11.0$ m/s), based on Wekesa et al. [33]. Thicker airfoils (NACA 0022) show improved performance at lower λ values compared to thinner airfoils.

In 2022, Chen et al. [34] applied modern optimization techniques to VAWTs by combining the Taguchi method with a neural network model. The Taguchi method is a robust and time-efficient design of experiments approach used to systematically investigate the influence of multiple parameters on a performance metric, such as the C_p. Rather than relying directly on C_p values, the method uses the signal-to-noise (S/N) ratio as a more stable performance indicator. This allows researchers to assess the consistency and reliability of parameter impacts even under fluctuating conditions.

For cases where maximizing performance is desired, the S/N ratio is calculated using the "larger-the-better" formulation:

$$\frac{S}{N} = -10 \log_{10} \left(\frac{1}{n} \sum_{i=1}^{n} \left(\frac{1}{y_i^2} \right) \right), \tag{15}$$

where y_i is the objective function (in this case, C_p) from each simulation, and n is the number of repetitions per case. In practice, this ratio enables one to distinguish parameters that consistently lead to better outcomes, even when performance varies due to external fluctuations. The impact of each parameter is then evaluated by the difference between the maximum and minimum average S/N ratios across its levels.

The parameters, mean inlet velocity, mean tip speed ratio, fluctuation amplitude, and frequency, each have three discrete levels (Figure 2.18a). These are combined into nine cases using an L9 orthogonal array (Figure 2.18b), efficiently covering the parameter space with minimal simulations.

Table 1
The operation parameters and levels of unsteady wind conditions.

Parameters	Factor	Symbols	Levels		
			1	2	3
Mean velocity inlet ($m \cdot s^{-1}$)	A	V_{mean}	3	10	17
Mean tip speed ratio	B	TSR_{mean}	2	4	6
Fluctuation amplitudes ($m \cdot s^{-1}$)	C	V_{amp}	0	1.5	3
Fluctuation frequencies (Hz)	D	f_c	0.5	1	2

Table 3
The layout of Taguchi's L_9 orthogonal array design.

Case	V_{mean}	TSR_{mean}	V_{amp}	f_c
S1	1	1	1	1
S2	1	2	2	2
S3	1	3	3	3
S4	2	1	2	3
S5	2	2	3	1
S6	2	3	1	2
S7	3	1	3	2
S8	3	2	1	3
S9	3	3	2	1

(a) Mean S/N ratio of factors A–D. *(b) Relative effect of each factor.*

Figure 2.18: Results from Chen et al. [34]: (a) average S/N ratio profiles, and (b) quantified influence of each factor by looking at the difference.

Chen et al. [34] quantified the influence of variables on VAWT power coefficient C_p under unsteady conditions. As shown in Figure 2.19, Factor B (λ_{mean}) has the greatest impact, followed by C (fluctuation amplitude), A (mean inlet velocity), and D (fluctuation frequency).

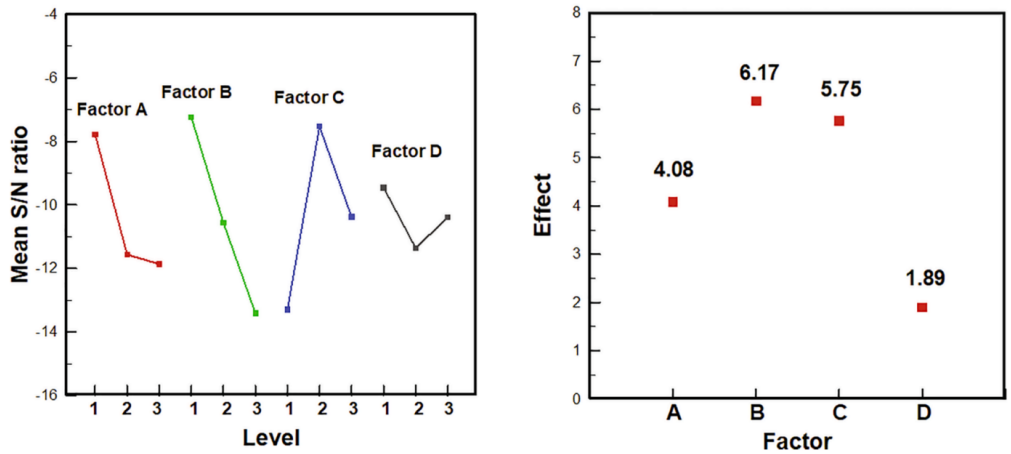

Figure 2.19: Results from Chen et al. [34] showing the (left) average S/N ratios of factors A–D, and (right) the difference between the minimum and maximum mean S/N ratios per factor, indicating the relative importance of each variable in the Taguchi method analysis.

Complementing this line of research, Wei et al. (2023) [35] investigated HAWTs and demonstrated that unsteady inflow conditions can substantially enhance the time-averaged power output. Building upon these findings, the present project aims to evaluate the applicability of these effects to VAWTs.

Earlier experimental work by Wei and Dabiri (2022) [8] developed models for unsteady power generation in HAWTs, highlighting the role of generator torque dynamics in predicting turbine performance. While this research focuses on HAWTs, the insights on generator torque under unsteady inflow are transferable to VAWTs. As such, these results provide a useful comparative framework for interpreting the VAWT's performance under sinusoidal inflow in the current study. Figure 2.20 illustrates the variation in generator torque with sinusoidal surge-velocity waveforms, providing a valuable benchmark for comparison.

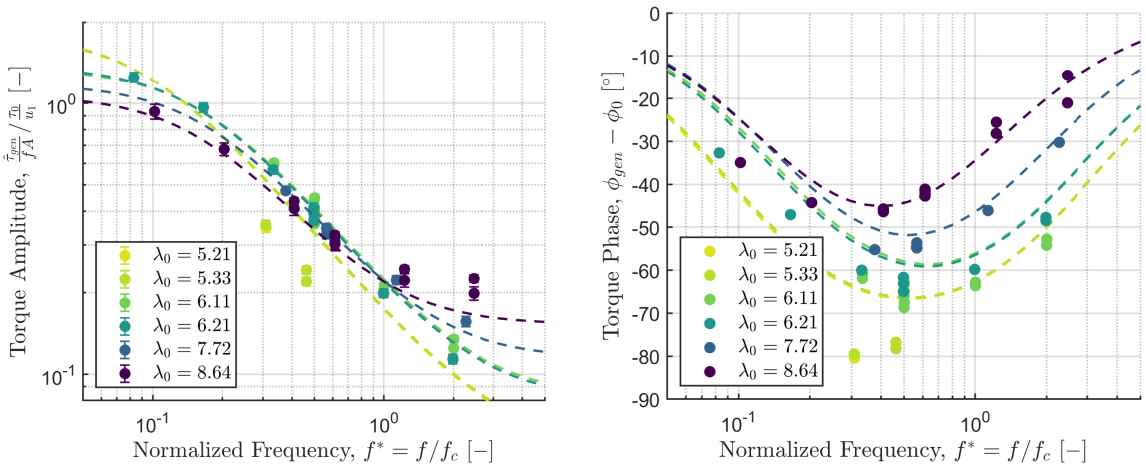

(a) (b)

Figure 2.20: Generator torque amplitude and phase response of a HAWT subjected to sinusoidal surge-velocity waveforms. The results demonstrate the predictive accuracy of a first-order linear ordinary differential equation model in capturing unsteady inflow dynamics [8].

In 2024, research has increasingly focused on optimizing wind turbine performance through the integration of unsteady flow dynamics. Through experiments, Wei et al. [36] demonstrated that periodic turbine motions can significantly enhance wake recovery and power density. This raises the question of whether similar performance improvements can also be achieved experimentally for VAWTs operating under unsteady inflow conditions.

2.5 Key Insights and Research Gap

To summarize, in 1973, Gormont [28] pointed out that rapid changes in the angle of attack can cause dynamic stall, which has a big impact on turbine blade performance. This sparked interest in how fluctuating wind speeds, causing similar angle changes, might affect vertical-axis wind turbines (VAWTs). Building on this, McIntosh et al. [29] used a two-dimensional free vortex model to show that under certain conditions, these fluctuations can boost the power coefficient (C_p) of VAWTs.

Since then, research has examined how VAWTs handle fluctuating winds. Danao and Howell [30] highlighted the need for adaptive control to avoid damaging resonance effects. Later, they [31] used CFD simulations to study how wind fluctuations affect tip speed ratio (λ) and power output. With fixed rotor speed, instantaneous λ varied with the wind, but the average λ was set by the rotor speed relative to the mean wind. Their results showed that the same fluctuating wind can increase or decrease power output depending on λ, with larger fluctuation amplitudes reducing efficiency, while fluctuation frequency had little effect in the tested range.

Other studies continued to refine the picture. Wekesa et al. [33] found that blade thickness also influences performance, specifically under fluctuating flows. More recently, Chen et al. [34] combined CFD with a Taguchi experimental design to rank the factors affecting performance. They discovered that the average tip speed ratio (λ) is the most important, followed by fluctuation amplitude, mean wind speed, and then fluctuation frequency.

While much of this work relies on simulations, experimental studies have started to catch up. For instance, Wei et al. [8], [35], and [36] showed that periodic wind speeds can improve the performance of horizontal-axis wind turbines (HAWTs). But for VAWTs, there's still a clear gap—experimental evidence is scarce.

This thesis aims to fill that gap by experimentally investigating how sinusoidal wind velocity fluctuations affect key VAWT performance metrics like power coefficient, torque, and wake behavior. Following Howell [32], special care is taken to account for turbulence intensity (TI) in the experimental design. Additionally, this work explores how to optimize the tip speed ratio (λ) in these dynamic wind conditions to maximize energy output. Ultimately, the goal is to help improve both the modeling and design of VAWTs that can thrive in fluctuating wind environments. This leads to the following research question:

> *How do periodic wind velocities impact the energy output of vertical-axis wind turbines, and how can this be optimized using the tip speed ratio (λ)?*

2.6 Research Objectives

To answer the central research question, this thesis sets out three main objectives, making use of the experimental capabilities and expertise available at Delft University of Technology:

1. **Understand the wind conditions created in the Windshape facility at DCSC.**
   Before testing any turbines, it's essential to know exactly what kind of wind we're working with. This objective focuses on mapping the flow field in the Windshape test facility—looking at how wind speed varies across space, how much turbulence is present, and how well the system can generate clean sinusoidal wind patterns. So far, no full characterization of this setup exists, which makes it difficult to confidently interpret turbine results. This step builds that foundation.

2. **Design and build a H-Darrieus VAWT for testing.**
   As part of this research, a custom vertical-axis wind turbine (VAWT) will be designed from scratch, guided by aerodynamic theory and established design practices. The goal is to create a turbine that is structurally sound and suitable for wind tunnel testing, with a setup that allows for precise measurement of its response to periodic wind input.

3. **Test how the turbine performs in steady vs. sinusoidal wind.**
   With the turbine built and the wind field mapped, the final goal is to test how it performs under different wind scenarios. Key performance indicators like power coefficient, torque, and angular velocity will be measured under both steady and sinusoidally varying wind. By comparing these cases, we can see how things like fluctuation frequency and amplitude affect performance—and figure out how to fine-tune the tip speed ratio (λ) for best results in unsteady conditions.

3. Theory for Thesis Goals

Following the research objectives, this section reviews background supporting the study's three main goals: characterizing flow in the WindShape facility, designing a vertical-axis wind turbine (VAWT), and evaluating turbine performance under variable wind. It brings together key insights to guide the experimental approach.

3.1 Characterizing Flow Conditions in the Wind Facility

Reliable experimental outcomes require accurate characterization of the flow conditions within the Wind AI facility. This subsection outlines the facility's design and capabilities to contextualize the measurement environment.

3.1.1 Wind AI facility

A key part of this characterization is understanding the experimental setup. The Wind AI facility at TU Delft (see Figure 3.1) is a platform for testing control systems in low-speed, complex flow environments.

Figure 3.1: Overview of the DCSC Wind AI facility. The WindShaper fan wall (highlighted in orange) generates custom wind profiles within the modular wind tunnel sections (green), which can be extended or reconfigured as needed. The test section is located behind the black windows, while the operator workstation is circled in red on the right. Blue arrows show the airflow path: wind is blown through the tunnel and recirculated back along the top and sides of the facility.

At the heart of the Wind AI facility is the WindShaper fan wall, a modular array of 729 individually controllable fans manufactured by WindShape [37] (see Figure 3.2). These fans can generate custom wind profiles—such as gusts, shear, and turbulence—within a confined test section known as the "box," enabling experiments under dynamic, non-uniform inflow conditions.

This flexibility makes Wind AI particularly suited for sensor-rich, small-scale experiments focused on real-time control, feedback, and flow sensing. However, the facility trades this adaptability for some limitations compared to traditional aerodynamic setups like TU Delft's Open Jet Facility (OJF) . These include lower maximum wind speeds, reduced inflow uniformity, and limited control over boundary conditions.

Unlike conventional tunnels designed to produce steady, high-speed flow, Wind AI replicates the kinds of unsteady, complex wind environments often encountered in real-world scenarios. As such, precise flow characterization is critical. The absence of standard flow-conditioning components, such as honeycombs and settling chambers, likely results in higher turbulence intensities than the typical 0.5–1.0% range [38], underlining the need for detailed spatial and temporal assessment (Project Goal 1).

Figure 3.2: The WindShaper uses a modular fan array to generate complex inflow patterns by selectively activating fans. Accurate spatial and temporal flow assessment is essential for validating experimental conditions [37].

Several experimental campaigns have already been conducted in the Wind AI facility under low-speed flow conditions, including:

- Synchronized Dynamic Induction Control: An Experimental Investigation [39],
- Mimicking the Helix with a porous disc for wind tunnel testing [40].

3.1.2 Measurement Techniques

To characterize the complex flow conditions within the WindShaper test facility, a variety of measurement techniques are available, each with distinct advantages and limitations. Table 3.1 provides a concise comparison of the most relevant methods, highlighting their suitability for this research.

Traditional methods like pitot-static tubes are simple and reliable for measuring mean flow speeds but cannot capture directional components. Advanced optical techniques such as Laser Doppler Anemometry (LDA) and Particle Image Velocimetry (PIV) offer high spatial and temporal resolution. In the WindShaper, optical access for PIV is actually more straightforward than in the Open Jet Facility (OJF); however, the high cost of tomographic PIV hardware, the complexity of post-processing, and the additional expense of installing required safety measures remain significant barriers. Hot-wire anemometry effectively measures fine-scale turbulence but is fragile and sensitive to environmental conditions, making it less suitable for routine use. Multi-hole pressure probes can measure both velocity magnitude and flow direction but require careful calibration and intrude on the flow.

Considering these factors, the TriSonica ultrasonic anemometer emerges as the optimal choice for this study. As detailed in Table 3.1, it offers a robust, compact design with no moving parts, enabling real-time measurement of three-dimensional wind vectors. Its ease of integration within the WindShaper—due to mounting points and straightforward data acquisition—further supports its suitability. Additionally, the availability of the TriSonica and the existing familiarity of DCSC staff with this instrument facilitate smoother project execution and reduce the learning curve.

The TriSonica Sphere sensor features three ultrasonic transducers arranged in a tetrahedral configuration (see Figure 3.3). Each transducer alternates between transmitting and receiving ultrasonic pulses. By measuring the time-of-flight of sound waves along multiple paths, the sensor detects wind-induced variations in propagation speed. These bidirectional time differences are used to reconstruct the three-dimensional wind velocity vector, capturing both wind speed and direction.

Table 3.1: Comparison of flow measurement techniques relevant to WindShaper testing.

Technique	Advantages	Limitations	Suitability	Citations
Pitot-static tube	Simple, low-cost, reliable for mean flow measurements	Cannot resolve turbulence or directional components	Low	[41]
Laser Doppler Anemometry (LDA)	Non-intrusive; high-frequency velocity measurements	Requires seeding particles and optical access	Low	[42]
Particle Image Velocimetry (PIV)	Provides full velocity field; excellent for visualization and validation	Complex setup and post-processing; requires seeding, and costs	Low	[43]
Hot-wire anemometry	High-frequency; ideal for turbulence studies	Fragile, intrusive; sensitive to temperature drift	Moderate	[44]
Multi-hole pressure probe	Measures velocity magnitude and flow direction (yaw/pitch)	Requires complex calibration; intrusive to flow	Moderate	[45, 46]
TriSonica ultrasonic anemometer	Compact; no moving parts; real-time 3D wind vector	Limited temporal resolution and spatial precision	**High**	[47]

Figure 3.3: TriSonica ultrasonic anemometer with four transducers in a tetrahedral arrangement. It measures three-dimensional wind speed and direction by analyzing the time-of-flight of ultrasonic pulses along multiple axes [47].

Despite its advantages, the TriSonica has limitations, including moderate temporal resolution and spatial precision compared to more specialized optical systems. However, its non-intrusive nature and capability for dynamic flow assessment make it uniquely suited to the WindShaper's goal of generating and measuring complex, time-varying inflow patterns.

3.2 Designing and Constructing a VAWT

After characterizing the wind tunnel, designing and constructing a single-bladed H-Darrieus VAWT requires an iterative process of development and evaluation. This section reviews the relevant background and design choices made.

3.2.1 Fundamental Physical Variables

To analyze and optimize the performance of a VAWT, it is essential to understand the physical quantities that form the basis of its dimensionless parameters. Figure 3.4 provides a schematic overview of the key variables used throughout this analysis:

Fluid Properties

- ρ: Air density.
- ν: Kinematic viscosity of air.

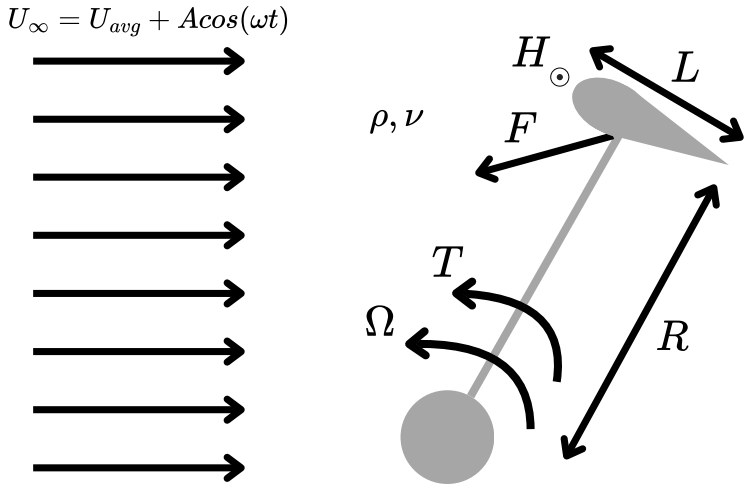

Figure 3.4: Schematic representation of the fundamental physical quantities used in defining dimensionless parameters relevant to VAWT aerodynamics and performance analysis.

Wind Characteristics

- U_∞: Freestream wind velocity approaching the turbine .
- U_{avg}: Average wind velocity over time.
- A: Amplitude of the wind oscillations.
- $\cos(\omega t)$: Periodic variation in wind speed, with ω as the angular frequency.

Turbine Geometry

- N: Number of blades.
- L: Chord length of the airfoil.
- R: Rotor radius ($D = 2R$).
- H: Height of the blades.
- A_{area}: Blade area, defined as $A_{area} = D \cdot H$ (16).

Kinematics and Output

- Ω: Angular velocity of the rotor.
- F: Aerodynamic force acting on the blade.
- T: Torque on the rotor, given by $T = F \cdot R$ (Equation 11).
- P: Mechanical power output, given by $P = T \cdot \Omega$ (Equation 12).

3.2.2 Key Dimensionless Parameters

Based on these variables, the following sections introduce the key dimensionless parameters that characterize VAWT performance. A summary of the parameters is provided in Table 3.2 at the end of this section.

Power Coefficient (C_p)

As explained earlier for HAWTs in Section 2.2, the Power Coefficient (C_p) quantifies the fraction of wind kinetic energy converted into mechanical power by a Darrieus H-type VAWT:

$$C_p = \frac{P}{0.5 \cdot \rho \cdot A_{area} \cdot U_\infty^3} = \frac{T \cdot \Omega}{0.5 \cdot \rho \cdot A_{area} \cdot U_{avg}^3} \tag{17}$$

Here, U_{avg} was used instead of the free-stream velocity U_∞, as the varying inflow would prevent defining a constant tip speed ratio. As shown in Figure 2.10, C_p is the key metric for evaluating turbine efficiency and comparing performance with literature and experiments.

Reynolds Number (Re)

The Reynolds number (Re) is a parameter affecting the aerodynamic performance of a Darrieus H-type VAWT. It characterizes the flow regime around the turbine blades- laminar, transitional, or turbulent—and influences the lift and drag forces acting on the blades. The Reynolds number is defined as the ratio of inertial to viscous forces in the flow and is given by:

$$Re_D = \frac{U_\infty D}{\nu} \quad or \quad Re_L = \frac{U_\infty L}{\nu} \tag{18}$$

Bachant and Wosnik [48] show that turbine performance becomes effectively Reynolds number-independent above critical thresholds such as $Re_D \sim 10^6$ (based on rotor diameter) or $Re_L \sim 2 \times 10^5$ (based on blade chord). Below these values, flow separation and wake dynamics vary significantly, impacting turbine efficiency.

Tip Speed Ratio (λ)

The Tip Speed Ratio (λ) is a key parameter for the aerodynamic performance of a Darrieus H-type VAWT. As introduced in Section 2.2 for HAWTs, it is defined as the ratio of the blade tip speed to the incoming wind velocity (Equation 3):

$$\lambda = \frac{U_{\text{tip}}}{U_\infty} = \frac{\Omega R}{U_{\text{avg}}} \tag{19}$$

Here, U_{avg} was used instead of the free-stream velocity U_∞, as the varying inflow would prevent defining a constant tip speed ratio. According to Ali et al. [15], λ governs the angle at which the wind meets the blades, influencing lift and drag. An optimal value ensures favorable angles of attack and maximizes power extraction. Too low a λ can cause stall, while too high increases drag and reduces efficiency.

Solidity Ratio

The Solidity Ratio (σ) is a dimensionless parameter for a Darrieus H-type VAWT. It represents the ratio of the total blade area to the turbine's swept area:

$$\sigma = \frac{NL}{2R} \tag{20}$$

Solidity influences the aerodynamic behavior of the turbine. According to Du et al. [49], a higher solidity increases the blade surface interacting with the wind, improving torque at low wind speeds but potentially causing excessive drag and flow blockage. Conversely, lower solidity reduces drag and allows higher rotational speeds but may not generate sufficient startup torque.

Dimensionless Frequency Ratio (ω^*)

The Dimensionless Frequency Ratio (ω^*) is a parameter for Darrieus H-type VAWTs operating under periodic freestream wind variations:

$$\omega^* = \frac{\omega}{\Omega} \tag{21}$$

According to Chen et al. [34], this factor has a relatively small influence on turbine performance based on CFD results. However, this study will also investigate ω^* experimentally, as it is possible that an optimal ω^* could enable the turbine blades to better synchronize with changing wind conditions, improving aerodynamic efficiency and reducing mechanical stress [8]. Deviations from this optimal ratio may lead to inefficient energy capture, increased wear, and operational instability.

Dimensionless Freestream Variation Amplitude (A^*)

The Dimensionless Freestream Variation Amplitude (A^*) quantifies the relative size of oscillations in the freestream wind velocity impacting a VAWT. The freestream velocity is described as:

$$U_\infty = U_{\text{avg}} + A\cos(\omega t), \tag{22}$$

The dimensionless amplitude is defined as the ratio of this amplitude to a characteristic length scale:

$$A^* = \frac{A}{R}, \tag{23}$$

According to Chen et al. [34], this parameter can affect turbine performance, likely due to its influence on unsteady aerodynamic forces and dynamic loading on the blades.

Table 3.2: Key dimensionless parameters for VAWT performance

Parameter	**Symbol & Formula**	**Description**
Power Coefficient	$C_p = \frac{P}{0.5\rho A_{area} U_{avg}^3}$	Efficiency of converting wind kinetic energy to mechanical power
Reynolds Number	$Re_D = \frac{U_\infty D}{\nu}, \quad Re_L = \frac{U_\infty L}{\nu}$	Characterizes flow regime: laminar to turbulent
Tip Speed Ratio	$\lambda = \frac{\Omega R}{U_{avg}}$	Ratio of blade tip speed to wind speed
Solidity Ratio	$\sigma = \frac{NL}{2R}$	Ratio of blade surface area to turbine swept area
Frequency Ratio	$\omega^* = \frac{\omega}{\Omega}$	Ratio of wind oscillation frequency to turbine rotation frequency
Freestream Amplitude	$A^* = \frac{A}{R}$	Relative amplitude of wind velocity oscillations

3.2.3 Choosing the Single-Blade Design

Having established the key dimensionless parameters governing turbine performance, the next step is to justify the choice of a single-blade configuration for the VAWT. This design isolates the aerodynamic behavior of an individual blade under sinusoidally varying wind, simplifying phase-dependent analysis.

Multi-blade turbines exhibit complex interactions, as each blade experiences the wind at a different azimuthal position and phase, complicating flow dynamics and performance prediction [50]. A single blade provides a clear phase relationship between wind frequency and rotor position, enabling more accurate predictions of aerodynamic forces and facilitating the optimization of operational conditions such as the tip speed ratio (λ) [50].

Although the single-blade design introduces challenges—such as the need for a counterweight to balance the rotor and reduce bearing loads, precise rotational control, and lower efficiency—it allows systematic study of blade aerodynamics at specific azimuthal positions and is therefore chosen for this study.

3.3 Turbine Performance under Various Conditions

With the wind tunnel active and the single-blade VAWT in place, experiments explored how periodic wind speed variations—characterized by the dimensionless frequency ratio (ω^*) and amplitude (A^*)—affect turbine performance across different tip-speed ratios (λ) and whether nonlinear or phase-dependent effects arise. Relevant literature is summarized in Table 3.3 for benchmarking.

Paper	**Reynolds Numbers**	**Solidity Ratio**	**Tip Speed Ratios**
[51]	70000	0.3	1–3
[52]	80000	0.17	0.1–6
	160000	0.17	0.1–6
	320000	0.17	0.1–6
[53]	16800–84000	0.13	1–5
	16800–84000	0.17	1–5

Table 3.3: Overview of dimensionless parameters (Reynolds number, solidity ratio, tip speed ratio) in key VAWT studies.

4. Wind AI Flow Characterization

With the relevant background now established, the first goal of this thesis is to attempt a basic characterization of the nominal test section volume within the WindAI facility operated by the at Delft Centre for Systems and Control (DCSC).

4.1 Objectives of the Experimental Campaign

The primary objective of this section is to outline how the WindAI facility will be used to generate the flow conditions necessary for aerodynamic testing of Vertical Axis Wind Turbines (VAWTs). Since WindAI differs from conventional wind tunnels, its volumetric flow characteristics within the test section have not yet been fully characterized. Therefore, it is necessary to first measure and analyze the mean flow velocity and turbulence intensity.

This characterization covers both steady and unsteady flow conditions, reflecting the realistic wind scenarios that a VAWT would encounter. By investigating different flow regimes, the capability of WindAI to reproduce relevant experimental conditions can be assessed. The study is divided into three main parts:

1. **Measurement Setup Verification**
   The impact of different TriSonica sensor mounting configurations is evaluated through repeated measurements to ensure that the setup does not introduce bias. Additionally, background noise levels are analyzed to quantify measurement uncertainty.

2. **Steady Uniform Flow Characterization**
   Mean velocity and turbulence intensity are measured under a steady 5 m/s flow to establish baseline conditions. These data are essential for subsequent experiments using the hexapod platform.

3. **Sinusoidal Wind Flow Characterization**
   Calibration tests are conducted to relate WindShape system power settings to actual sinusoidal wind profiles. Following calibration, the system's ability to reliably generate sinusoidal wind is validated. The effect of streamwise (x) position on the characteristics of the sinusoidal flow is also investigated.

4.2 Experimental Setup

Following the objective, this section describes the equipment used to achieve it, along with the capabilities and limitations of the instrumentation, including the robot arm and testing area, to provide context for the experimental procedures that follow.

4.2.1 Available Equipment

Firstly, an overview of the available equipment is provided, detailing the key components essential for the experiments. For full configuration details, see Appendix A.

- **WindShaper:** Composed of multiple wind fans and counter-rotating fans, it eliminates vortex formation by using the counter-rotating fans to simulate natural wind conditions in the wind facility (see Figure 3.2).
- **Plastic wind facility sections:** Installed in a dedicated room, each measuring 75 x 220 x 220 cm, to direct the airflow through and around the facility back to the WindShaper (see Figure 4.1a for all sections depicted along the wind facility).
- **Sensor rake with three TriSonica sensors:** A rigid frame holding three TriSonica ultrasonic anemometers arranged to simultaneously capture three-dimensional wind velocity at multiple points (see Figure 4.2a).
- **Newly 3D-printed sensor rake:** A custom lightweight mount, fabricated via 3D printing, designed for a single TriSonica sensor to allow precise positioning in confined spaces with minimal flow interference (see Figure 4.2b).
- **Robot arm setup:** Provides precise positioning and control, located in plastic sections 6 through 10 (i.e., between 375 cm and 750 cm from the WindShaper) (see Figure 4.1b).

4.2.2 Accessible Measurement Positions

Due to its movement limits, the robot arm could only operate within a certain area. This entire accessible area was used by following a set scanning pattern in the lower part of the wind facility, indicated by the red areas in Figure 4.3. To reach higher points, the arm was rotated 180°, enabling measurements in the green areas shown in the same figure.

(a) Facility setup

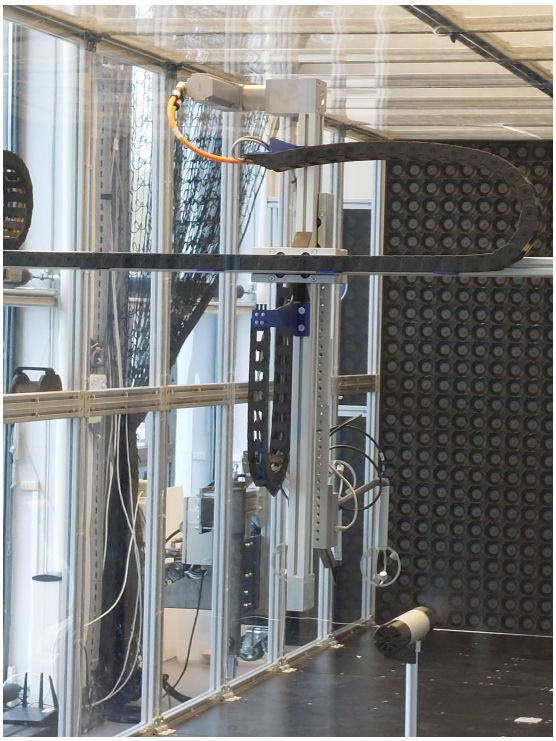

(b) Robot arm used

Figure 4.1: Overview of the experimental facility setup (a) and the robotic arm used for precise sensor positioning (b).

(a) Rake with three TriSonica sensors

(b) Rake for one TriSonica sensor

Figure 4.2: TriSonica sensor configurations: (a) rake with three TriSonica ultrasonic anemometers, and (b) newly 3D-printed rake designed for a single TriSonica sensor.

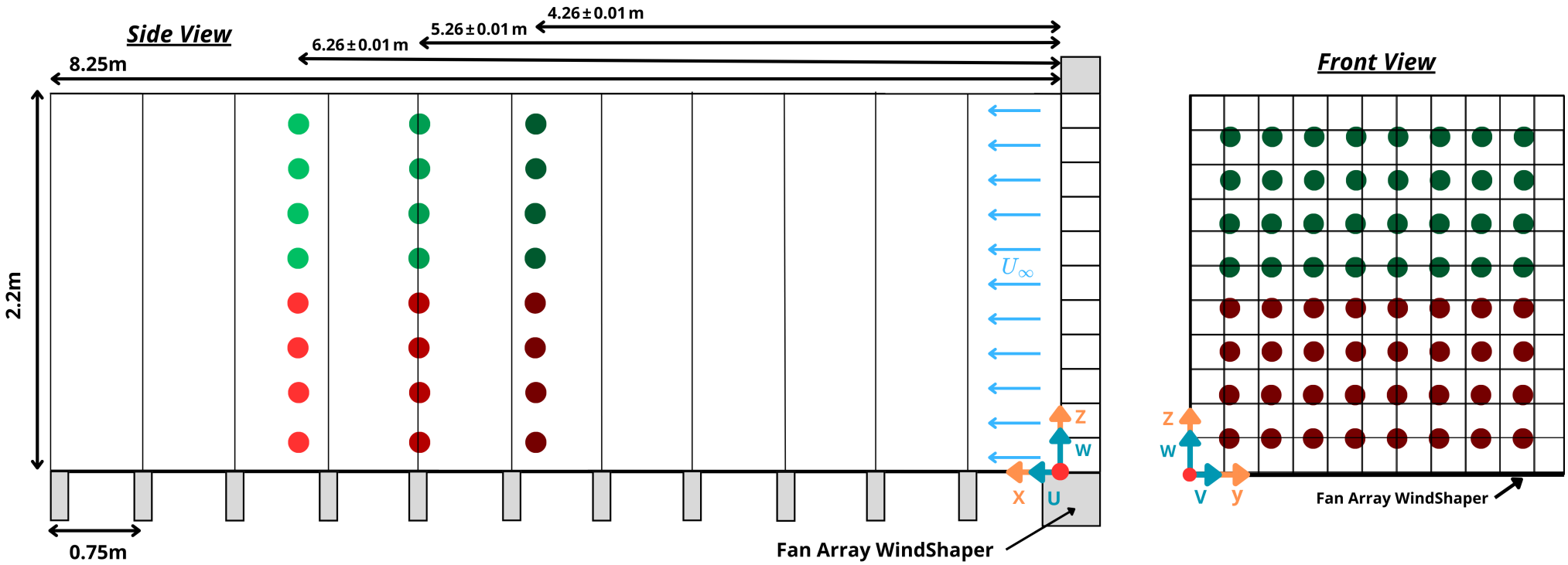

Figure 4.3: Side (left) and front (right) views of the tested positions within the wind facility. Colors indicate different measurement point sets and help illustrate the viewing angles of the wind tunnel. Positive directional axes and velocity vectors are also shown.

4.2.3 Environmental Conditions

The experiments, conducted between February 12 and 19, were affected not only by spatial limitations but also by environmental conditions. Room temperature at the WindAI facility was primarily determined by internal heat sources, as outside temperatures remained consistently lower.

Temperature measurements were recorded during the experiments using the TriSonica sensor. As shown in Figure 4.4, local fluctuations did not exceed ±0.5°C around the mean value, indicating that the air temperature remained stable throughout the test runs.

These fluctuations of ±0.5°C correspond to less than a 0.65% change in kinematic viscosity and Reynolds number (Appendix B), which is negligible for the flow characterization experiments. Therefore, the influence of temperature variations on the results can be considered insignificant.

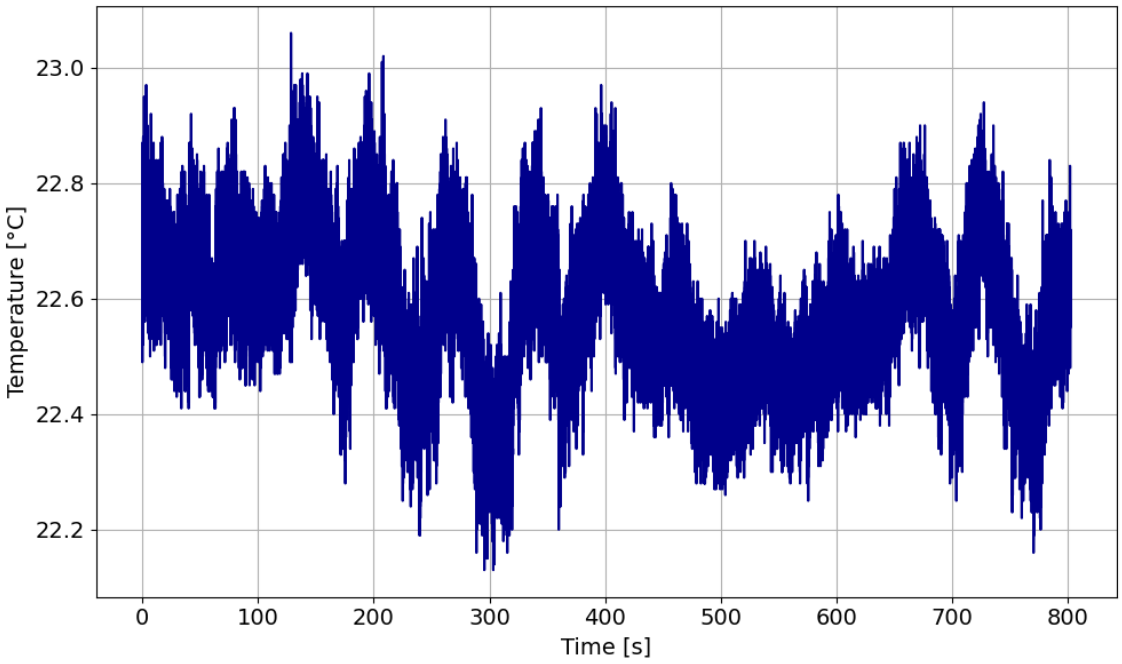

Figure 4.4: Temperature measured by the TriSonica sensor during the experiments at 5 m/s wind velocity. Temperature variations are primarily due to robot repositioning, while the average temperature remained stable throughout the test.

4.3 Experimental Cases

Taking the environmental conditions into account, a series of wind tunnel experiments were conducted to meet the measurement objectives. An overview of the setup and purpose for each experiment is provided in Table 4.1.

Each experimental case was designed to isolate specific flow characteristics. By varying wind speed, oscillation amplitude, and input frequency, the system's response under controlled conditions could be observed, allowing validation of theoretical flow models. The chosen test cases also reflect realistic operating conditions.

Wind input profiles were generated using the Advanced WindShape menu, based on the following equation:

$$\text{Set Amplitude} = A_{\%} \cdot \sin(2\pi f t) + B_{\%} \tag{24}$$

In this expression, $A_{\%}$ sets the oscillation amplitude, $B_{\%}$ defines the mean power level, f is the input frequency in Hz, and t is time in seconds. Increasing $A_{\%}$ simulates stronger gusts, while adjusting f allows investigation of the system's response to faster or slower variations in wind speed.

Prior to the experimental campaign, all measurement instruments were regularly calibrated and checked for proper functioning. This ensured accurate readings and minimized potential systematic errors in the collected data.

Before each run, the wind tunnel and measurement equipment were positioned at the appropriate starting location, depending on the area of the wind tunnel being tested. The measurements were then initiated, following the detailed step-by-step procedure outlined in Appendix C.

Finally, a structured shutdown procedure was followed at the conclusion of each experiment to ensure the safety of both the equipment and personnel. This included shutting down the control programs and equipment, as outlined in Appendix D.

Table 4.1: Overview of Conducted Experiments

Group	Subgroup	Exp. #	Title / Purpose	Wind Condition	Region in Figure 4.3	Scan Timing
1. Measurement setup	Sensor mounting	1	Sensor interference test (all sensors on)	5 m/s ($B = 34\%$)	All Lower	1s + 4s
		2	Repeat of Exp. 1 to test consistency	5 m/s ($B = 34\%$)	All Lower	1s + 4s
		3	Single-sensor test	5 m/s ($B = 34\%$)	All Lower	1s + 4s
	Background noise	4	Background noise	0 m/s ($B = 0\%$)	All Upper	1s + 4s
		5	Background noise	0 m/s ($B = 0\%$)	All Lower	1s + 4s
2. Uniform flow	Baseline measurement	6	Velocity & turbulence intensity	5 m/s ($B = 34\%$)	All Lower	1s + 4s
		7	Velocity & turbulence intensity	5 m/s ($B = 34\%$)	All Upper	1s + 4s
3. Sinusoidal flow	Calibration	8	Calibration of WindShape settings	Trial & error	$x \approx 4000$, $y \approx 1000$	1s + 4s
	0.1 Hz validation	9	1 m/s amplitude	$A = 10\%$, $B = 33\%$	Light Green	1s + 40s
		10	1 m/s amplitude	$A = 10\%$, $B = 33\%$	Light Red	1s + 40s
		11	2 m/s amplitude	$A = 20\%$, $B = 30\%$	Light Green	1s + 40s
		12	2 m/s amplitude	$A = 20\%$, $B = 30\%$	Light Red	1s + 40s
	0.2 Hz validation	13	1 m/s amplitude	$A = 13\%$, $B = 30\%$	Light Green	1s + 20s
		14	1 m/s amplitude	$A = 13\%$, $B = 30\%$	Light Red	1s + 20s
		15	2 m/s amplitude	$A = 28\%$, $B = 30\%$	Light Green	1s + 20s
		16	2 m/s amplitude	$A = 28\%$, $B = 30\%$	Light Red	1s + 20s
	x-position effect	17	Spatial variation	$A = 13\%$, $B = 30\%$	All Upper	1s + 20s
		18	Spatial variation	$A = 13\%$, $B = 30\%$	All Lower	1s + 20s

4.4 Data Analysis Approach

To analyze these cases, this section details the methods used for processing the WindShape tunnel data, focusing on two key metrics: turbulence intensity (TI) and the tunnel's ability to reproduce sinusoidal wind patterns. All analysis code is available in the 4TU.ResearchData repository.

4.4.1 Turbulence Intensity Calculation

Firstly, Turbulence intensity (TI) is a dimensionless measure of the strength of velocity fluctuations relative to the mean flow speed. As discussed in Section 2.4.2, TI can significantly impact experimental outcomes, making it important to characterise. It is defined as the ratio of the root mean square (RMS) of the velocity fluctuations to the mean velocity magnitude.

To compute TI at each point in the measurement domain, the dataset is grouped by spatial coordinates `(x, y, z)`. For each group, the following steps are applied:

1. Calculate the RMS of each velocity component using:

$$u_{\text{rms}} = \sqrt{\frac{1}{N}\sum_{i=1}^{N}(u_i - \bar{u})^2} \tag{25}$$

   and similarly for v_{rms} and w_{rms}.

2. Compute the mean velocity magnitude:

$$|\bar{U}| = \sqrt{\bar{u}^2 + \bar{v}^2 + \bar{w}^2} \tag{26}$$

3. The turbulence intensity is then given by:

$$TI = \frac{\sqrt{u_{\text{rms}}^2 + v_{\text{rms}}^2 + w_{\text{rms}}^2}}{|\bar{U}|} \tag{27}$$

This method enables a spatially resolved estimation of turbulence intensity (TI) throughout the measurement domain. Using these TI values and corresponding velocity data, heat maps are generated to illustrate how flow characteristics vary across different spatial locations.

4.4.2 Theory for Sinusoidal Flow Assessment

Next, to evaluate how well the WindShape tunnel reproduces sinusoidal wind conditions, a representative test case, Experiment 16, was selected for in-depth analysis. This experiment aimed to generate a 0.2 Hz sinusoidal velocity signal with a 2 m/s amplitude, corresponding to control inputs $A\% = 28$ and $B\% = 26$.

At each spatial measurement point, wind velocity was recorded over a 21-second interval, allowing the first second for stabilization and using the remaining 20 seconds for analysis. An example of the raw velocity signal at location $x = 5.26 \pm 0.01m$, $y = 0.29m$, and $z = 0.95m$ is shown in Figure 4.5.

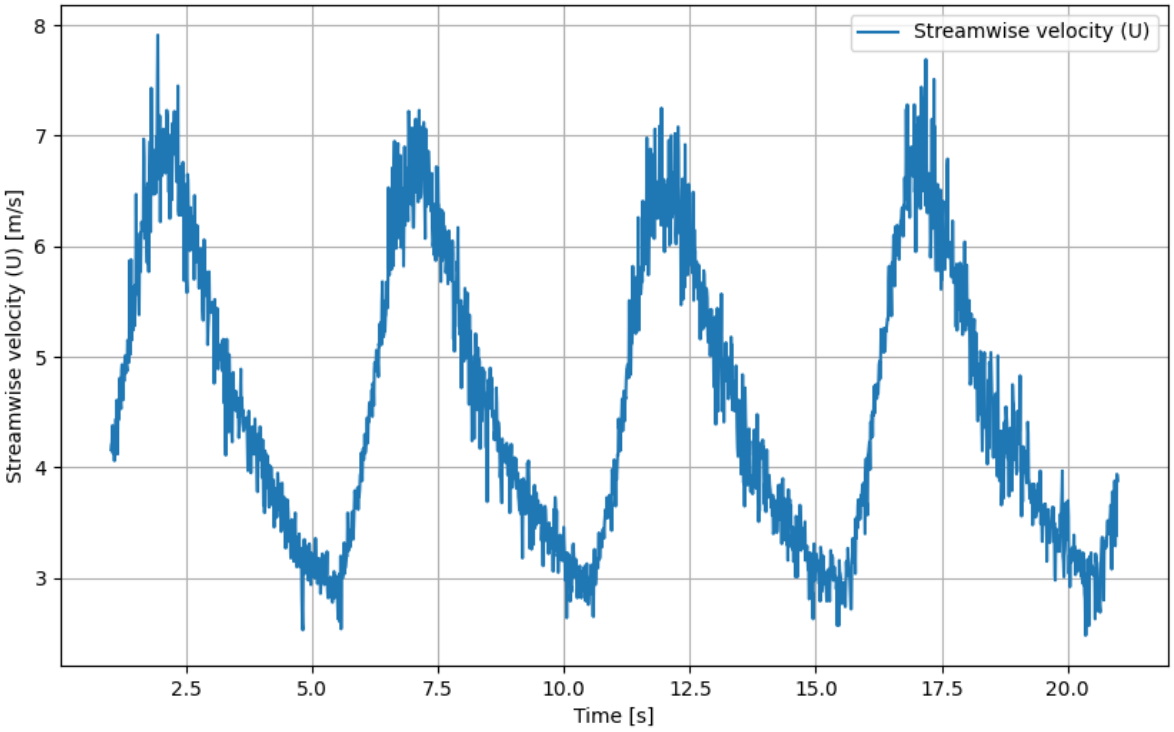

Figure 4.5: Time series of the recorded wind velocity at the measurement location ($x = 5.26 \pm 0.01m$, $y = 0.29m$, $z = 0.95m$) during a 0.2 Hz sinusoidal wind test with 2 m/s amplitude.

To reduce noise and isolate the dominant oscillatory behavior, a phase-averaging technique was applied over a 5-second cycle. This averages multiple periods of the wind signal, smoothing out random fluctuations and revealing the underlying periodic pattern (shown in Figure 4.6). To further characterize the frequency content, a Fourier decomposition was performed, representing the signal as a sum of sine and cosine functions:

$$f(t) \approx A_0 + \sum_{n=1}^{N} \left[A_n \cos\left(\frac{2\pi n t}{T}\right) + B_n \sin\left(\frac{2\pi n t}{T}\right) \right] \tag{28}$$

Here, A_0 is the average (DC offset), while A_n and B_n capture the amplitudes of each harmonic. In this case, only the first three terms were included: A_0, A_1, B_1, A_2, and B_2, corresponding to the mean value, the primary sinusoidal component at 0.2 Hz, and its first harmonic at 0.4 Hz. This limited decomposition highlights both the intended frequency and any subtle deviations from an ideal sine wave.

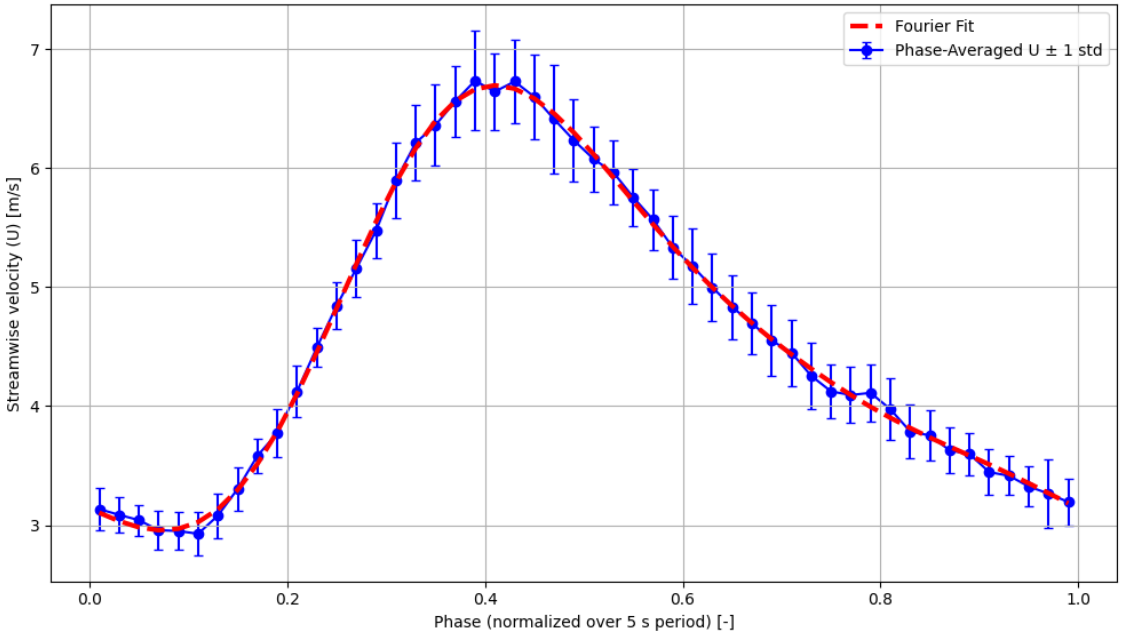

Figure 4.6: Phase-averaged velocity over one 5-second cycle at $x = 5.26 \pm 0.01$ m, $y = 0.29$ m, $z = 0.95$ m during a 0.2 Hz sinusoidal test with 2 m/s amplitude. Averaging data within each phase bin over multiple periods reduces noise and reveals the consistent oscillatory response of the wind tunnel. Error bars show the standard deviation at each phase. The measured velocity deviates from a perfect sinusoid, indicating that the tunnel reproduces the imposed oscillation with systematic distortions rather than random noise.

To quantify how closely the measured waveform matches the ideal sinusoid, the root mean square (RMS) error is computed. This metric calculates the square root of the average squared differences between the measured and ideal signals over time. In other words, it captures the typical magnitude of deviation throughout the cycle. Lower RMS values indicate a waveform that more closely follows the ideal sinusoidal shape. An example comparison between a measured waveform and its ideal counterpart is shown in Figure 4.7, where the RMS error was 0.7432 m/s.

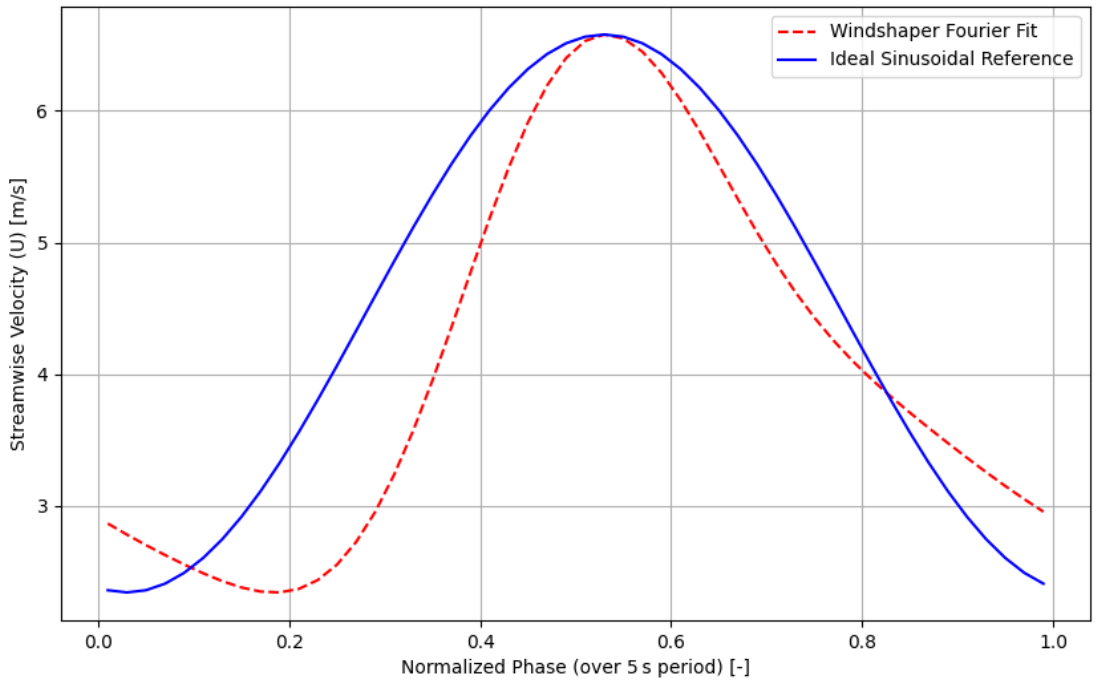

Figure 4.7: Comparison of the measured wind velocity waveform at location $(x, y, z) = (5.26 \pm 0.01m, 0.29m, 0.95m)$ *with an ideal 0.2 Hz sinusoidal signal of 2 m/s amplitude, over one full 5-second cycle. The root mean square (RMS) error between the measured signal and the reference sinusoid is 0.7432 m/s.*

This approach forms the basis for generating RMS error maps across the entire measurement domain, quantifying the tunnel's performance in reproducing the desired time-varying wind conditions consistently across the experimental domain.

4.5 Findings of Flow Characterization

Now that all elements are in place, this section summarizes findings from experiments evaluating the WindAI facility's consistency in reproducing realistic flow conditions.

4.5.1 Measurement Setup Verification

As previously discussed, the measurement setup first required verification. In Experiments 1 and 2, all three TriSonica sensors were active, and the wind speed was set to 5 m/s. The turbulence intensity measured at different points in the test subsection is shown in Figure 4.8. These results show unexpectedly high turbulence intensity at some locations, along with some irregular patterns in the data.

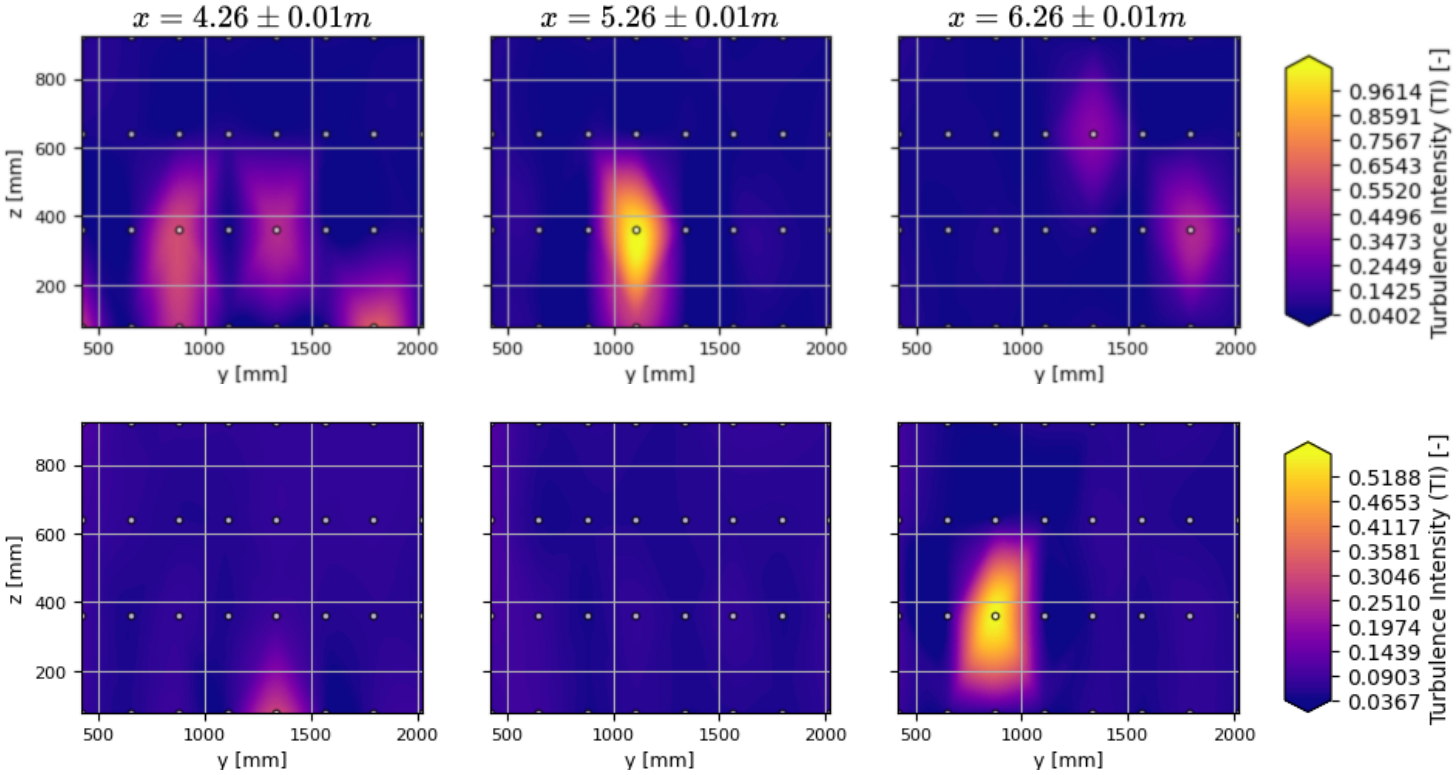

Figure 4.8: Turbulence intensity measurements for Experiments 1 and 2, showing the zy plane at $x = 4.26 \pm 0.01\,\mathrm{m}$, $x = 5.26 \pm 0.01\,\mathrm{m}$, *and* $x = 6.26 \pm 0.01\,\mathrm{m}$ *from left to right. The results reveal high turbulence intensities and irregular spatial patterns, likely influenced by the sensor mounting configuration. All three TriSonica sensors were active in both cases. Note that this experiment only measured the lower region.*

In Experiment 3, only one TriSonica sensor was turned on, and the other two were turned off. The results from this setup are shown in Figure 4.9. In this case, no unusually high turbulence values were seen. The average turbulence intensity was 8.67%, with a standard deviation of 1.06%. This suggests that using multiple sensors at the same time may have affected the earlier results.

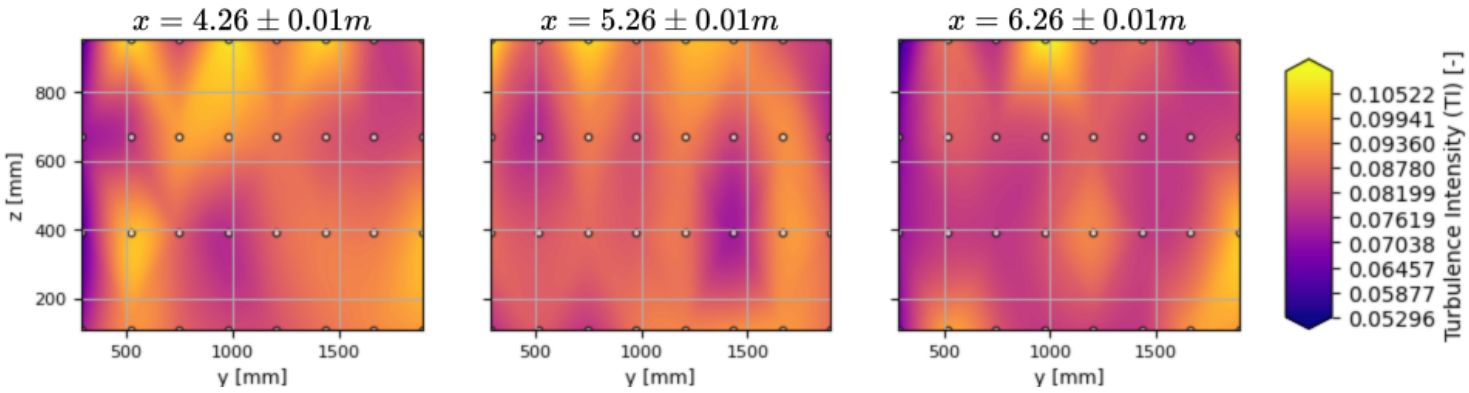

Figure 4.9: Turbulence intensity measurements for Experiment 3, showing the lower region of the zy plane at $x = 4.26 \pm 0.01\,\text{m}$, $x = 5.26 \pm 0.01\,\text{m}$, and $x = 6.26 \pm 0.01\,\text{m}$ from left to right. Only one TriSonica sensor was active. The results show a more uniform distribution and no unusually high values, suggesting that the elevated turbulence levels in earlier experiments may have been influenced by interference between simultaneously active sensors. Note that this experiment only measured the lower region.

When the wind tunnel was turned off, velocity components were measured to quantify background noise. Values remained close to zero, with $U = -0.054 \pm 0.060$ m/s, $V = -0.147 \pm 0.201$ m/s, and $W = -0.165 \pm 0.158$ m/s, indicating minimal residual flow and a stable baseline. While no clear spatial trends were observed in any of the velocity components, small biases relative to the standard deviations were noted (see Appendix E). These minor deviations fall within the expected range of measurement uncertainty and are not expected to meaningfully influence the experimental results or their interpretation.

4.5.2 Steady Uniform Flow Characterization

With the measurement setup validated, velocity measurements were subsequently conducted under uniform wind conditions of 5 m/s. The turbulence intensity averaged 8.0%, with a standard deviation of 0.18% (see Figure 4.10). However, due to unresolved high-frequency components in the temporal spectrum, stemming from limited measurement resolution, the true turbulence intensity is expected to be slightly higher, with an adjustment on the order of $\sim 1\%$ (see Appendix F).

An overview of the velocity components U, V, and W is provided in Figure 4.11, showing slices in the zy plane at $x = 4.26 \pm 0.01\,\text{m}$, $x = 5.26 \pm 0.01\,\text{m}$, and $x = 6.26 \pm 0.01\,\text{m}$ from left to right. The mean streamwise velocity U across all positions in the measurement domain is 4.83 m/s, with a standard deviation of 0.21 m/s reflecting spatial variations of the local mean values. In contrast, the transverse component V averages $0.054 \pm 0.150\,\text{m/s}$, and the vertical component W averages $-0.049 \pm 0.039\,\text{m/s}$, both remaining small in magnitude. The small, seemingly random spatial variations observed in Figure 4.11 likely reflect measurement uncertainty, suggesting that the true variability of the flow is probably smaller than indicated. These results confirm the uniformity of the inlet flow and suggest minimal cross-flow or vertical motion within the measurement domain.

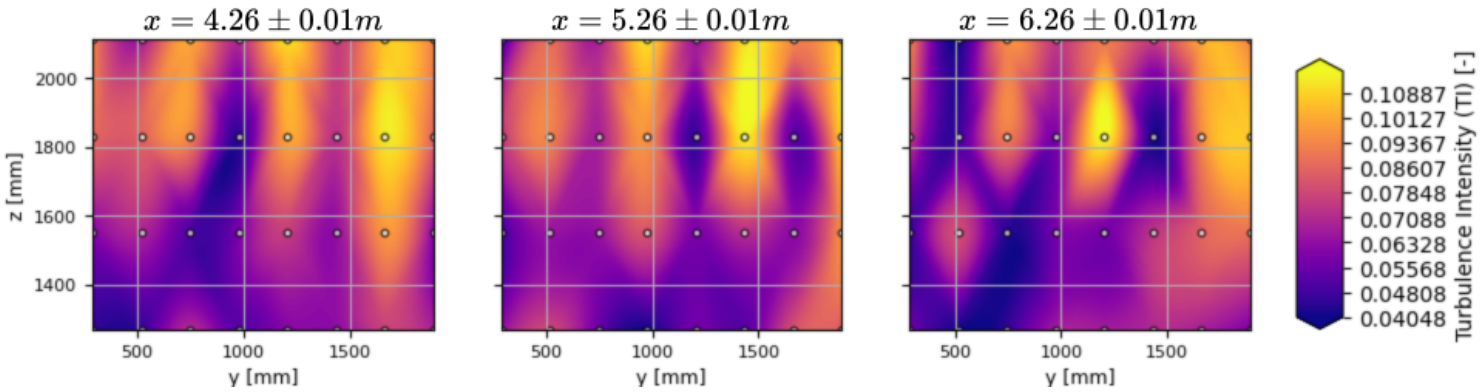

Figure 4.10: Measured turbulence intensity for a uniform 5 m/s wind, showing both lower and upper regions of the zy plane at $x = 4.26 \pm 0.01\,\text{m}$, $x = 5.26 \pm 0.01\,\text{m}$, and $x = 6.26 \pm 0.01\,\text{m}$ from left to right. This is a separate experiment from Figure 4.9; the lower region in this figure was not measured in Experiment 3. The average turbulence intensity is 8.0% with a standard deviation of 0.18%, though this is likely underestimated due to spectral resolution limitations (see Appendix F).

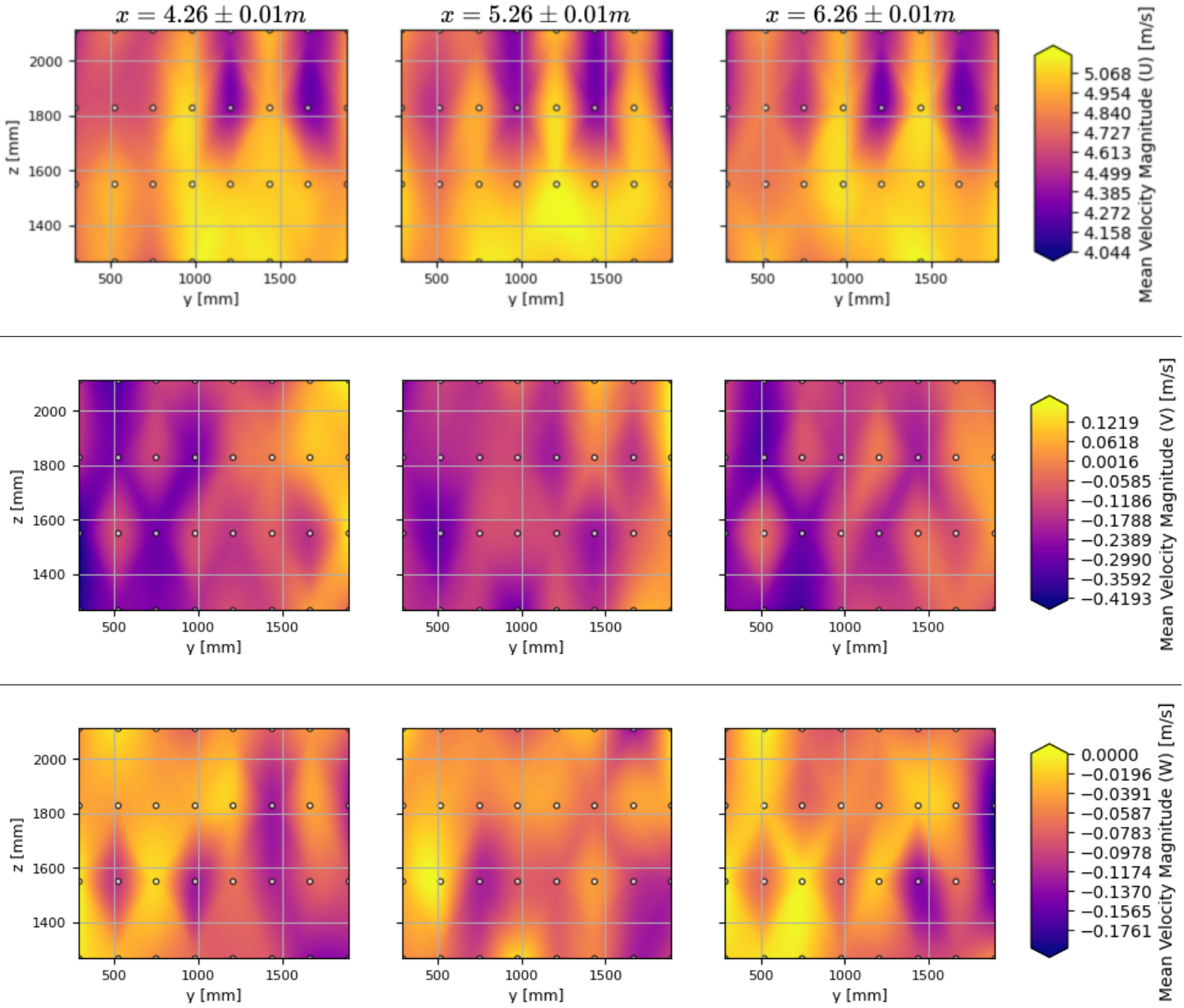

Figure 4.11: Measured velocity components U (top), V, and W (bottom) under a uniform 5 m/s wind, shown across the zy plane at $x = 4.26 \pm 0.01$ m, $x = 5.26 \pm 0.01$ m, and $x = 6.26 \pm 0.01$ m from left to right. The flow is dominated by the streamwise U-component (4.83 ± 0.21 m/s, while the crosswise V-component (0.0538 ± 0.1502 m/s) and vertical W-component (-0.0486 ± 0.0386 m/s) show only minor deviations—highlighting a nicely uniform inflow.

4.5.3 Sinusoidal Wind Flow Characterization

Following the uniform flow measurements, the focus now shifts to evaluating the sinusoidal flow conditions. Experiment 8 involved adjusting the settings of the WindShape system and measuring at the centre of the wind tunnel. The measurements were analyzed to determine the achievable wind pattern.

At higher frequencies and amplitudes, the WindShape fans could not follow the full sinusoidal command, keeping the wind speed above a minimum and preventing the sinusoid from reaching the intended lower velocities (see Figure 4.12).

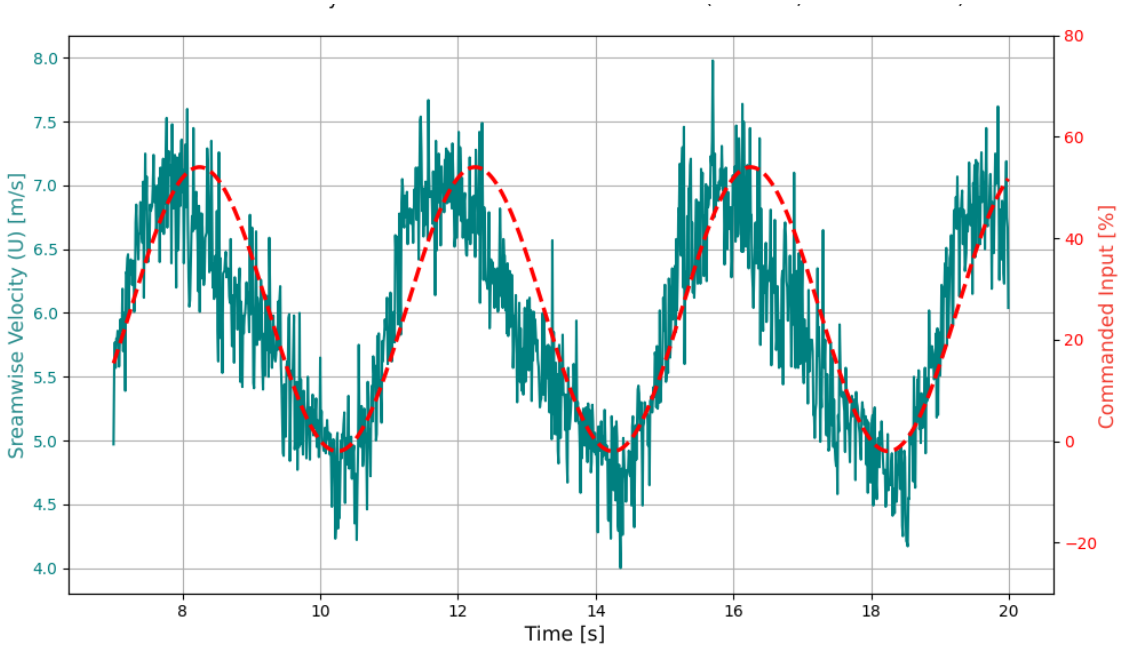

Figure 4.12: Measured wind velocity and corresponding commanded sinusoidal input at high frequency. The input, defined by $A_{\%} = 28$, $B_{\%} = 26$, and $f = 0.25$ Hz, was intended to generate wind oscillations around 5 m/s with a 2 m/s amplitude. While the start time of the command is approximate, the comparison illustrates how the WindShape fans struggle to keep up with rapid fluctuations.

Following the outlined methodology, feasible settings were limited to 0.1 Hz and 0.2 Hz frequencies with amplitudes of 1 m/s and 2 m/s, as shown in Figure 4.13,4.14. Attempts at higher frequencies and amplitudes were unsuccessful due to fan limitations. Despite using sinusoidal inputs from the Advanced WindShape Menu based on Equation 24, the parameters $A_{\%}$ (amplitude) and $B_{\%}$ (offset) did not linearly translate to wind speeds. The system's nonlinear response required iterative trial-and-error tuning to approximate the desired velocity patterns.

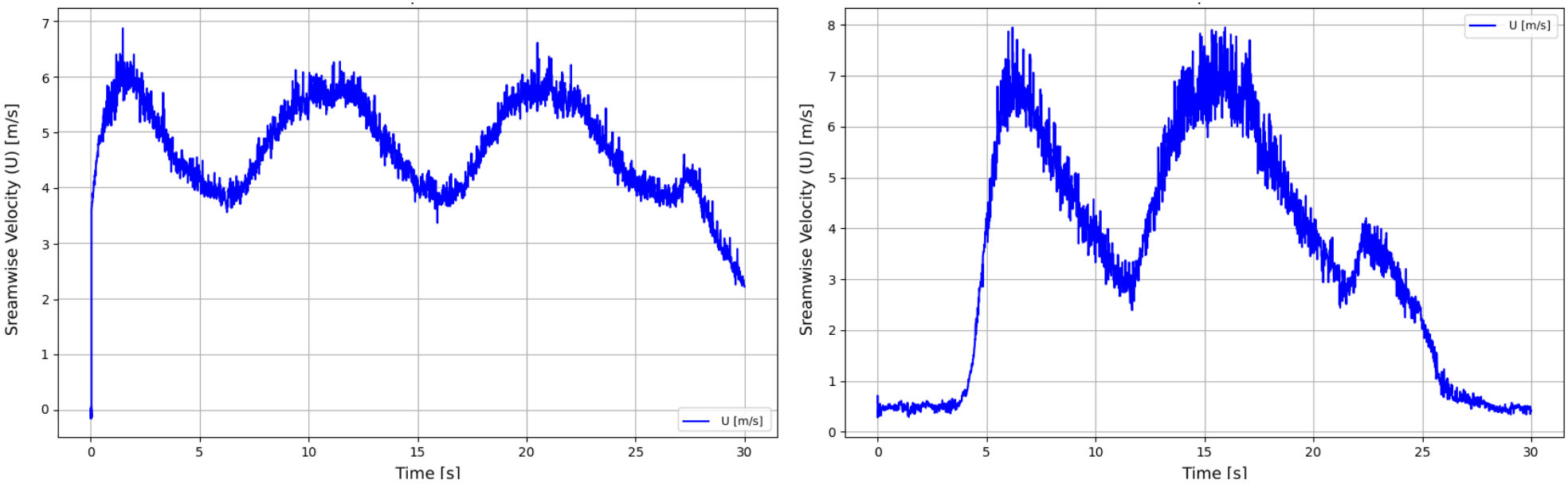

Figure 4.13: Left: Wind pattern at 0.1 Hz with a 1 m/s amplitude, generated using fan parameters $A_{\%} = 25$, $B_{\%} = 10$. Right: Wind pattern at 0.1 Hz with a 2 m/s amplitude, generated using fan parameters $A_{\%} = 20$, $B_{\%} = 30$.

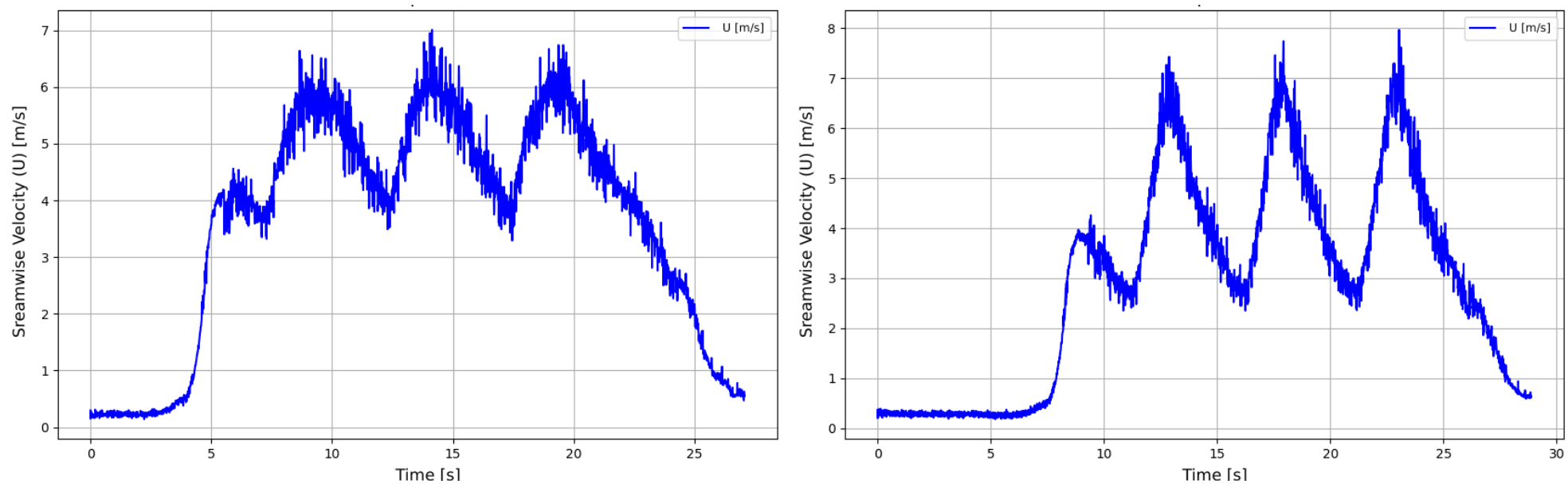

Figure 4.14: Left: Wind pattern at 0.2 Hz with a 1 m/s amplitude, generated using fan parameters $A_{\%} = 13$, $B_{\%} = 30$. Right: Wind pattern at 0.2 Hz with a 2 m/s amplitude, generated using fan parameters $A_{\%} = 28$, $B_{\%} = 26$.

To assess how well the WindShape tunnel replicates sinusoidal wind patterns across space, the root mean square (RMS) error of the measured wind velocity relative to the commanded sinusoidal input was computed at every measurement point. Figures 4.15 and 4.16 show these RMS error maps for test cases at 0.1 Hz and 0.2 Hz with amplitudes of 1 m/s and 2 m/s, respectively. Higher RMS errors occur near the tunnel edges, indicating that the wind waves are less accurately reproduced in those regions.

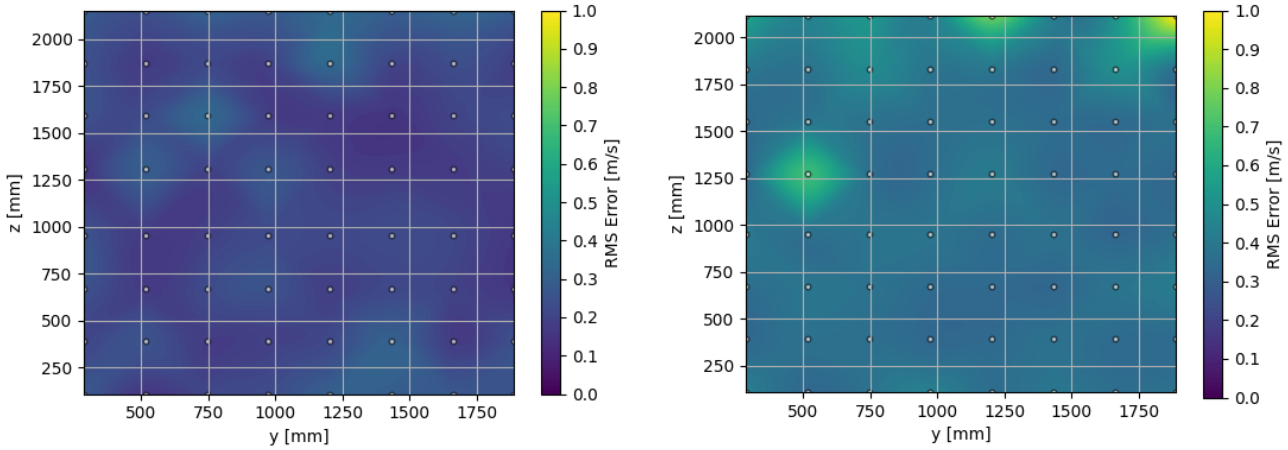

Figure 4.15: RMS error map over the y-z plane at $x = 5.26 \pm 0.01\,\mathrm{m}$, illustrating how the measured waveform compares to ideal 0.1 Hz sinusoids with left figure 1 m/s and right figure 2 m/s amplitudes during a full 5-second cycle.

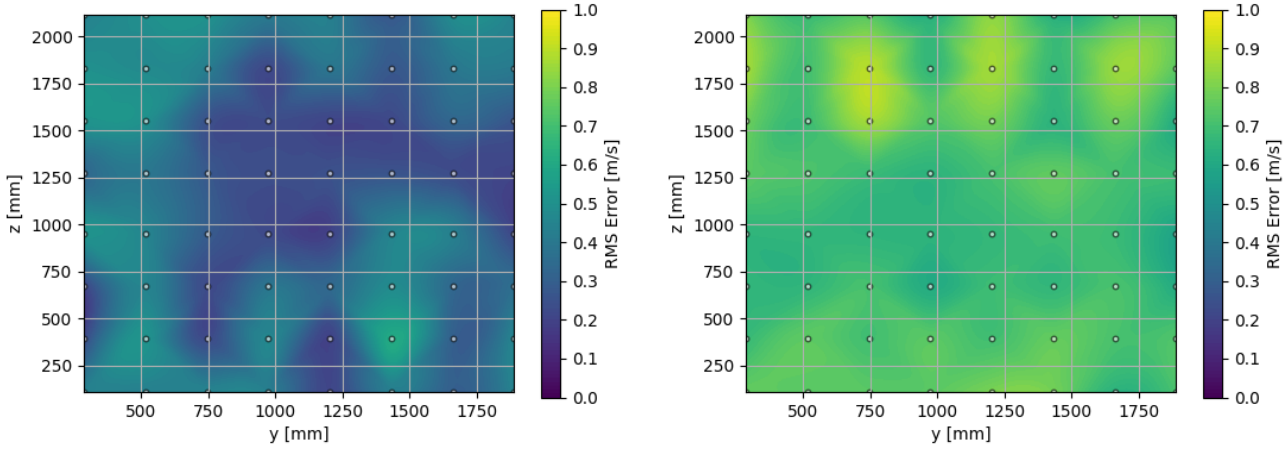

Figure 4.16: RMS error map over the y-z plane at $x = 5.26 \pm 0.01\,\mathrm{m}$, illustrating how the measured waveform compares to ideal 0.2 Hz sinusoids with left figure 1 m/s and right figure 2m/s amplitudes during a full 5-second cycle.

The average RMS errors for each case are shown in Table 4.2.

Frequency [Hz]	Velocity [m/s]	RMS Error [m/s]
0.1	1	0.23 ± 0.05
0.1	2	0.40 ± 0.11
0.2	1	0.36 ± 0.11
0.2	2	0.71 ± 0.07

Table 4.2: Average RMS error for different frequencies and inflow velocities.

These results suggest that waveform accuracy decreases with increasing frequency and amplitude, likely because the WindShape system struggles to keep up with faster or more extreme fluctuations.

To explore how spatial x-positions influence the quality of sinusoidal wind patterns, RMS error heatmaps were analyzed at three streamwise locations ($x = 4.26 \pm 0.01\,\text{m}$, $x = 5.26 \pm 0.01\,\text{m}$, and $x = 6.26 \pm 0.01\,\text{m}$); see Appendix G. The corresponding average RMS errors were $0.35 \pm 0.11\,\text{m/s}$, $0.34 \pm 0.11\,\text{m/s}$, and $0.38 \pm 0.15\,\text{m/s}$, respectively. While the differences are modest, a subtle trend emerges: further downstream, the sinusoidal waveforms become slightly more distorted, likely due to accumulating effects of turbulence, small flow instabilities, or edge influences. In short, the farther the wave travels, the more it wobbles from its ideal path.

4.6 Conclusion

To ensure reliable conditions for vertical-axis wind turbine (VAWT) testing, the WindAI facility was evaluated for its ability to generate controlled wind profiles. This involved assessing measurement accuracy, turbulence in steady flows, and the facility's ability to replicate sinusoidal wind patterns.

The measurement setup showed that mounting of the TriSonica sensor affected data quality. When only one TriSonica sensor was active, turbulence intensity dropped and erratic spikes disappeared, suggesting interference (likely acoustic) between sensors. Therefore, all further tests used a single active sensor. Background measurements confirmed velocity readings remained centered near zero throughout the test volume, with only minor directional biases.

The tunnel produced a steady and reliable flow around the target 5 m/s. The mean streamwise velocity was 4.83 ± 0.21 m/s, while transverse and vertical components remained small ($V = 0.054 \pm 0.150$ m/s, $W = -0.049 \pm 0.039$ m/s), indicating minimal flow deviation. Turbulence intensity averaged $8\% \pm 0.18\%$, and is estimated to be slightly higher, around 9%, when accounting for unresolved high-frequency components. These results demonstrate that the setup is suitable for clean and repeatable aerodynamic measurements.

Sinusoidal wind patterns were successfully generated at 0.1–0.2 Hz with amplitudes up to 2 m/s. Beyond this range, waveform accuracy degraded as the fans could not keep up with rapid fluctuations. RMS errors increased with frequency and amplitude, ranging from 0.23 ± 0.05 m/s to 0.71 ± 0.07 m/s. Accuracy was highest in the tunnel center and varied only slightly along the x-direction. However, these errors were too large for high-precision experiments. A hexapod system will therefore be used to generate more accurate sinusoidal wind profiles.

Compared to typical wind tunnels with turbulence intensities of 0.5–1.0% [38], WindAI exhibits higher baseline turbulence. This limits its use in high-precision turbulence studies but makes it well-suited for early-stage experimental research.

These results show that WindAI performs well under steady conditions and provides a strong platform for early-stage VAWT testing. For future work, improving turbulence resolution should be prioritized. Smaller-volume sensors, such as Oxford probes or hot-wire anemometry, could better resolve fine-scale structures and quantify energy missed by the TriSonica. Automating WindShape fan calibration may also enhance repeatability under dynamic conditions. For long-term or high-precision campaigns, fully characterised facilities like the OJF remain the benchmark.

5. Wind Turbine Design

Following the wind characterization, this section outlines the design and construction process of the wind turbine prototype, covering initial calculations, 3D modeling, iterative design refinements, manual development, component procurement, and validation.

5.1 Design Requirements

The first step in the construction process was to create a comprehensive manual to ensure reproducibility and ease future testing or redesigns. The manual includes:

1. **Wind Facility Compatibility**
   The turbine was designed to fit within the WindShape wind facility. Its height was constrained to keep the blade tips below the boundary layer region, avoiding distorted measurements from non-uniform flow.

2. **Hexapod Mounting and Center of Mass Alignment**
   To enable dynamic testing, the turbine was mounted directly onto a hexapod platform. The design ensured that the center of mass aligned with the hexapod's connection point, minimizing vibrations and improving mechanical stability.

3. **Aerodynamic Cleanliness**
   The support structure was streamlined to minimize its influence on the incoming flow, helping to isolate blade-related aerodynamic effects from upstream interference.

4. **Geometric Scaling for Experimental Relevance**
   Key dimensionless parameters—such as Reynolds number and tip-speed ratio (λ)—were chosen to match values found in existing research. This ensures that results are both scalable and comparable.

5. **Integrated Safety and Control Features**
   A bicycle brake was installed to stop rotation rapidly in case of malfunction or excessive speed. Additionally, a motor was included in the drivetrain to allow active control of the rotational speed, which is essential for experiments with time-varying (e.g., sinusoidal) wind inputs.

6. **Instrumentation and Data Acquisition**
   A torque sensor was installed to measure the mechanical response of the turbine under load. All sensors and actuators were configured to interface with the dSPACE MicroLabBox, allowing for synchronized high-frequency sampling and closed-loop control during testing.

These design considerations ensured the turbine prototype was both functional and compatible with the testing environment. With these constraints addressed, the next step involves performing preliminary calculations to further refine the turbine's expected performance and guide the experimental setup.

5.2 Preliminary Calculations

Before the mechanical modeling began, several key calculations were performed to guide design decisions. These calculations focused on structural integrity, motor requirements, and aerodynamic relevance.

5.2.1 Dimensions of the Wind Turbine

Before proceeding with the calculations, it is necessary to define the scope of the analysis. The relevant variables are listed in Section 3.2.1; here, they are assigned values. The initial design features a radius of $R = 0.25\,\mathrm{m}$. However, to reduce structural vibrations, the final design increased the radius to $R = 0.50\,\mathrm{m}$. The total blade height was $H = 0.45\,\mathrm{m}$, and the chord length was $L = 0.075\,\mathrm{m}$. The projected swept area for a vertical-axis wind turbine (VAWT) is given by (Equation 16):

$$A = D \cdot H = 2 \cdot 0.50\,\mathrm{m} \cdot 0.45\,\mathrm{m} = 0.45\,\mathrm{m}^2$$

For a one-bladed configuration, the solidity ratio is (Equation 20):

$$\sigma = \frac{N \cdot L}{2 \cdot R} = \frac{1 \cdot 0.075}{1.0} = 0.075$$

The Reynolds number, based on the diameter and a freestream wind velocity of $U = 5\,\mathrm{m/s}$, using the kinematic viscosity of air $\nu = 1.48 \times 10^{-5}\,\mathrm{m}^2/\mathrm{s}$, is (Equation 18):

$$Re_D = \frac{UD}{\nu} = \frac{5 \cdot 1.00}{1.48 \times 10^{-5}} \approx 3 \times 10^5$$

This Reynolds number suggests the flow is within the laminar to transitional regime around the blade section [48]. Although it does not fully reach the turbulent regime,

limitations in tunnel size and operational wind speeds, restricted due to acoustic constraints, defined this practical upper bound. Furthermore, the relatively rough surface finish of the 3D-printed blades is expected to trigger boundary-layer transition close to the leading edge, thereby reducing the dependence of aerodynamic performance on Reynolds number.

5.2.2 Motor Selection Based on Torque Requirements

The heart of this wind turbine is the motor, but what size should it be? This section answers that question by calculating the average aerodynamic torque, $\bar{\tau}$, which can be estimated from the power coefficient C_p using:

$$C_p = \frac{\bar{\tau}\,\Omega}{\frac{1}{2}\,\rho\,A\,U_\infty^3} \quad \Rightarrow \quad \bar{\tau} = \frac{C_p\,(\frac{1}{2}\,\rho\,A\,U^3)}{\Omega}. \tag{29}$$

Assuming the (theoretical maximum) Betz limit $C_p = 0.593$ [11], and using:

$$\rho = 1.225\,\mathrm{kg/m^3}, \quad \Omega = 25\,\mathrm{rad/s},$$

the resulting average torque is:

$$\bar{\tau} \approx \frac{0.593 \cdot \frac{1}{2} \cdot 1.225 \cdot 0.45 \cdot 125}{25} = 0.82\,\mathrm{Nm}.$$

To ensure robust operation under dynamic conditions, a motor with a continuous torque rating of at least 1 Nm is advised, incorporating a $\approx 20\%$ safety margin.

5.2.3 Structural Support and Shaft Sizing

To prevent the wind turbine from breaking mid-rotation, the vertical shafts must withstand both the rotor's weight and the centrifugal forces generated during spinning. Calculations follow standard beam theory from [54]. Each shaft is modeled as a circular steel beam with radius $r = 4.0\,\mathrm{mm}$, giving a second moment of inertia:

$$I = \frac{\pi r^4}{4} = 2.0 \times 10^{-10}\,\mathrm{m^4}. \tag{30}$$

The rotor assembly weighs approximately 0.64 kg, consisting of 3D-printed PETG blades and two steel support rods (6.0 mm and 8.0 mm in diameter, each 0.50 m long). Each shaft carries half the weight:

$$P_\delta = \frac{mg}{2} = \frac{0.64 \times 9.81}{2} = 3.1\,\mathrm{N}. \tag{31}$$

For a simply supported span of $L_{rod} = 0.50\,\text{m}$, vertical deflection under gravity is:

$$\delta_{\text{ver}} = \frac{P_\delta L_{rod}^3}{3EI} = \frac{3.1 \times (0.50)^3}{3 \times 2.1 \times 10^{11} \times 2.0 \times 10^{-10}} = 3.0\,\text{mm}, \tag{32}$$

which becomes $\delta_{\text{ver,single}} \approx 1.5\,\text{mm}$ per shaft. For centrifugal loading at $\Omega = 30\,\text{rad/s}$ and radius $R = 0.50\,\text{m}$, the outward force is:

$$F_{\text{rad}} = m\Omega^2 R = 0.64 \times 30^2 \times 0.50 \approx 290\,\text{N}. \tag{33}$$

Wind force at $|\vec{U}_{rel}| = 5\,\text{m/s}$ on a flat plate with dimensions $H = 0.45\,\text{m}$, $L = 0.075\,\text{m}$, and drag coefficient $C_D = 1.2$ [55], is (Equation 7):

$$F_{\text{drag}} = \frac{1}{2}\rho A_{blade} C_D(\alpha)|\vec{U}_{rel}|^2 = 0.5 \times 1.225 \times 1.2 \times (0.45 \times 0.075) \times 25 = 0.6\,\text{N}.$$

This is negligible compared to the centrifugal force. Assuming the centrifugal force is uniformly distributed, the load per unit length is:

$$w_\delta = \frac{F_{\text{rad}}}{H} = \frac{290}{0.45} \approx 640\,\text{N/m}. \tag{34}$$

With both ends of the shaft fixed, the maximum horizontal deflection is:

$$\delta_{\text{horiz}} = \frac{w_\delta L_{rod}^4}{384EI} \approx \frac{640 \times (0.50)^4}{384 \times 2.1 \times 10^{11} \times 2.0 \times 10^{-10}} = 2.5\,\text{mm}, \tag{35}$$

which is halved for two shafts: $\delta_{\text{ver,single}} \approx 1.25\,\text{mm}$. The allowable blade deflection is not explicitly specified for small VAWT blades. As a conservative engineering guideline, a maximum deflection of $L/180 \approx 2.8\,\text{mm}$ is considered, following common structural design practices [56]. Thus an 8 mm diameter steel shaft with a 0.5 m span provides sufficient stiffness to ensure safe operation of the turbine.

5.3 CAD Modeling and Design Setup

Building on the safety calculations and chosen dimensions, this section walks through the creation of the 3D model, setting up the turbine in the test environment together with the code that realizes the implementation.

5.3.1 Computer-Aided Design Modeling of Turbine Design

To support the design and construction of the wind turbine, a 3D model was created in SolidWorks (see Figure 5.1). The Computer-Aided Design (CAD) model served as the foundation for design validation and later construction. Multiple iterations were made to refine the blade profile, ensure manufacturability, and simplify assembly. The CAD model is available in the 4TU.ResearchData repository.

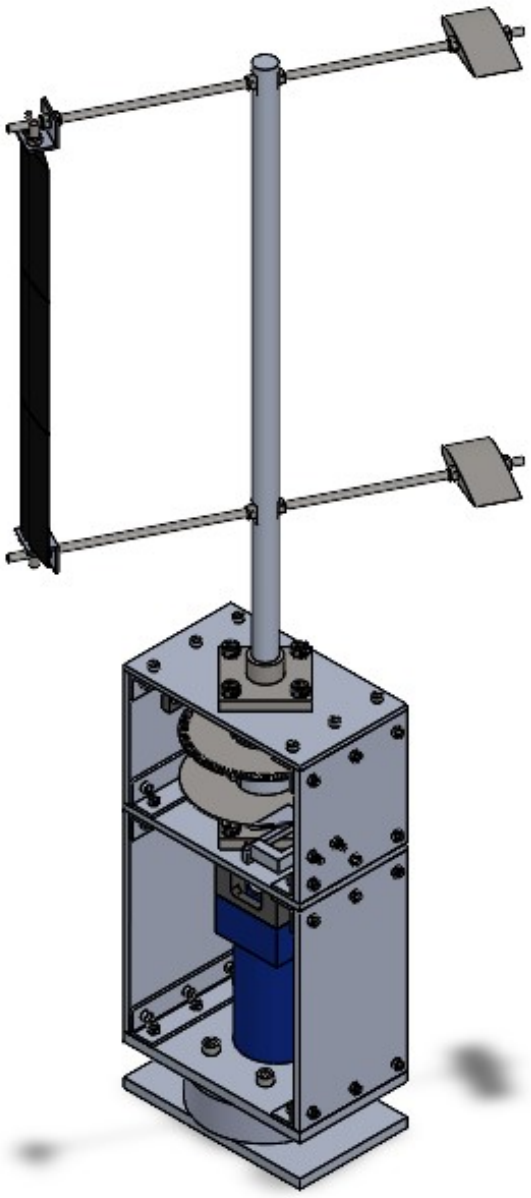

Figure 5.1: Isometric view of the full wind turbine assembly modeled in SolidWorks. This render shows the overall geometry and layout of the design; details and annotations of individual components are provided in the following figures. This figure shows the wind turbine model with an initial blade radius of $R = 0.25m$ (later increased to $R = 0.5m$).

Following the full assembly view, specific components of the wind turbine are highlighted to provide a clearer understanding of the design. First, the torque sensor and first platform are shown in Figure 5.2, followed by the second platform in Figure 5.3, and finally the single-blade rotor in Figure 5.4.

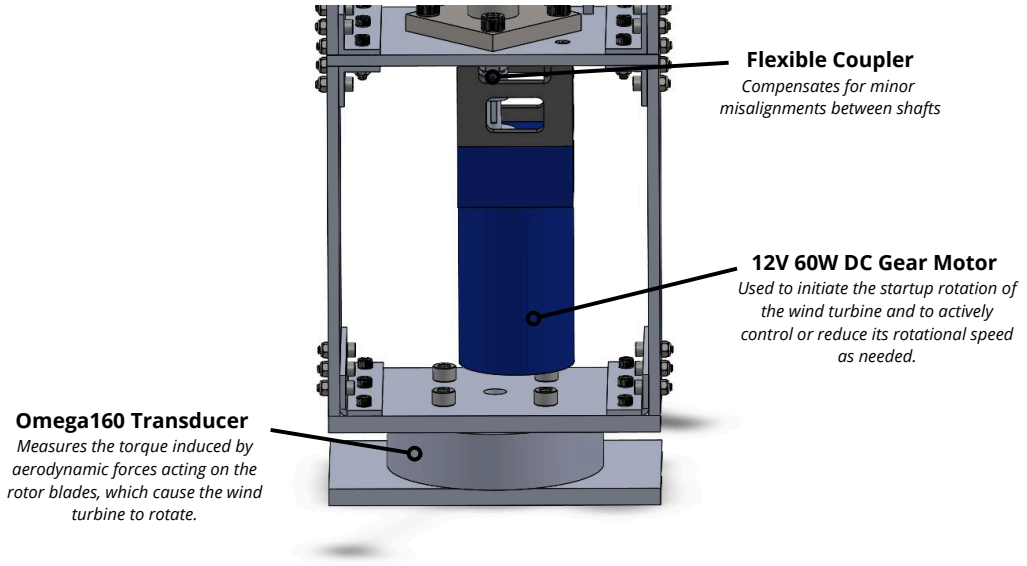

Figure 5.2: Detail view highlighting the torque sensor, first platform, motor, and flexible coupler. These components provide the structural base, torque measurement, and rotational connection for the turbine setup.

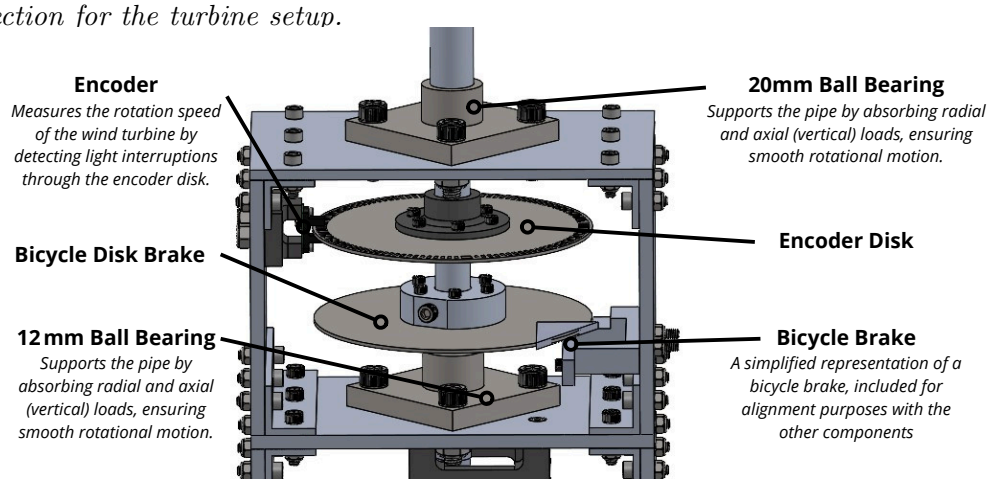

Figure 5.3: The second platform, which supports the upper bearing and allows vertical alignment adjustments. This view also shows the encoder and encoder disk for rotational measurement, as well as the disk brake and bicycle brake for torque control and safety.

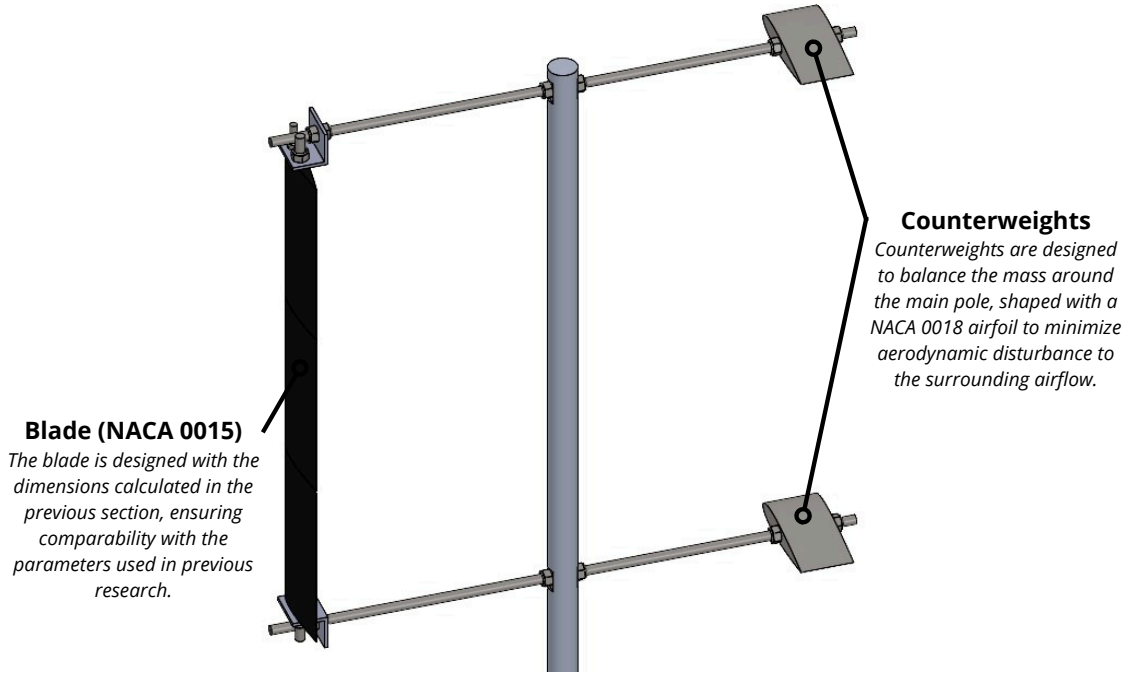

Figure 5.4: Close-up view of the single-blade rotor, illustrating the NACA 0015 airfoil connected to the central shaft and the counterweights used for balancing. The mounting connection to the shaft is also visible.

5.3.2 Setup of Turbine Design

With the CAD model completed, the next step is to implement the turbine's electrical system. Figure 5.5 shows the circuit schematic, mapping out how all the components connect. The operational principle is as follows:

The encoder measures the angular velocity of the turbine and transmits this data to the dSPACE controller. The dSPACE system records the measurements for analysis, while the motor input percentage, predetermined to achieve the desired angular velocity, is supplied directly to the H-bridge. The H-bridge directs power through a relay circuit, which can immediately stop the motor and wind shaper in the event of an emergency. Otherwise, power flows uninterrupted to the motor, which maintains the turbine speed according to the preset input.

Simultaneously, a torsion sensor measures the forces acting on the wind turbine and sends this information to the dSPACE controller. The processed data is then transmitted through a network switch to the user's PC for real-time monitoring and data acquisition.

Regarding the hexapod positioning system, position commands are sent to a dedicated hexapod PC located inside the wind tunnel. This PC interfaces with a network switch that relays position data to the user PC. Alternatively, the switch can be configured to send predefined position commands to the hexapod, enabling precise control of its movements.

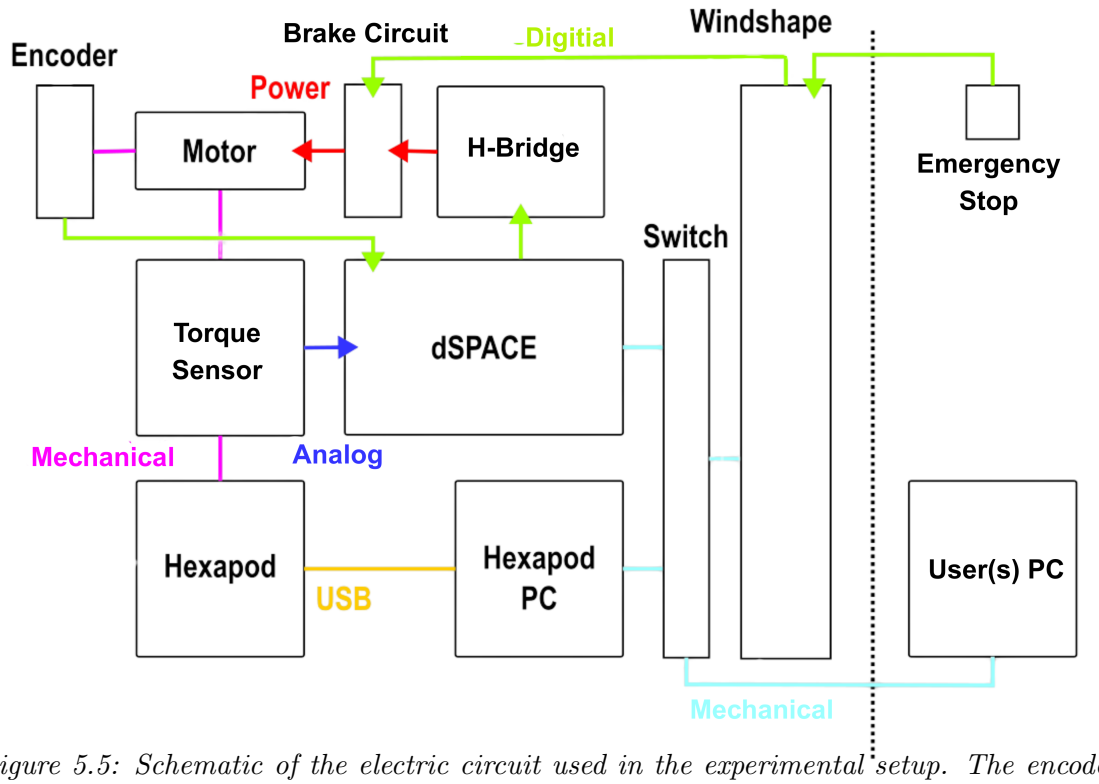

Figure 5.5: Schematic of the electric circuit used in the experimental setup. The encoder measures the turbine's angular velocity and sends the data to the dSPACE controller for recording and analysis. The motor input, predetermined to achieve the desired turbine speed, is supplied to the H-bridge. Power passes through a relay for emergency shutoff before reaching the motor. A torsion sensor sends force data to dSPACE for monitoring via the user PC. The hexapod positioning system is controlled via a dedicated PC connected to the network switch, allowing for real-time or preprogrammed movement commands.

5.3.3 Control Implementation

Actual control of the wind turbine is performed in real time using a Simulink model running on the dSPACE controller. For clarity, this model is divided into two parts. The first part, shown in Figure 5.6, handles sensor data acquisition, including torque and encoder signals. The second part, depicted in Figure 5.7, manages motor control via an H-bridge and processes hexapod positioning signals.

This Simulink model is then uploaded to the dSPACE system, where it can be accessed through the dSPACE control interface shown in Figure 5.8. This interface enables real-time monitoring of all variables and allows direct control of the motor by adjusting the duty cycle and rotation direction. Additionally, data logging is supported, with the option to export recordings as MATLAB files for detailed post-processing and analysis.

Separately, the hexapod was controlled using modified Quanser code provided by the DCSC lab. Detailed steps can be found in Appendix H.

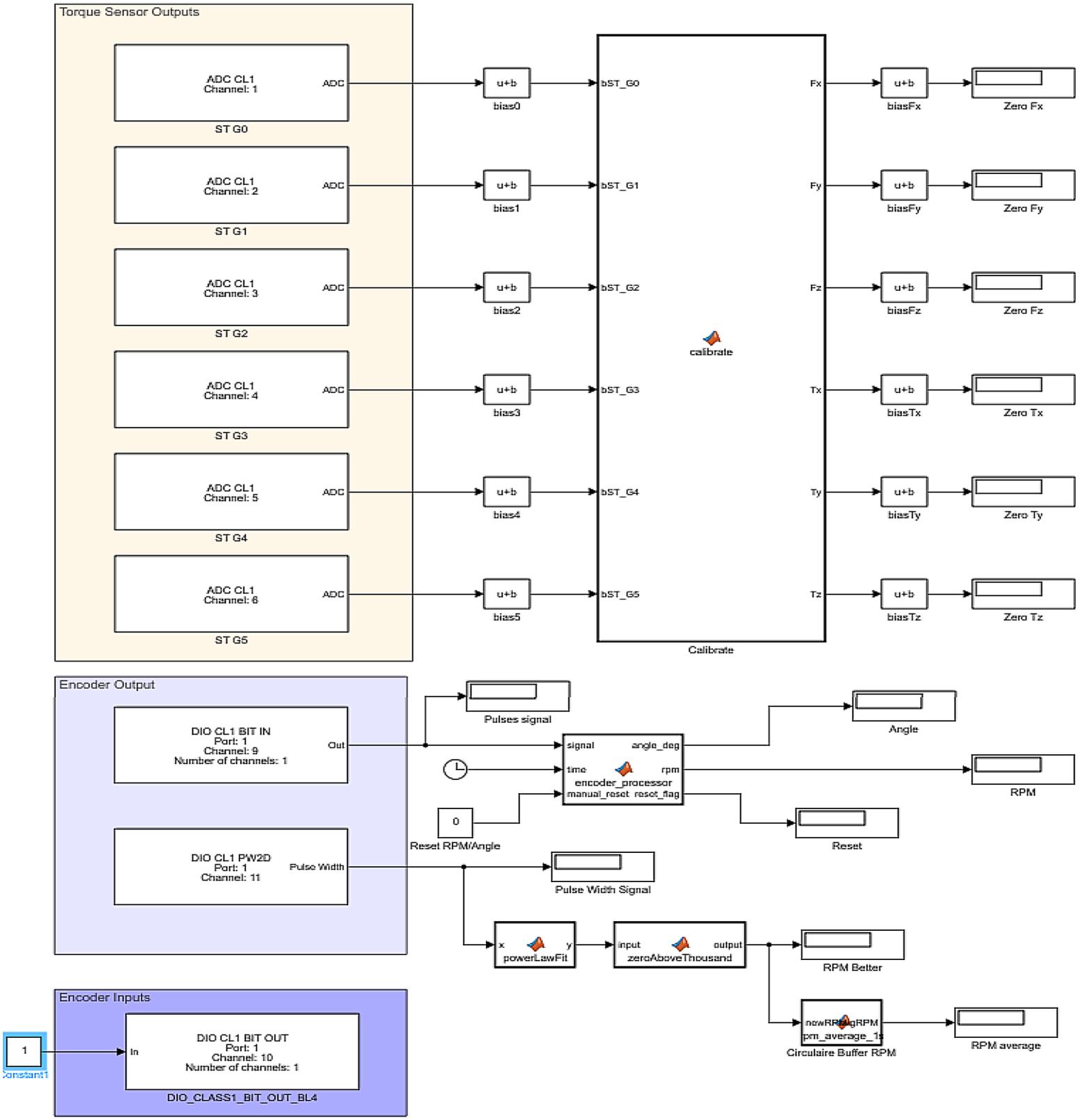

Figure 5.6: First half of the Simulink model on the dSPACE controller, color-coded by function: (1) yellow for torque sensor readout and conversion, (2) light purple for encoder signal readout (see Section 6.3.2), (3) dark purple for encoder input processing.

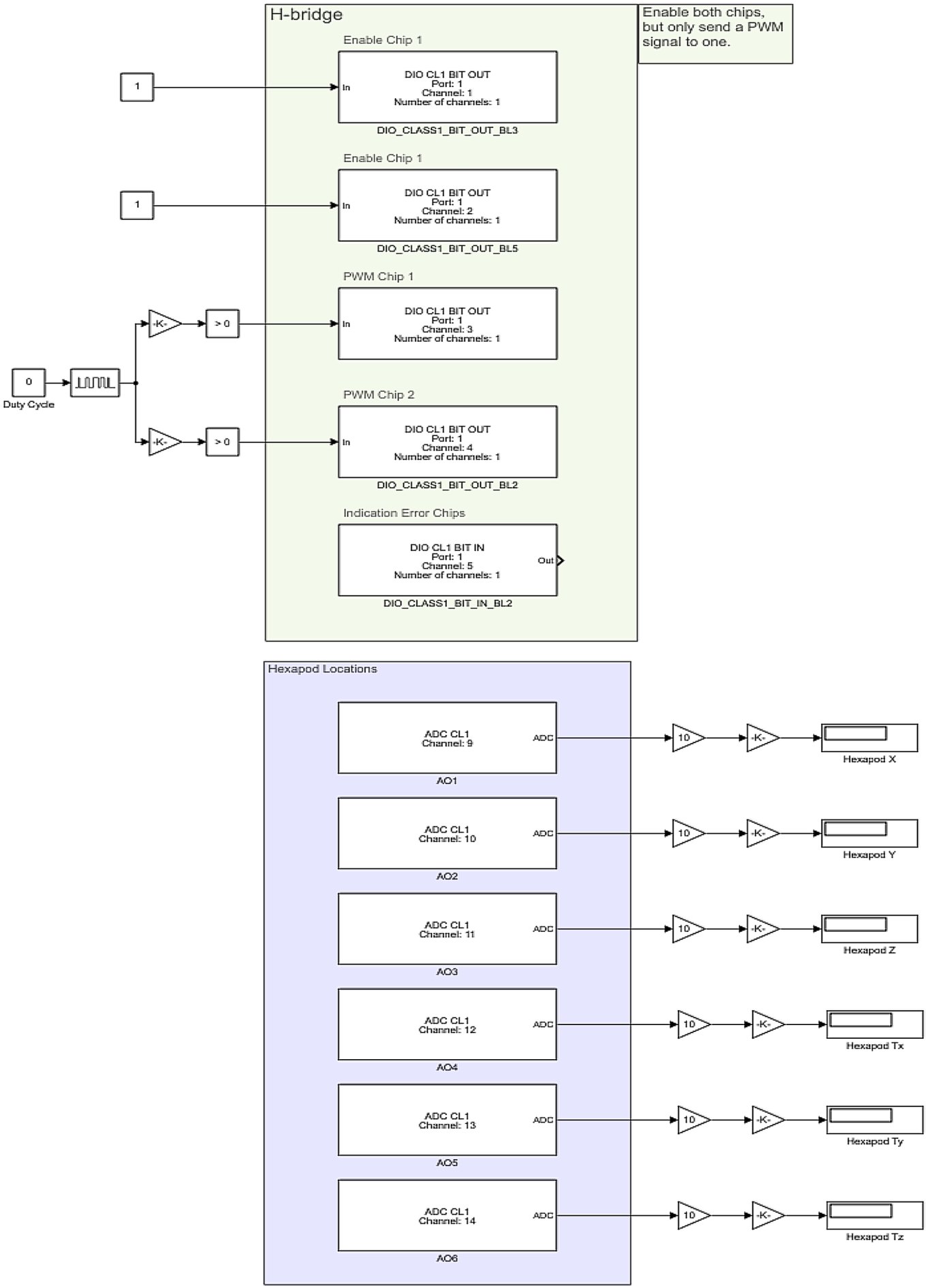

Figure 5.7: Second half of the Simulink model divided into two sections: (5) green for H-bridge control with 100 Hz duty cycle, and (6) purple for hexapod position readout from analog signal conversion.

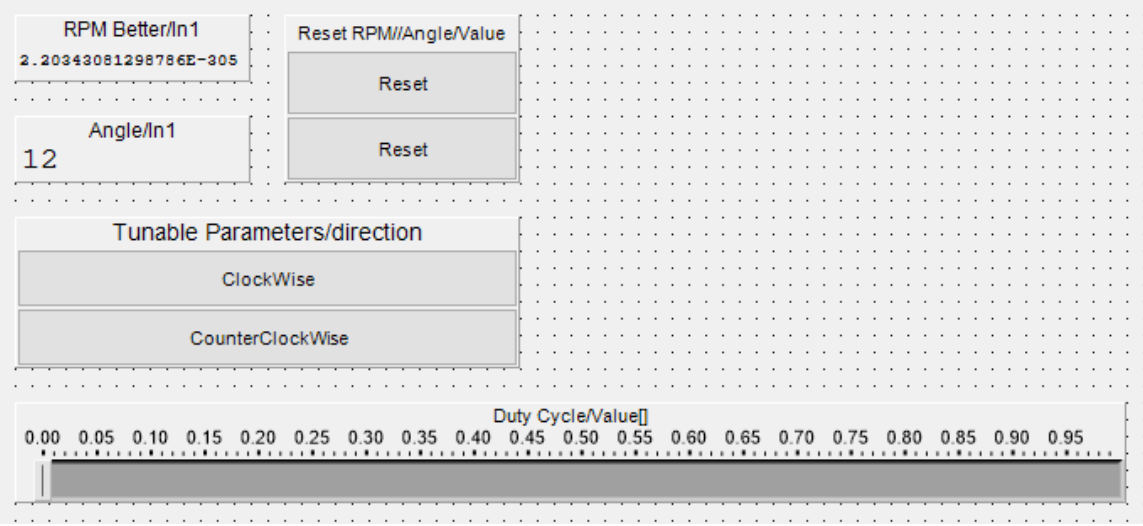

Figure 5.8: dSPACE control interface for real-time monitoring, motor control through duty cycle and rotation direction adjustments, and data logging with MATLAB export capability. Key features include RPM display, angle calculation with manual reset, and tunable motor parameters for changing the motor direction (theory detailed in Section 6.3.2).

5.4 Construction and Assembly

With the design finalized, this section walks through the construction steps, assembly process, and final tweaks made after practical testing.

5.4.1 Construction Manual of Turbine Design

The first step in the construction process was creating a clear manual to ensure reproducibility and simplify future testing or redesigns. The manual includes:

- Step-by-step build instructions with annotated diagrams to guide the assembly process.
- Tool and material lists to ensure all necessary components are available before starting.
- Tolerances and critical alignments to ensure precision in every aspect of the construction.
- Troubleshooting tips for common build issues, helping to resolve potential problems during assembly.

The process of documenting the build not only helped organize the steps clearly but also led to the identification of design improvements. These insights were integrated into subsequent versions of the design, although the latest version still shows slight differences to the final wind turbine. The documentation and design files are available in the 4TU.ResearchData repository.

5.4.2 Assembly Validation of Turbine Design

After receiving all components, the turbine was assembled according to this construction manual. The aim of this validation step was to ensure the system could be safely installed in the wind tunnel and operated at controlled speeds. The following aspects were checked under no-load conditions:

- Smooth and stable rotation at low speed, without excessive vibration.
- Speed control and braking using the H-bridge and motor: verifying whether the motor responds as expected to input signals and can decelerate the turbine.
- Safe mounting compatibility with the wind tunnel baseplate and geometry.

Although full aerodynamic loading could not be tested outside the wind tunnel, preliminary observations indicated that the system behaves predictably during manual or low-speed electric rotation.

5.4.3 Final Design Adjustments

After putting the assembly to the test, a few final tweaks were needed to fine-tune performance and boost reliability. These adjustments included:

- **Removal of braking system:** Limited access and wiring constraints inside the sealed wind tunnel led to the removal of the original mechanical braking system. This was not problematic because the motor's strong back-EMF provides sufficient resistive torque to safely decelerate and control the turbine during operation.
- **Added structural reinforcement:** The housing's anisotropic (uneven) stiffness led to unwanted oscillations around 300–500 RPM, which coincides with the rotation speeds used during turbine testing. To fix this, a laser-cut stiffening plate was added to the turbine base. This shifted the eigenfrequencies and cut down the resonance, making the system safer and more stable.

- **Extended blade radius:** Slight vibrations still occurred between 300 and 600 RPM, prompting an increase in blade diameter from 0.5 m to 1 meter. This adjustment allows the turbine to maintain the same tip-speed ratio at lower rotational speeds, ensuring operational readiness.

5.5 Conclusion

The goal of this section was to design and construct a single-blade vertical-axis wind turbine prototype through an iterative process involving CAD modeling, physical assembly, and control system implementation.

The design process successfully balanced practical constraints with performance objectives by continuously refining the turbine's geometry and structure. Developing a detailed construction manual proved invaluable, streamlining assembly and revealing key structural details early on. The implementation of electrical and control systems resulted in stable, responsive turbine operation, while validation testing provided important insights that guided the final adjustments.

These experiences offer clear direction for future design improvements and culminated in a functional, reliable prototype, illustrated from multiple perspectives in Figure 5.9, ready to support aerodynamic experiments.

Some limitations emerged during the project, including constraints imposed by the wind tunnel setup, such as the removal of the mechanical brake, and unexpected structural resonance that required modifications after construction.

Future work could focus on incorporating dynamic simulations from the early design stages to better anticipate and mitigate resonance issues related to eigenfrequencies. Additionally, exploring alternative control strategies aimed at maintaining a constant rotational speed could further enhance turbine performance.

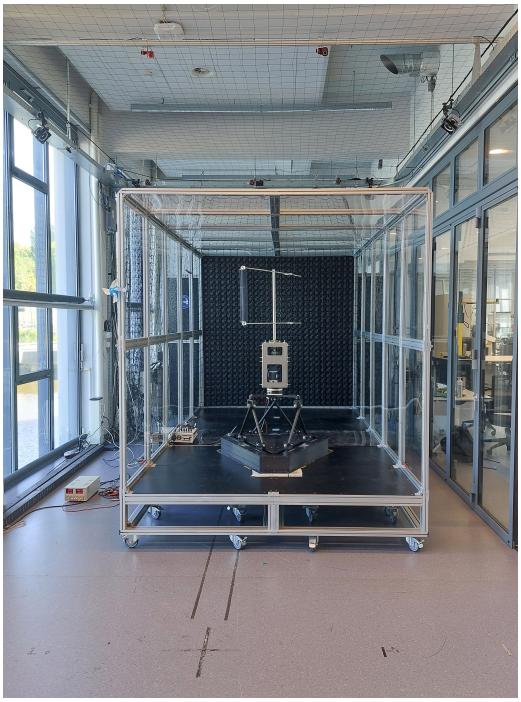

(a) Wind tunnel exterior

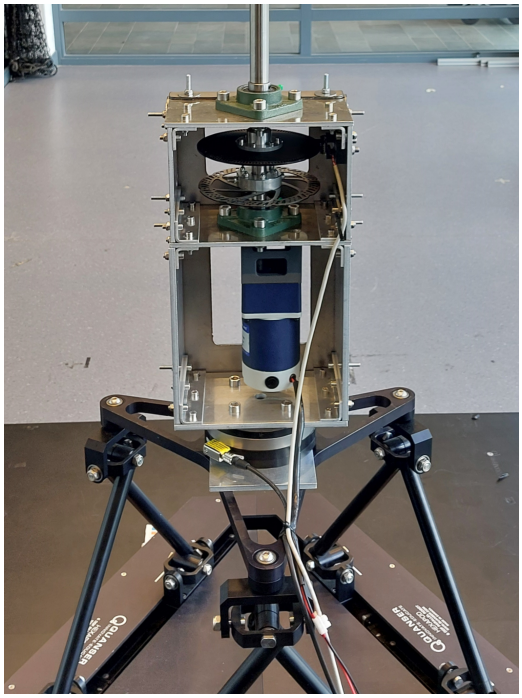

(b) Frontal view of turbine

(c) Electronics setup

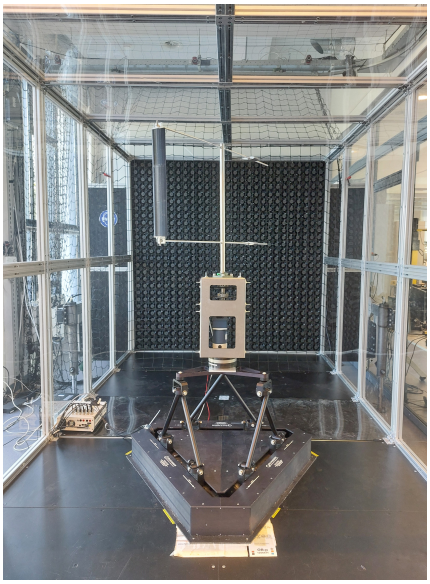

(d) Interior of wind tunnel

Figure 5.9: Final wind turbine prototype shown from various perspectives.

6. Sinusoidal Wind Experiments

Building upon the validated turbine assembly and wind facility setup, the following experimental approach was employed to investigate turbine performance under controlled wind conditions.

6.1 Objectives of the Experimental Campaign

The primary objective of this section is to investigate the aerodynamic performance of the turbine under sinusoidal inflow conditions, as tested in the wind tunnel at the DCSC Lab. The experiments focus on three main goals:

1. **Impact of inflow frequency on power efficiency:**
   To assess the influence of oscillation frequency on turbine performance, tests were conducted over a range of dimensionless frequencies (ω^*) from 0 to 0.189. The amplitude of the imposed translational motion was fixed at 0.5 m. For each frequency, torque was measured at multiple tip speed ratios (λ) to evaluate the resulting variations in aerodynamic loading and power efficiency.

2. **Effect of inflow amplitude on power efficiency:**
   The role of inflow amplitude was examined by varying the oscillation amplitude between 0.05 m and 0.45 m at a fixed dimensionless frequency of 0.126 and a constant tip speed ratio $\lambda = 2.0$. This allowed for isolation of amplitude effects while maintaining consistent operating conditions.

3. **Phase interaction between inflow and turbine rotation:**
   To investigate the interaction between the phase of the imposed inflow and the rotor azimuthal position, a two-dimensional torque map was constructed. Torque data were binned by blade azimuth and hexapod wave phase, revealing how timing between oscillatory inflow and blade rotation influences performance.

To achieve these objectives, the final experimental setup is presented in Figure 6.1, following the configuration described in section 5. The software setup and measurement procedures are provided in detail in Appendix I.

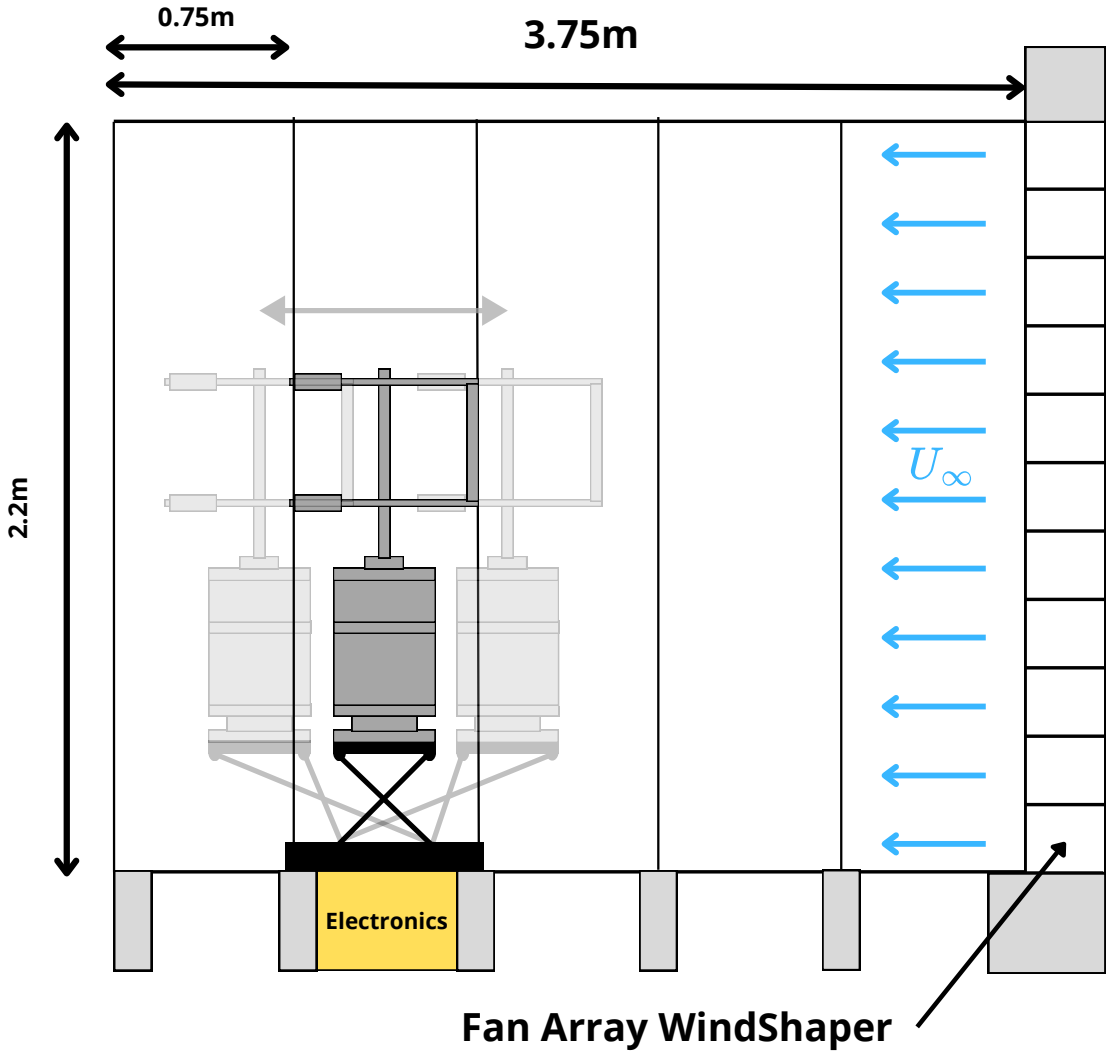

Figure 6.1: Overview of the experimental setup. The wind turbine is mounted near the center of the fourth wind tunnel segment from the right on a hexapod. This placement is closer to the WindShaper module than in previous studies due to practical system constraints. Electronic components, including the data acquisition system and power supplies, are positioned beneath the wind tunnel, outside the airflow domain. Wind tunnel segments are annotated with their respective lengths. Note: Flow direction is shown from right to left for experimental setup clarity.

6.2 Experimental Cases

Working with this experimental setup, the test program is divided into three distinct phases. In the first phase, initial tests are carried out without the blade, referred to as the zero case. In the second phase, the blade and counterweight are installed, and iterative adjustments are made to ensure dynamic stability (Table 6.1).

Once the turbine reaches stable rotation, the frequency variation study is conducted to examine how different inflow fluctuation frequencies influence turbine performance (Table 6.3). The selection of the frequency range is justified in Appendix J. In the third phase, an amplitude variation study is carried out at a fixed frequency and tip-speed ratio to isolate the effect of inflow amplitude on torque generation (Table 6.2). All tests involving the blade are repeated three times to ensure robustness and repeatability of the results. Each case consists of 18 hexapod cycles per run, and for the steady hexapod cases, each run lasts 60 seconds.

Table 6.1: Summary of balance optimization tests aimed at minimizing lateral (x) and vertical (y) torque components on the turbine shaft.

Test	**Condition**	**Goal**
y1	Spin turbine w/o wind	Measure initial x, y torques
y2	Adjust counterweights	Reduce x, y torques
y3	Spin turbine w/o wind	Verify torque reduction
y4	Repeat y2 and y3 as needed	Ensure stable minimal torques

Table 6.2: Test matrix showing a range of varying inflow amplitudes at a fixed dimensionless frequency $\omega^* = 0.126$, with constant angular frequency $\omega_{\text{rad}} = 2.513\,\text{rad/s}$. Each test runs for 18 cycles (44.84 seconds) to ensure sufficient data collection.

λ Group	**Case**	Ω **[rad/s]**	ω_{rad} **[rad/s]**	A **[m]**	$\boldsymbol{\omega^*}$ [-]	$\boldsymbol{A^*}$ [-]	**Time for 18 cycles [s]**
	J1	20.0	2.513	0.05	0.126	0.100	44.84
	J2	20.0	2.513	0.10	0.126	0.200	44.84
	J3	20.0	2.513	0.15	0.126	0.300	44.84
	J4	20.0	2.513	0.20	0.126	0.400	44.84
2.0	J5	20.0	2.513	0.25	0.126	0.500	44.84
	J6	20.0	2.513	0.30	0.126	0.600	44.84
	J7	20.0	2.513	0.35	0.126	0.700	44.84
	J8	20.0	2.513	0.40	0.126	0.800	44.84
	J9	20.0	2.513	0.45	0.126	0.900	44.84

Table 6.3: Test matrix showing varying dimensionless frequencies ω^* and corresponding physical parameters at fixed amplitude $A = 0.5\,\mathrm{m}$ across different tip speed ratio groups λ. The table lists rotational speeds Ω (rad/s), oscillation frequencies ω (rad/s), dimensionless amplitudes A^*, and test durations for 18 oscillation cycles. Zero-frequency cases correspond to steady inflow conditions for baseline comparison.

λ Group	**Case**	Ω **[rad/s]**	ω_{rad} **[rad/s]**	A **[m]**	$\boldsymbol{\omega^*}$ [-]	$\boldsymbol{A^*}$ [-]	**Time for 18 cycles [s]**
1.0	A1	10	0.000	0.0	0.000	0	0.00
	A2	10	0.314	0.5	0.0314	1	360.00
	A3	10	0.628	0.5	0.063	1	180.00
	A4	10	0.942	0.5	0.094	1	120.00
	A5	10	1.257	0.5	0.126	1	90.00
	A6	10	1.571	0.5	0.157	1	72.00
	A7	10	1.885	0.5	0.189	1	60.00
1.25	B1	12.5	0.000	0.0	0.000	0	0.00
	B2	12.5	1.571	0.5	0.126	1	72.00
1.5	C1	15	0.000	0.0	0.000	0	0.00
	C2	15	0.471	0.5	0.031	1	243.24
	C3	15	0.942	0.5	0.063	1	113.20
	C4	15	1.413	0.5	0.094	1	80.18
	C5	15	1.885	0.5	0.126	1	59.90
	C6	15	2.356	0.5	0.157	1	48.00
	C7	15	2.835	0.5	0.189	1	39.92
1.75	D1	17.5	0.000	0.0	0.000	0	0.00
	D2	17.5	2.199	0.5	0.126	1	51.43
2.0	E1	20.0	0.000	0.0	0.000	0	0.00
	E2	20.0	0.628	0.5	0.031	1	181.82
	E3	20.0	1.257	0.5	0.063	1	89.56
	E4	20.0	1.885	0.5	0.094	1	60.10
	E5	20.0	2.513	0.5	0.126	1	44.84
	E6	20.0	3.142	0.5	0.157	1	36.00
	E7	20.0	3.781	0.5	0.189	1	29.92
2.25	F1	22.5	0.000	0.0	0.000	0	0.00
	F2	22.5	2.828	0.5	0.126	1	40.00
2.5	G1	25	0.000	0.0	0.000	0	0.00
	G2	25	0.785	0.5	0.031	1	145.16
	G3	25	1.571	0.5	0.063	1	72.44
	G4	25	2.356	0.5	0.094	1	48.26
	G5	25	3.142	0.5	0.126	1	36.18
	G6	25	3.927	0.5	0.157	1	28.94
	G7	25	4.726	0.5	0.189	1	23.92
2.75	H1	27.5	0.000	0.0	0.000	0	0.00
	H2	27.5	3.456	0.5	0.126	1	32.73
3.0	I1	30	0.000	0.0	0.000	0	0.00
	I2	30	0.942	0.5	0.031	1	120.80
	I3	30	1.885	0.5	0.063	1	60.30
	I4	30	2.828	0.5	0.094	1	40.22
	I5	30	3.770	0.5	0.126	1	30.14
	I6	30	4.712	0.5	0.157	1	24.10
	I7	30	5.671	0.5	0.189	1	19.94

6.3 Data Analysis Approach

This section discusses the method used to process raw experimental signals and derive the turbine performance metrics for the experimental cases. The code used for the calculations presented in this work is available in the 4TU.ResearchData repository.

6.3.1 Raw Signals Overview

To characterize the turbine's response under sinusoidal inflow conditions, three key signals were measured simultaneously. These signals form the basis for deriving aerodynamic performance metrics:

- **Torque sensor (Tz direction):** Figure 6.2 shows the torque measured in the Tz direction over the first 3 seconds for both the baseline (no wind) and experimental run (with wind). The torque signal appears as a band ranging roughly from 1.2 to 1.55 Nm. This apparent variation is caused by high-frequency spikes superimposed on an otherwise relatively constant torque baseline.

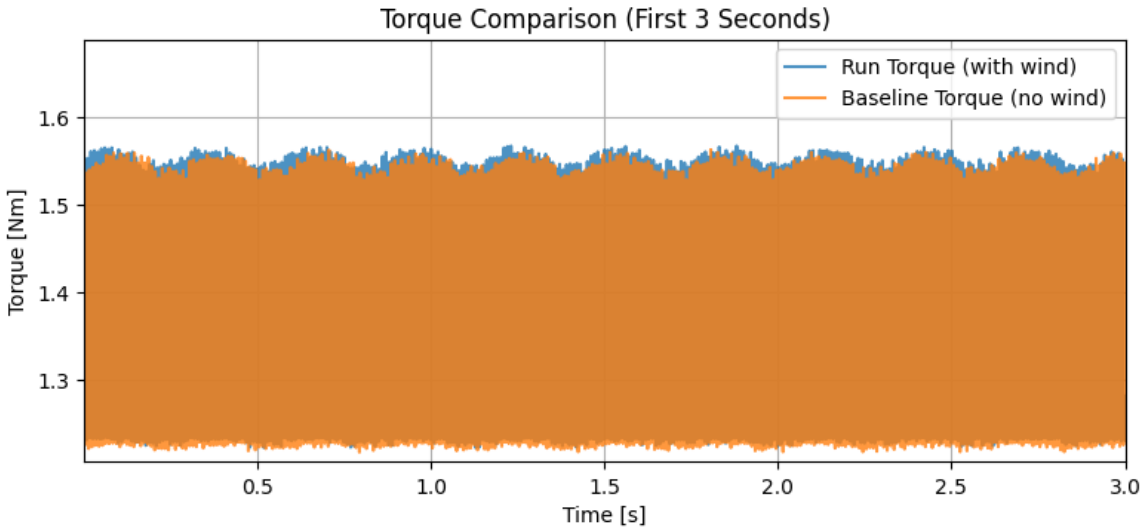

Figure 6.2: Torque signal measured in the Tz direction during the first 3 seconds of the sinusoidal experiment for Case A1 ($\lambda = 1$, $w^* = 0$, $\Omega = 10$ rad/s). The shaded band between 1.2 and 1.55 Nm reflects the presence of high-frequency spikes superimposed on the baseline torque.

- **Encoder signal:** The encoder signal (left plot in Figure 6.3) is a digital representation of the rotor's angular position. It is high (1) when light passes through holes on a rotating disk and low (0) otherwise. The disk contains evenly spaced holes, with one larger or uniquely placed hole marking the start of each full rotation. This allows the encoder signal to serve both as a speed reference and as a phase marker.

- **Pulse width signal:** The pulse width signal (right plot in Figure 6.3) records the duration of the encoder's high-state as the rotor passes each hole. Sampled at a higher frequency than the encoder signal itself, it provides more precise timing information, enabling reconstruction of angular velocity profiles and evaluation of rotor speed variations and periodicity.

The objective of this signal analysis is to extract the turbine's aerodynamic performance under unsteady inflow conditions. The final outcome is the power coefficient curve (C_p) as a function of the tip speed ratio (λ), shown in Figure 6.4. This curve characterizes the turbine's efficiency across operating conditions.

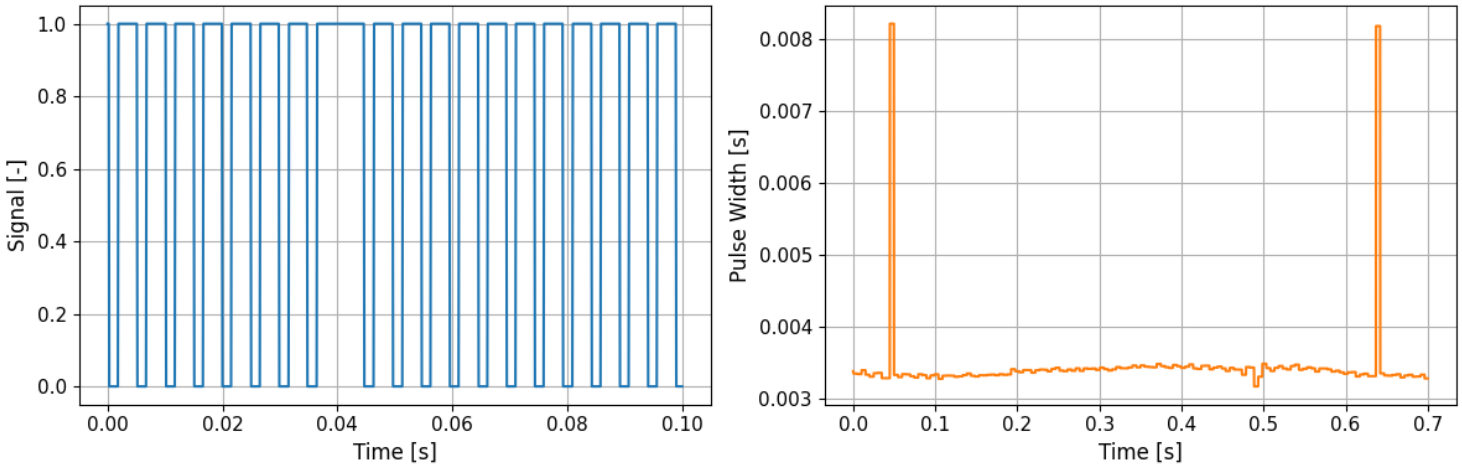

Figure 6.3: Encoder signal (left) over 0.2 seconds and pulse width signal (right) over 0.7 seconds for Case A1 ($\lambda = 1$, $w^* = 0$, $\Omega = 10$ rad/s), providing information on rotor position and rotational speed.

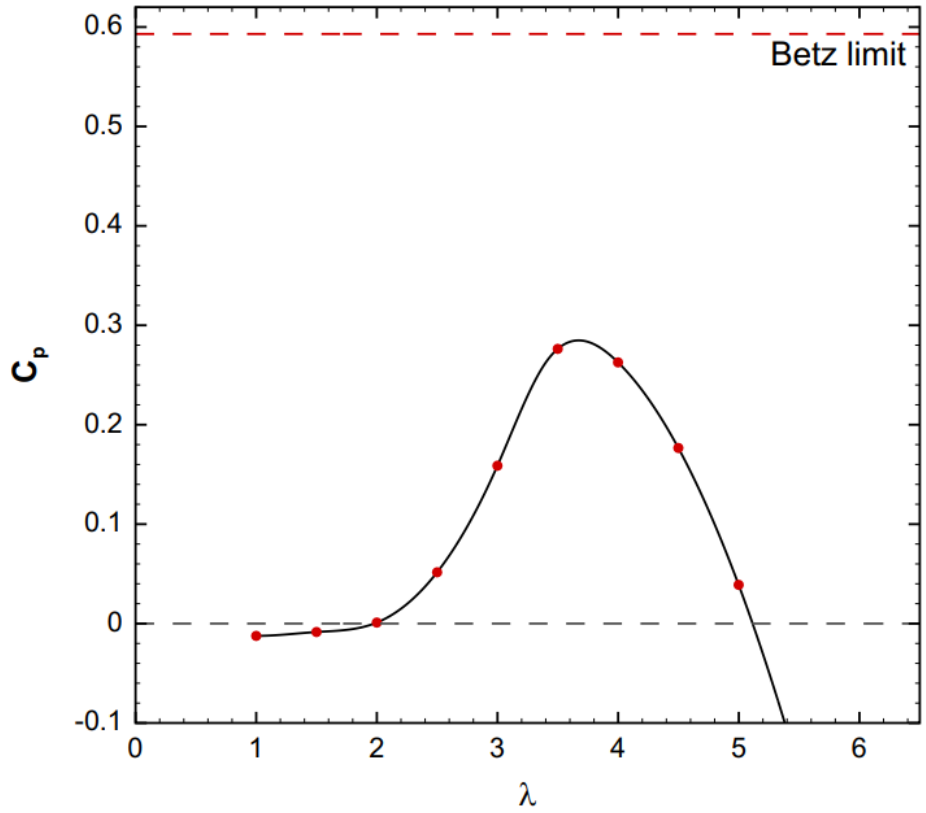

Figure 6.4: Example power coefficient (C_p) curve as a function of tip speed ratio (λ), based on URANS simulations of a two-blade H-rotor vertical-axis wind turbine at Reynolds number $Re_c = 70{,}000$ [51].

6.3.2 Determining Turbine Rotational Speed

From the raw encoder signal recorded over time during a gradual increase in motor duty cycle—producing a broad range of revolutions per minute (RPM) —the turbine's rotational speed was determined. The encoder disk has 120 evenly spaced holes, so each encoder pulse corresponds to a 3° rotation of the shaft. One slot is intentionally larger and reserved for a separate optical marker.

By measuring the time intervals between successive rising and falling edges of the signal (as illustrated in the left plot of Figure 6.3), the instantaneous RPM was calculated. A histogram of the resulting RPM distribution is shown in Figure 6.5, highlighting the noise in the raw encoder-based measurements. This variability is primarily due to the limited time resolution of the sampling system, as illustrated schematically in Figure 6.6.

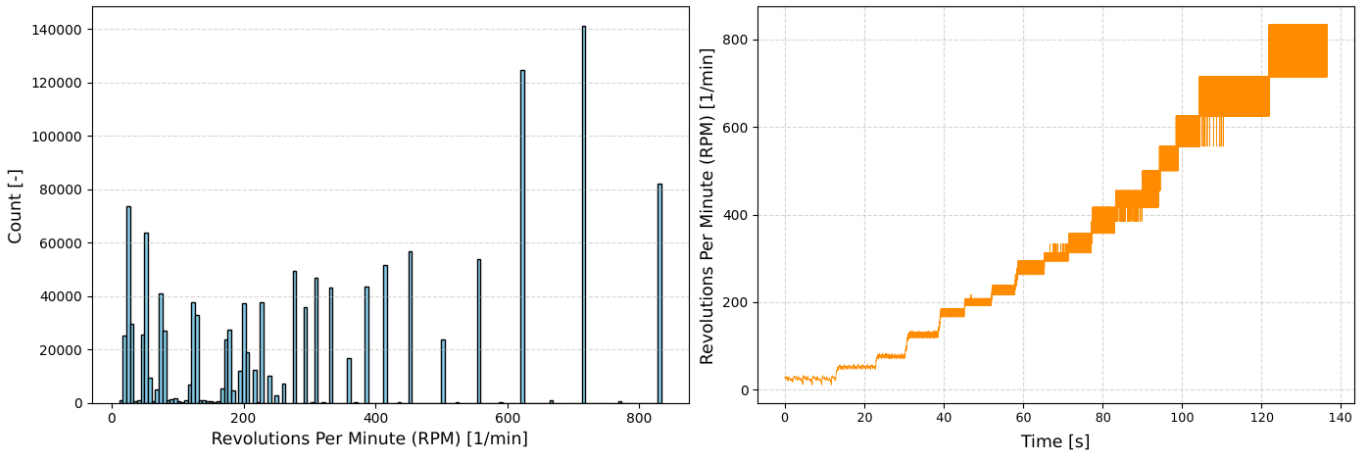

Figure 6.5: Left: Histogram of raw RPM values from encoder data, showing finer resolution at low RPMs and increasing quantization at high RPMs due to limited sampling rate. Right: Time series of the data, highlighting non-uniformity and resolution loss at higher speeds.

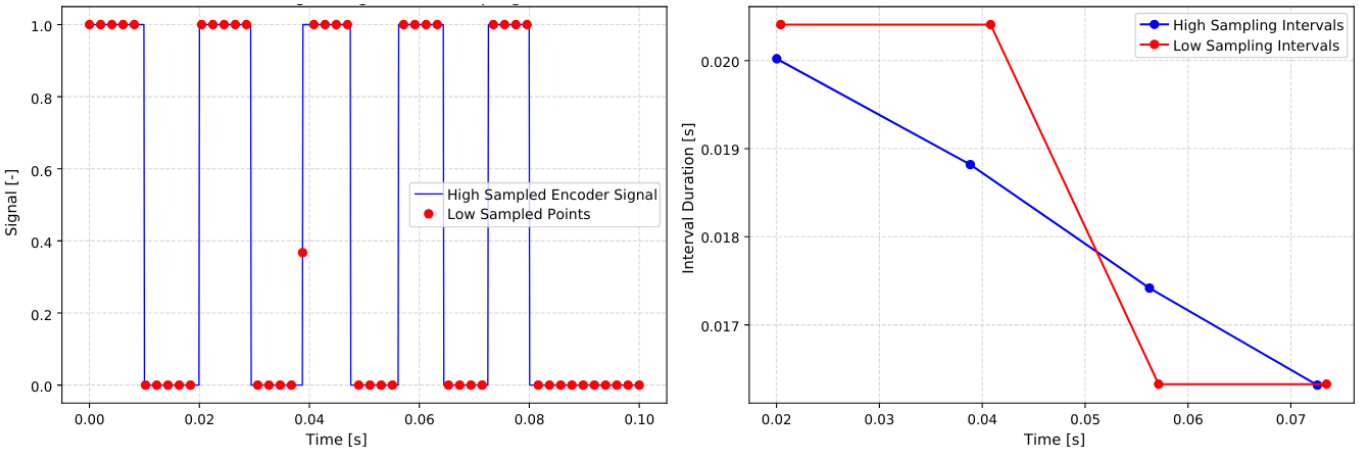

Figure 6.6: Effect of sampling resolution on encoder measurements. Left: Raw encoder signal sampled at high resolution (blue) and low resolution (red). The low-resolution signal misses some transitions, causing non-uniform detection of the encoder slots. Right: Time intervals between successive encoder pulses. High-resolution sampling (blue) accurately captures pulse timing, while low-resolution sampling (red) shows quantized intervals and reduced accuracy. These differences illustrate why low sampling rates increase uncertainty in RPM measurements.

To address these limitations, a more precise pulse width signal was used to reconstruct the RPM. As previously discussed, the pulse width corresponds to the exact time required for an optical hole to pass the sensor (see the right plot of Figure 6.3). By binning the encoder-based RPM values and averaging the corresponding pulse widths within each bin (in chunks of 10,000 points), a robust relationship between

RPM and pulse width was obtained. This relationship follows a power law, shown in Figure 6.7. The residuals from the power law fit were used to estimate the standard error of the mean (SEM) , which was combined with the sampling-related SEM to quantify the overall uncertainty in the reconstructed RPM.

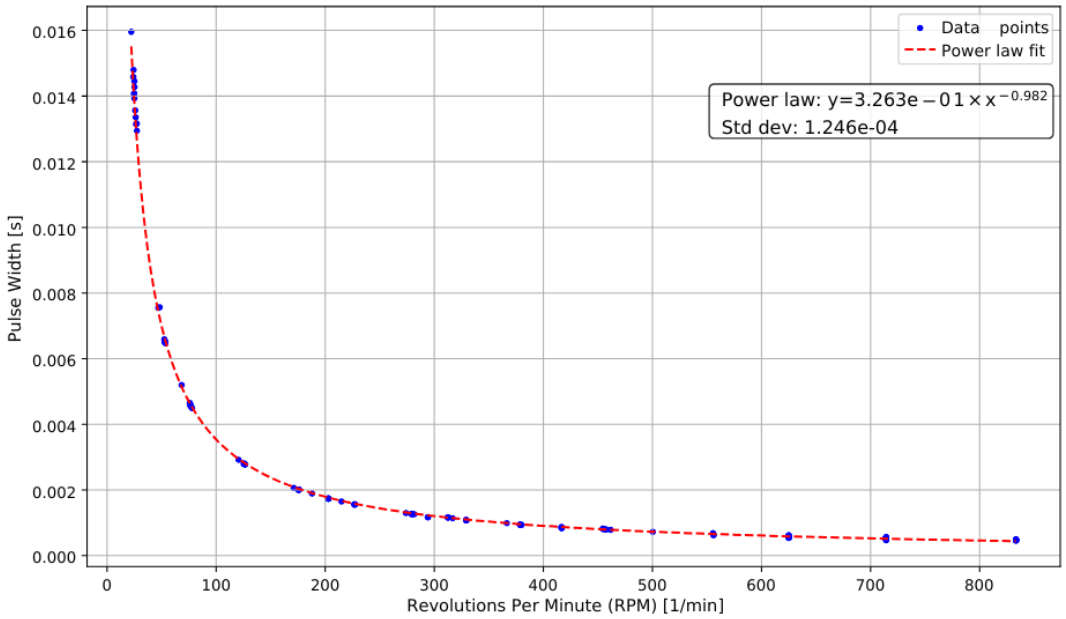

Figure 6.7: Power law fit between RPM and pulse width obtained from averaged bin data. This relation is used to reconstruct a smooth RPM signal from the pulse width signal, with uncertainty quantified as the standard error of the mean (SEM).

The resulting power law fit enables the estimation of instantaneous RPM directly from the pulse width signal, yielding a smoother and more accurate RPM profile over time—excluding the data points corresponding to the larger optical hole.

6.3.3 Computing the Tip Speed Ratio

Using this RPM data, the Tip Speed Ratio (λ) can be calculated; however, an accurate and reliable estimate of the turbine's rotational speed is essential to ensure the validity of further analysis. For each operating condition, RPM was measured with the blade attached (three runs) and once without the blade (zero case). These were denoted as `mean_rpms` and `mean_rpms_zero`, respectively, with associated standard errors of the mean (SEM) `sem_rpms` and `sem_rpms_zero`.
First, the mean RPM from both runs was averaged to obtain a central estimate:

$$\overline{\mathrm{RPM}} = \frac{\mathrm{RPM}_{\mathrm{forward}} + \mathrm{RPM}_{\mathrm{zero}}}{2} \tag{36}$$

To accurately capture uncertainty, both the SEM of each measurement and the potential bias between the two runs were considered. The combined uncertainty was computed by combining the individual SEM values and the absolute bias between the two means in quadrature:

$$\sigma_{\mathrm{SEM}} = \frac{\sqrt{\sigma^2_{\mathrm{forward}} + \sigma^2_{\mathrm{zero}}}}{2}, \quad \sigma_{\mathrm{bias}} = \frac{|\mathrm{RPM}_{\mathrm{forward}} - \mathrm{RPM}_{\mathrm{zero}}|}{2} \tag{37}$$

$$\sigma_{\mathrm{RPM,\ combined}} = \sqrt{\sigma^2_{\mathrm{SEM}} + \sigma^2_{\mathrm{bias}}} \tag{38}$$

As shown in Figure 6.8, the RPM measurements from both forward and zero-direction runs are combined to account for statistical variability and systematic offsets. The resulting RPM change is on the order of 1–2%, indicating good measurement consistency, largely due to the motor dominating the rotation.

Next, the rotational speed in RPM was converted to angular velocity ω in radians per second:

$$\Omega = \frac{2\pi \cdot \overline{\mathrm{RPM}}}{60}, \quad \sigma_\Omega = \frac{2\pi \cdot \sigma_{\mathrm{RPM,\ combined}}}{60} \tag{39}$$

With the turbine radius $R = 0.5\,\mathrm{m}$ and the inflow wind speed $U = 4.83\,\mathrm{m/s}$ (with SEM $\sigma_U = 0.21\,\mathrm{m/s}$ from goal 1, Section 4), the λ was calculated using the standard formula (Equation 3):

$$\lambda = \frac{\Omega R}{U}$$

To propagate the uncertainty into the λ estimate, the standard error propagation formula was applied:

$$\sigma_\lambda = \lambda \cdot \sqrt{\left(\frac{\sigma_\Omega}{\Omega}\right)^2 + \left(\frac{\sigma_U}{U}\right)^2} \tag{40}$$

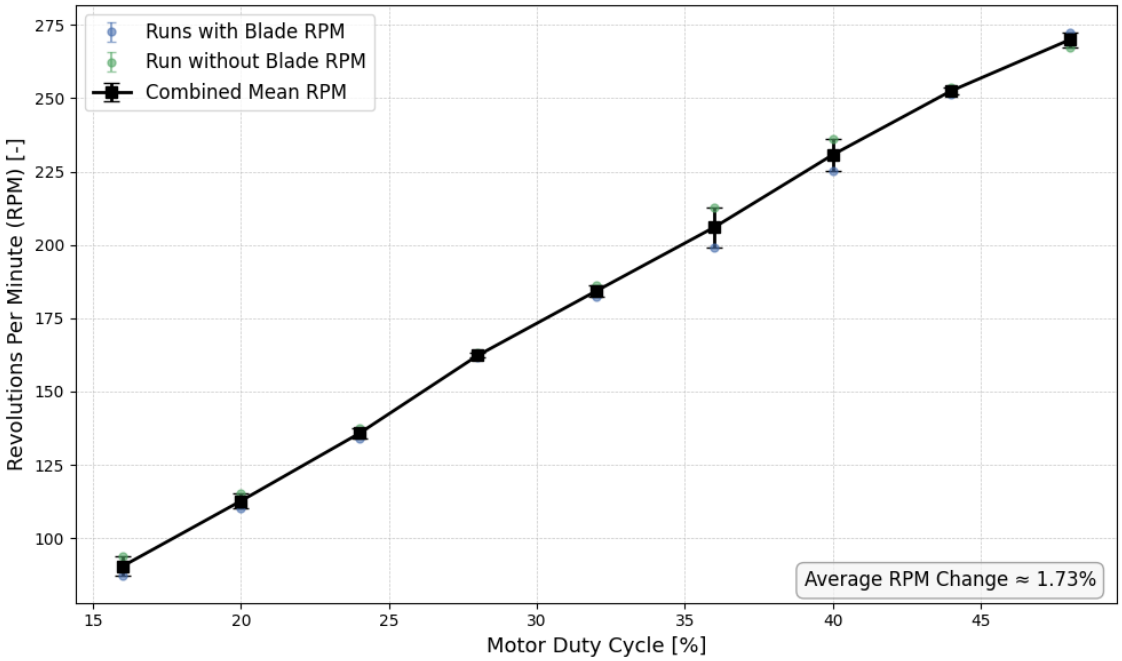

Figure 6.8: Mean RPM values during blade and no-blade runs with standard errors over motor duty cycle. Combined mean and total uncertainty (including systematic bias) are shown as black squares. The small RPM difference (1–2%) confirms the consistency of the measurement method.

6.3.4 Torque Calculation

Torque values were derived from sensor measurements collected across multiple experiments, providing robust data to analyze the turbine's mechanical performance. Each dataset, stored in HDF5 format, was processed to extract and aggregate the torque signals using two distinct methods:

Method 1: Direct Time-Averaged Torque In this method, torque values were averaged directly over time using the complete set of filtered measurements across multiple revolutions. Since the rotational speed of the rotor is effectively controlled by the motor, each azimuthal position is sampled with approximately equal weight. This provides a representative estimate of the mean aerodynamic torque experienced over time.

The standard error of the mean (SEM) was calculated from all filtered torque samples as:

$$\text{SEM} = \frac{\sigma_{\text{all}}}{\sqrt{N_{\text{all}}}} \tag{41}$$

where σ_{all} is the standard deviation and N_{all} is the number of filtered torque samples.

Method 2: Blade Phase-Binned Torque To gain more insight into how torque varies with blade position, a second approach was used in which torque values were grouped into bins based on the rotor's angular position (blade phase). The rotor angle was reconstructed from the encoder signal, using a digital counter that resets at the missing-tooth position. This mapping is illustrated in Figure 6.9, which shows how torque measurements are aligned with blade phase angles across revolutions.

Once the phase is reconstructed, the torque values are aggregated into bins (15 bins of 24° each) over a full 360° cycle. A separate no-wind run is used to establish a baseline torque profile, which is subtracted from the wind-on data in a bin-wise manner to isolate the aerodynamic contribution. Finally, torque values are averaged within each bin, resulting in a phase-resolved aerodynamic torque profile. For a flowchart of this method, see Appendix K.

As shown in Figure 6.10, this phase-binning groups torque values according to the blade's position during rotation. This binning approach is also used in the heatmap visualizations later in the thesis. By comparing the binned torque profiles to those computed using the direct (time-based) averaging method, it becomes possible to validate whether the phase-resolved torques follow a similar trend, thereby increasing confidence in the results. Indeed, the shape of the binned torque profile is qualitatively similar to the expected torque curve from Figure 2.9, which further supports that the analysis has been performed correctly. If the patterns from both approaches are consistent, it suggests that the binning process does not introduce bias and that the averaged torque values are representative of the true loading behavior.

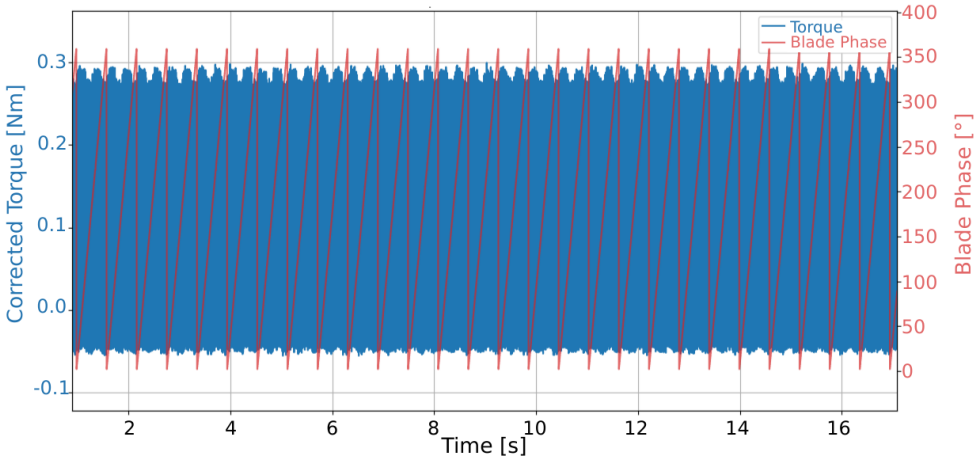

Figure 6.9: Example of torque measurements mapped to blade phase angles (θ), using encoder resets at the missing-tooth position to align data across revolutions. This enables phase-based torque binning over the rotor cycle.

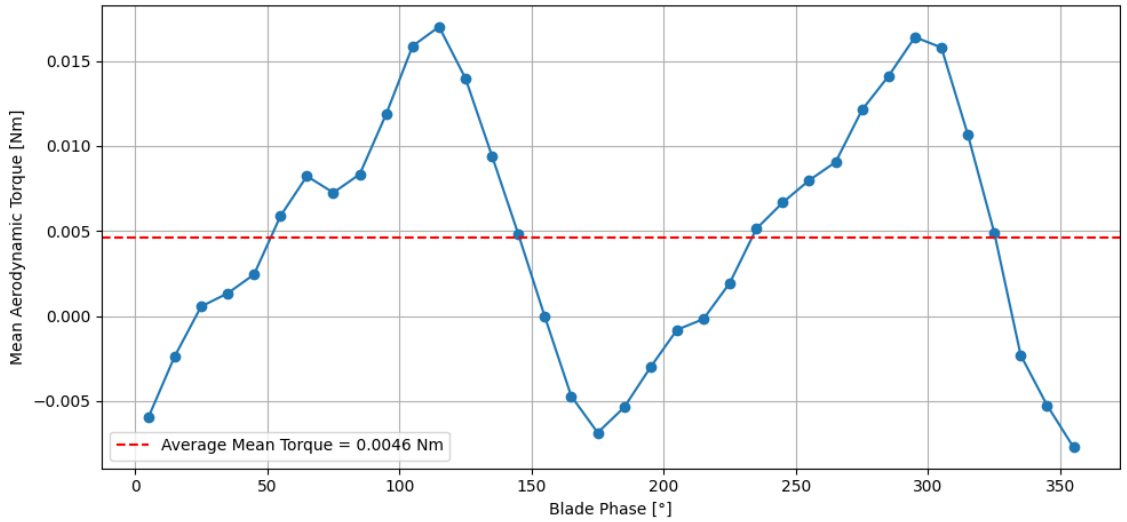

Figure 6.10: Example of Aerodynamic torque vs. blade phase angle (θ), binned into 36 intervals over one rotor revolution. Zero-wind runs were subtracted to isolate aerodynamic effects. Dashed line indicates the mean torque. Data shown at tip-speed ratio (λ) 1 and non-dimensional wind speed $w^* = 0.126$.

This approach reveals not only the mean torque but also how it fluctuates over the rotor cycle, providing insight into asymmetric loading effects under unsteady inflow. These variations are particularly useful for interpreting the more complex sinusoidal inflow results shown later in the thesis.

6.3.5 Dimensionless Torque Computation

To compare these torque results across different flow conditions and turbine setups, the mean torque was non-dimensionalized using the torque coefficient, C_T, defined as:

$$C_T = \frac{T}{\frac{1}{2}\rho A R U^2} \tag{42}$$

where T is the mean torque (after filtering and averaging), $\rho = 1.225\,\mathrm{kg/m^3}$ is the air density, A is the turbine's swept area, R the radius, and U the mean wind speed. In this setup, $A = 0.45 \times 0.5\,\mathrm{m^2}$ for the single-bladed H-type configuration, and $U = 4.83\,\mathrm{m/s}$.

To isolate the aerodynamic effect, torque values from blade-on runs were compared to the zero case (without blades) at each tip-speed ratio (λ):

$$\Delta T = T_{\text{blade}} - T_{\text{zero}} \qquad \Rightarrow \qquad \Delta C_T = \frac{\Delta T}{\frac{1}{2}\rho A R U^2} \tag{43}$$

The standard error of the torque difference was propagated from both blade and zero-case measurements:

$$\mathrm{SEM}_{\Delta T} = \sqrt{\left(\frac{\sigma_{\mathrm{blade}}}{\sqrt{N_{\mathrm{blade}}}}\right)^2 + \left(\frac{\sigma_{\mathrm{zero}}}{\sqrt{N_{\mathrm{zero}}}}\right)^2} \tag{44}$$

The corresponding uncertainty in ΔC_T includes wind speed uncertainty:

$$\mathrm{SEM}_{\Delta C_T} = \Delta C_T \cdot \sqrt{\left(\frac{\mathrm{SEM}_{\Delta T}}{\Delta T}\right)^2 + \left(\frac{2 \cdot \mathrm{SEM}_U}{U}\right)^2} \tag{45}$$

where $\mathrm{SEM}_U = \sigma_U / \sqrt{N_U}$ is the standard error in wind speed. In this study, $\sigma_U = 0.21\,\mathrm{m/s}$ and $N_U = 80{,}422$ (from section 4). Figure 6.11 shows the resulting ΔC_T at $\lambda = 1$ for the stationary hexapod case.

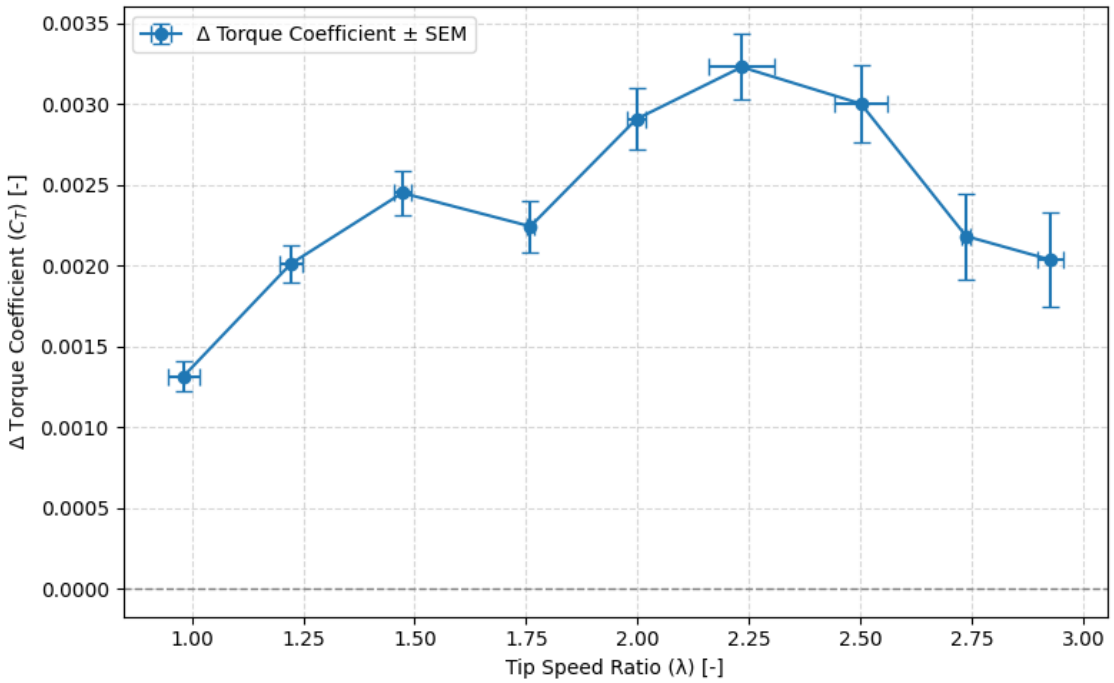

Figure 6.11: Dimensionless torque coefficient difference, ΔC_T, as a function of tip-speed ratio (λ) for the stationary hexapod configuration ($w^* = 0$). Vertical error bars represent propagated standard errors combining torque and wind speed uncertainties; horizontal error bars indicate uncertainty in λ.

6.3.6 Calculating the Power Coefficient

This dimensionless torque leads to the power coefficient, C_p, which measures the efficiency of converting wind power into mechanical power and is calculated as:

$$C_p = \frac{P_{\text{mech}}}{P_{\text{wind}}} = \frac{T \cdot \omega}{\frac{1}{2}\rho A U^3} \tag{46}$$

where T is the mean torque, ω the angular velocity, ρ the air density, A the turbine swept area, and U the mean wind speed.

The combined uncertainty in C_p accounts for errors in torque, rotational speed, and wind speed measurements:

$$\text{SEM}_{C_p} = C_p \cdot \sqrt{\left(\frac{\text{SEM}_T}{T}\right)^2 + \left(\frac{\text{SEM}_\omega}{\omega}\right)^2 + \left(3 \cdot \frac{\text{SEM}_U}{U}\right)^2} \tag{47}$$

where SEM_T, SEM_ω, and SEM_U are the standard errors of torque, angular velocity, and wind speed respectively. The factor 3 arises from the cubic dependence of power on wind speed. Figure 6.12 shows the resulting C_p as a function of tip speed ratio (λ), including propagated uncertainties.

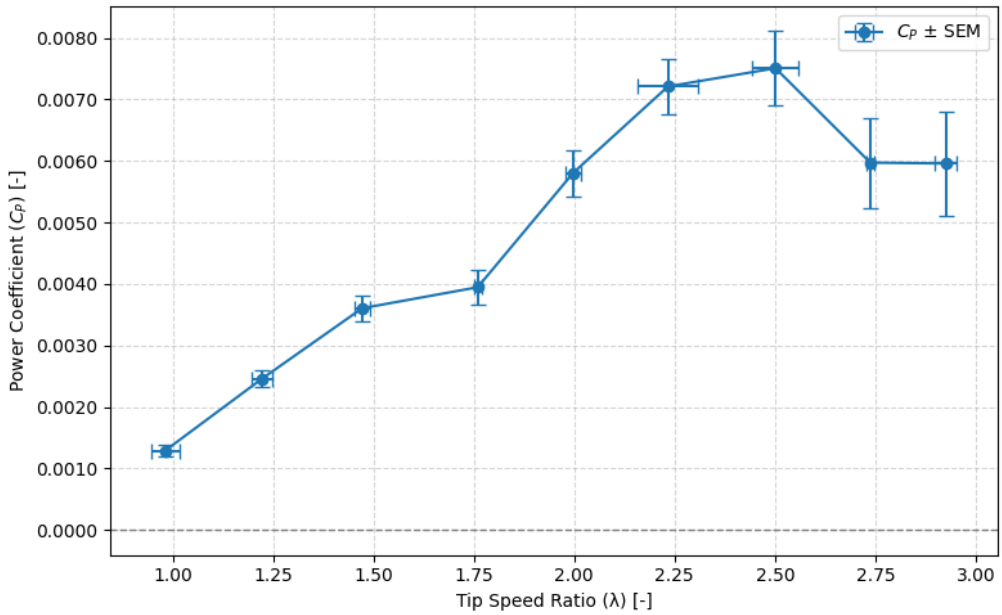

Figure 6.12: Power coefficient C_p versus tip speed ratio (λ) for the stationary hexapod configuration ($w^* = 0$). Error bars represent propagated uncertainties from torque, rotational speed, and wind speed measurements.

Under steady inflow, the power coefficient curve $C_p(\lambda)$ shows a typical bell shape with a clear optimum at a specific tip-speed ratio, consistent with prior experimental and numerical VAWT studies [57]. This peak marks the operating point where aerodynamic torques are most efficiently converted into mechanical power, minimizing flow separation and dynamic stall.

Although the expected trend is evident, the measured $C_p \approx 0.008$ is about 30 times lower than typical values [57], likely due to torque underestimation from sensor miscalibration, drivetrain losses, or dissipation before measurement. As the study focuses on relative performance trends, this offset does not undermine the validity of the conclusions.

6.3.7 Heat Map Generation

At last, to analyze how aerodynamic torque varies with blade position and hexapod motion, 2D heat maps are generated by binning phase data. A zero-wind reference is used to capture baseline torque from friction and mechanical effects, which is subtracted from the windy-condition data to isolate the aerodynamic contribution. The process consists of the following steps:

- The blade phase is reconstructed from an encoder signal using a custom pulse-based algorithm. The azimuthal angle increments by a fixed number of degrees per pulse. A larger gap in the pulse train—created by an intentionally oversized hole in the encoder disk, serves as a reference marker (home position) for resetting the phase. This method is described in detail in Section 6.3.4.

- Because of the physical mounting, the encoder's reference position does not coincide with the blade's actual zero azimuthal angle. Therefore, an angular offset of 130° is applied to align the measured phase with the blade's true physical position, where zero degrees corresponds to the blade facing directly into the oncoming wind (see Appendix L for a figure).

- The hexapod position signal naturally oscillates between positive and negative values (e.g., +0.5 m to –0.5 m). By applying the Hilbert transform [58], this oscillatory signal is converted into an analytic signal, from which a continuous phase angle is computed. This phase angle smoothly varies from 0° to 360° over each oscillation cycle, providing a convenient representation of the hexapod's phase.

- Blade and hexapod phases are discretized into 2D bins (15×15) to construct the aerodynamic torque heatmaps (see Figure 6.13). Using the zero-wind reference data, a baseline torque map is computed by averaging torque values per bin. For each windy run, torque is binned in the same way, and the baseline is subtracted bin-wise to isolate the aerodynamic component. These aerodynamic torque maps are then accumulated and averaged across all runs to obtain the final mean aerodynamic torque heatmap.

This process produces a 2D heatmap with blade phase on the horizontal axis and hexapod phase on the vertical. It visualizes how aerodynamic torque varies over the blade's rotation and the hexapod's oscillation.

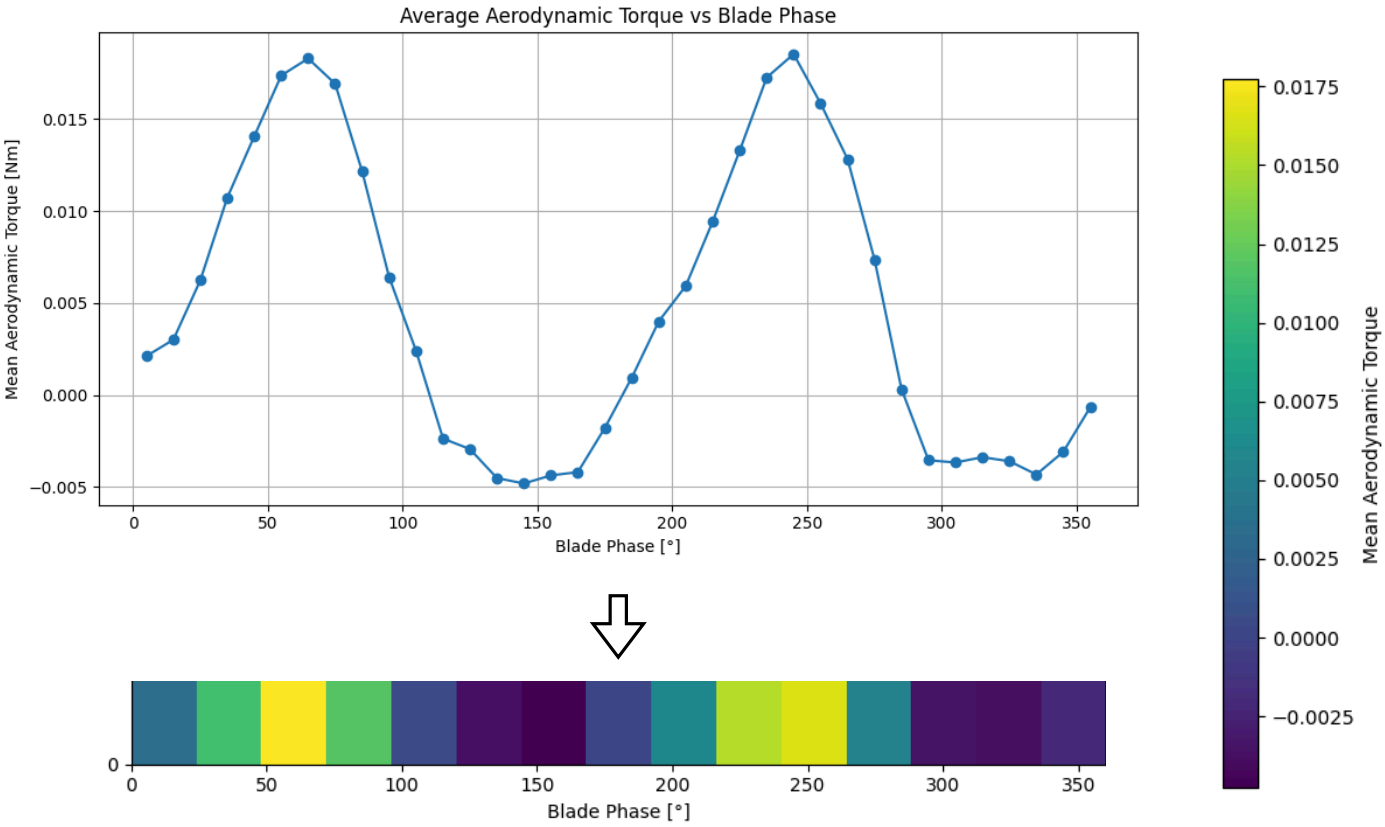

Figure 6.13: Example of computation of mean aerodynamic torque heatmaps: torque is binned by blade phase (as shown), and afterwards repeated for each hexapod phase. This binning procedure is then applied to generate the aerodynamic torque heatmaps shown in Figure 6.17 and Figure 6.18, highlighting spatial variations across blade and hexapod phases.

6.4 Findings

After establishing the methodology, this section focuses on presenting the experimental outcomes for the single-blade VAWT over varying tip-speed ratios (λ) and inflow oscillations. The analysis focuses on torque behavior, dimensionless scaling with ω^* and A^*, phase-resolved effects, and identification of optimal operating regimes under unsteady inflow conditions.

6.4.1 Influence of Oscillatory Inflow on Power Coefficient

Firstly, the power coefficient C_p was assessed over oscillation frequencies from 0 to 0.189 Hz at a fixed amplitude of 0.5 m/s for each λ group. To evaluate averaging effects, C_p was computed using two methods: a direct time average (Figure 6.14) and the phase-binned torque approach (Figure 6.15).

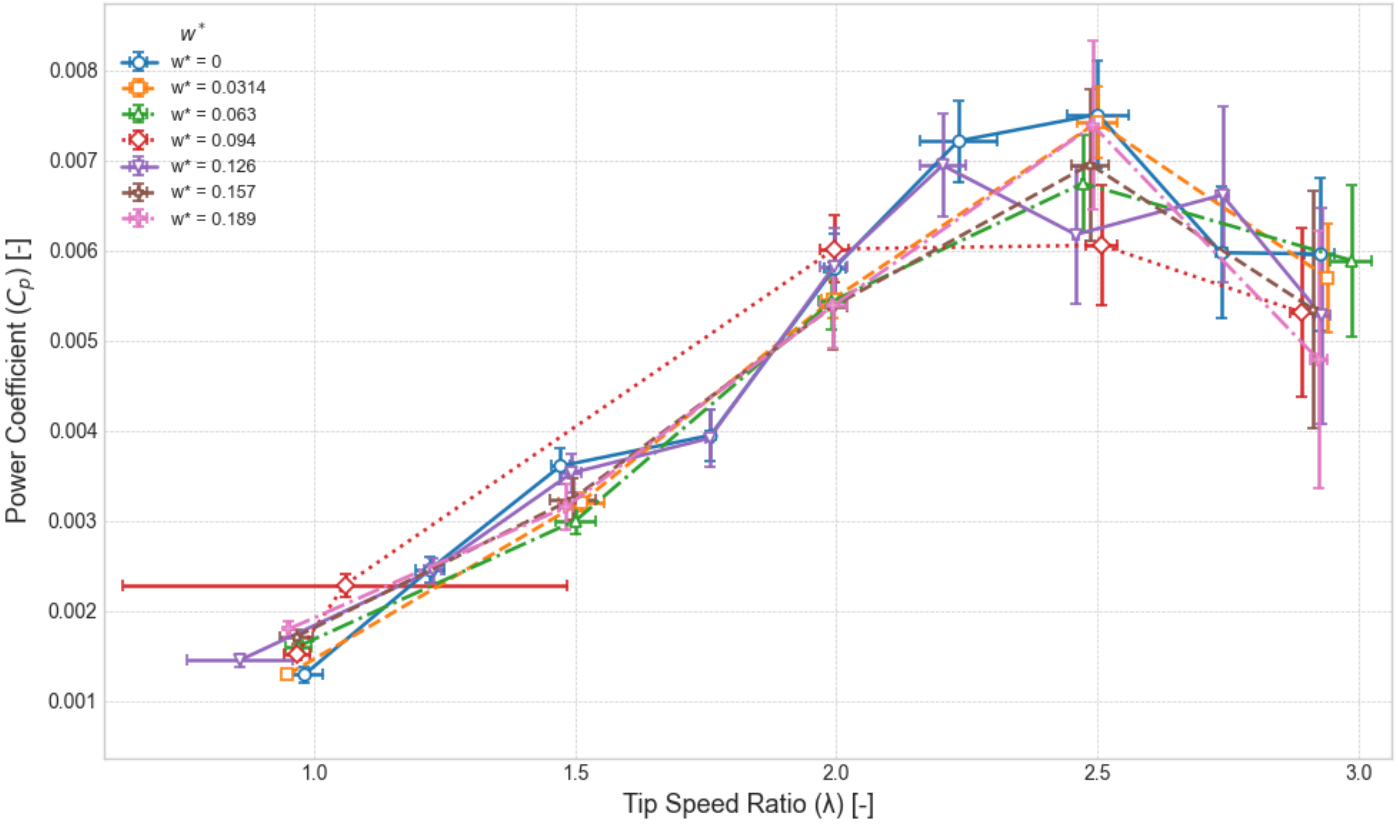

Figure 6.14: Variation of mean power coefficient C_p with inflow oscillation frequency for different λ groups, calculated using direct time-averaged torque.

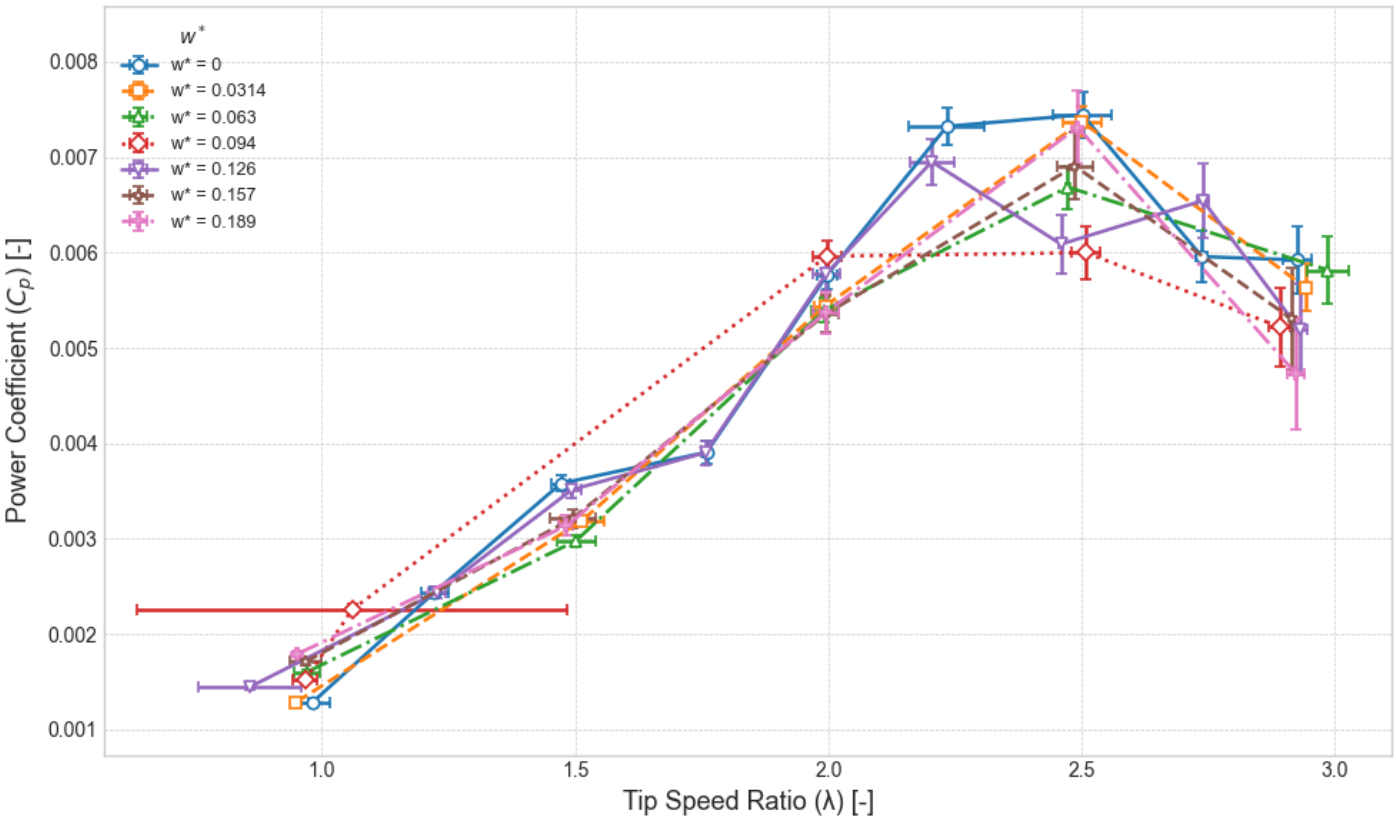

Figure 6.15: Variation of mean power coefficient C_p with inflow oscillation frequency for different λ groups, calculated using phase-binned torque values. Binning was performed over 15 blade phase intervals.

While both figures exhibit a similar overall trend, differences in absolute values and local extrema may arise from the underlying averaging method. The phase-binned approach incorporates rotor position during torque averaging, which can provide a more accurate representation of aerodynamic performance under unsteady inflow conditions. This enhances the interpretability of the heatmap patterns.

6.4.2 Effect of Dimensionless Oscillation Amplitude on Power Coefficient

Then, to isolate the impact of inflow amplitude on turbine performance, tests were conducted at a fixed dimensionless oscillation frequency of $\omega^* = 0.126$ and a constant tip-speed ratio $\lambda = 2.0$. The dimensional amplitude of the imposed inflow oscillation was incrementally varied from 0.005 m to 0.045 m, corresponding to dimensionless amplitudes $A^* = 0.1$ to $A^* = 0.9$, where $A^* = A/0.5$. These conditions were selected based on prior findings indicating peak efficiency at this frequency and λ.

The results, shown in Figure 6.16, reveal an increase in the power coefficient C_p with increasing dimensionless amplitude A^*, which then levels off at higher values, suggesting diminishing aerodynamic gains.

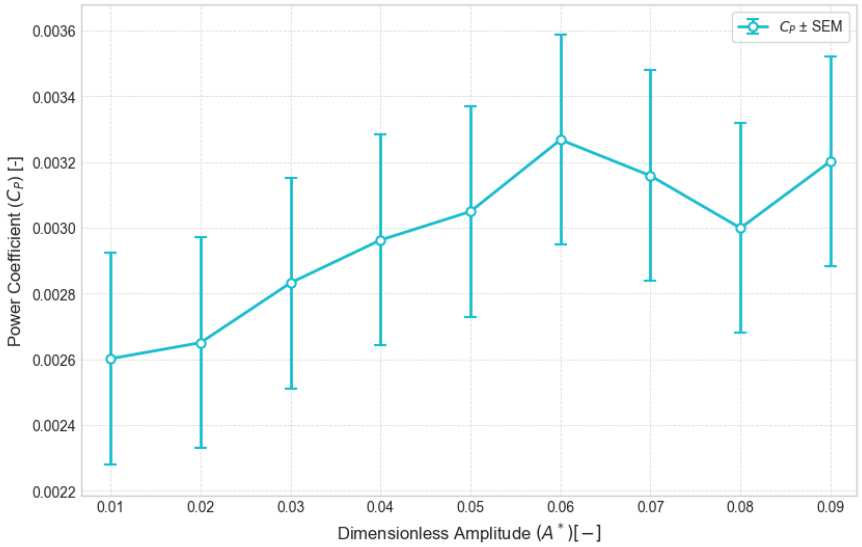

Figure 6.16: Variation of power coefficient C_p with dimensionless oscillation amplitude A^* at fixed frequency $\omega^* = 0.126$ and tip-speed ratio $\lambda = 2.0$. Increasing A^* enhances aerodynamic forcing, with diminishing returns at higher values.

6.4.3 Interaction of Rotation and Wave Phase on Turbine Torque

Finally, to investigate how turbine torque is influenced by both blade rotation and wave-induced platform motion, a two-dimensional, phase-resolved torque heatmap was generated. This visualization captures torque variations as a function of blade azimuthal angle and the phase of hexapod-induced oscillations, revealing how the interaction between rotational dynamics and unsteady inflow evolves across conditions. The main results are shown in Figure 6.17 and Figure 6.18, with sampling density in Appendix M, and coarser 10-by-10 bin versions for reference in Appendix N.

At low hexapod oscillation frequencies, the torque pattern closely follows the blade's rotational phase (i.e., tip-speed ratio), displaying two torque maxima and minima per revolution due to cyclic angle-of-attack changes (see Figure 2.6). As the frequency of oscillation increases, these torque peaks shift in phase, suggesting a growing influence of the wave-induced velocity component. This shift indicates a coupling effect, where the relative timing between platform motion and blade passage modifies the instantaneous angle of attack and, consequently, the torque output.

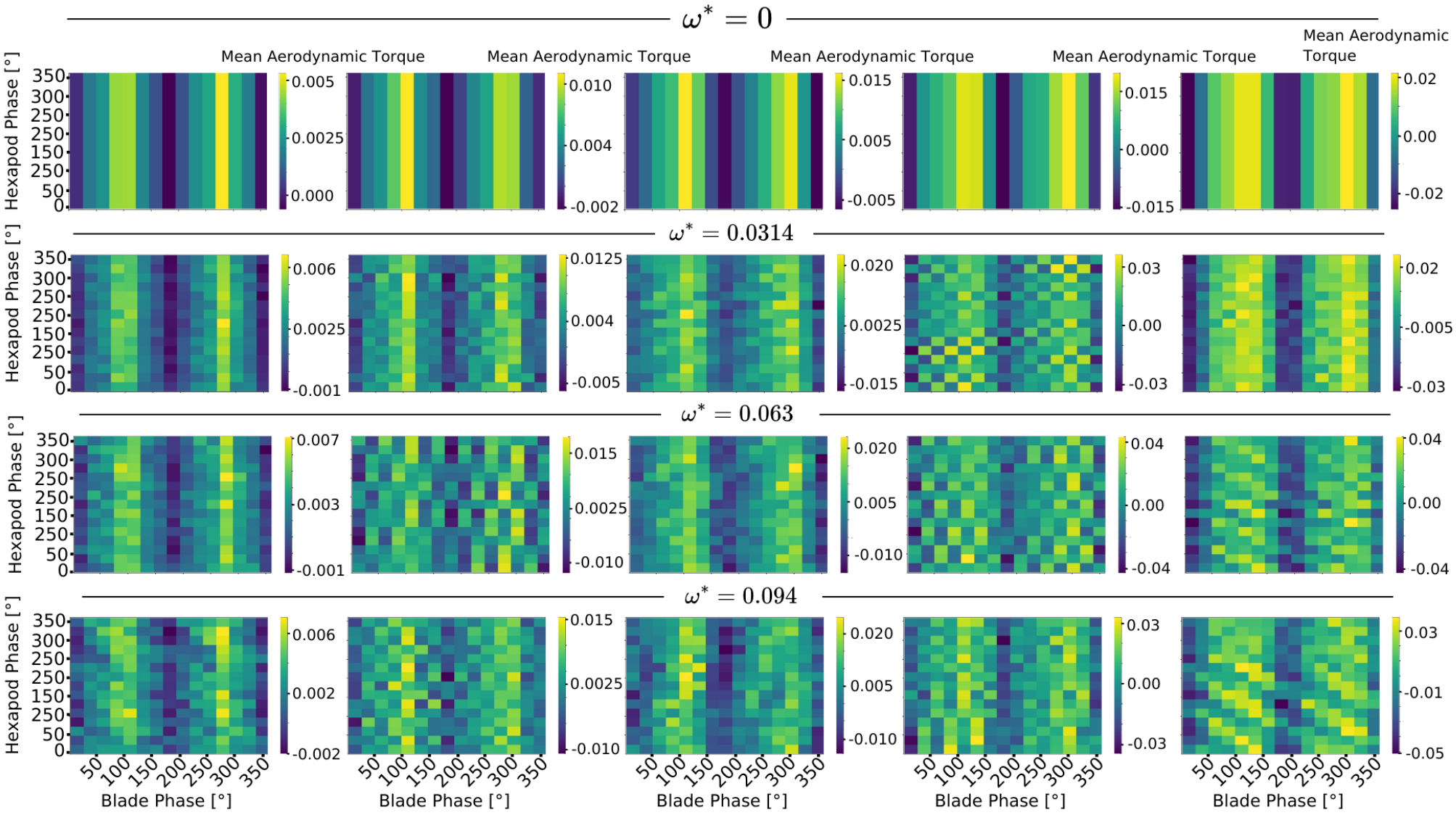

Figure 6.17: Heatmaps of torque distribution showing aerodynamic torque variation over blade azimuth and hexapod phase, for different tip-speed ratios λ and normalized frequencies $\omega^* = 0,\ 0.0314,\ 0.063,\ 0.094$ under steady inflow conditions.

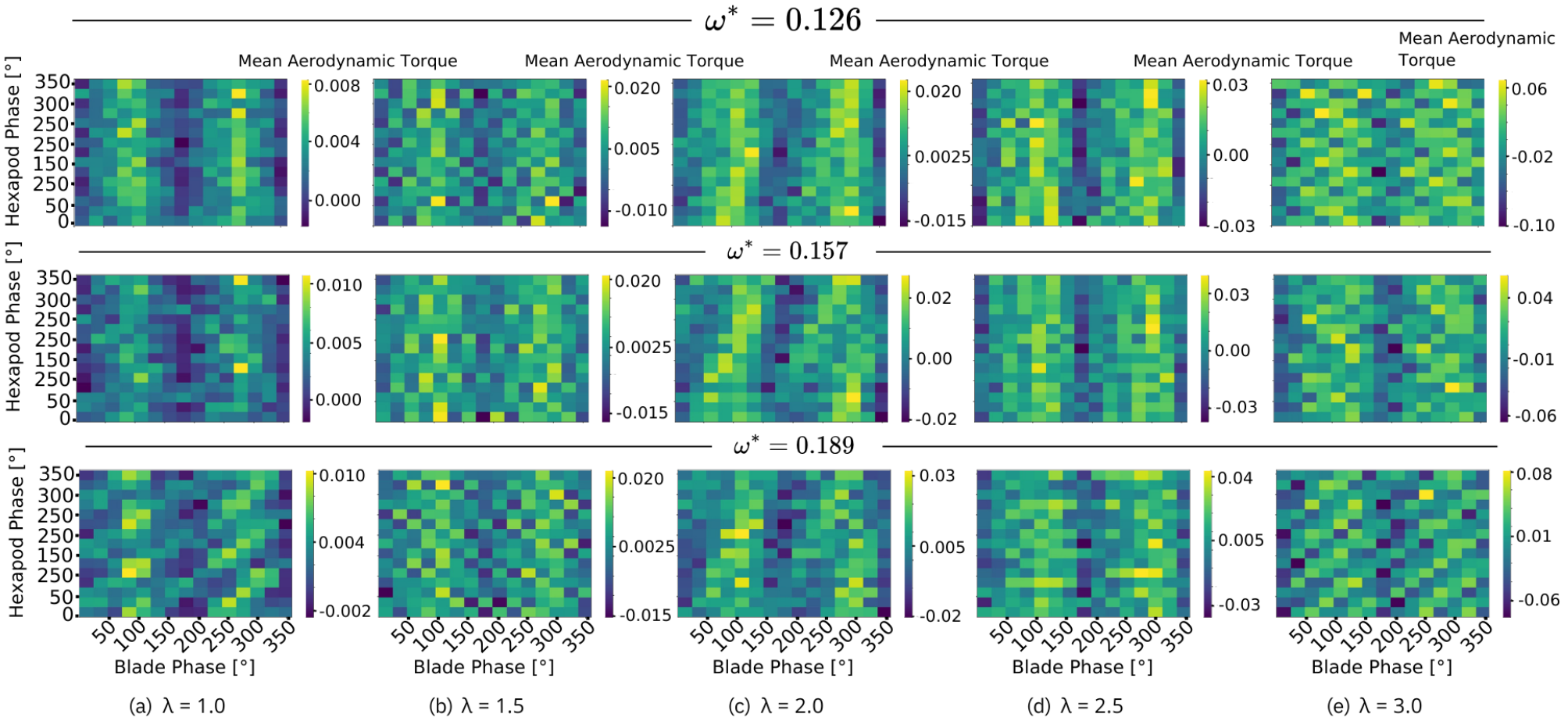

Figure 6.18: Heatmaps of torque distribution showing aerodynamic torque variation over blade azimuth and hexapod phase, for different tip-speed ratios λ and normalized frequencies $\omega^* = 0.189,\ 0.157,\ 0.126$ under steady inflow conditions.

6.5 Conclusion

This section investigated the aerodynamic performance of a single-blade Vertical Axis Wind Turbine (VAWT) under sinusoidal inflow conditions, varying the tip-speed ratio (λ), non-dimensional inflow frequency (ω^*), and amplitude (A^*), to assess their influence on power coefficient (C_p).

Under steady inflow, the turbine exhibited the expected bell-shaped power coefficient (C_p) curve with a clear optimal tip-speed ratio. However, measured C_p values were significantly lower than theoretical predictions, likely due to torque underestimation from sensor calibration issues. Time-averaged and phase-binned C_p calculations were in close agreement, validating phase-binning as a reliable method for detailed aerodynamic analysis.

With sinusoidal inflow (ω^*), the turbine's overall performance remained robust, showing only minor reductions in mean C_p near optimal λ. Similarly, varying amplitude (A^*) had little effect, with a slight increase in C_p at low amplitudes that plateaued quickly. Torque patterns transitioned from stable, blade-aligned distributions at low frequencies to more chaotic, phase-coupled structures at higher frequencies, indicating strong dynamic coupling between inflow oscillations and blade aerodynamics. Despite these complex variations, average C_p and the azimuthal position of peak torque remained largely unchanged, since ω^* had no significant effect.

These findings partially align with previous research. Danao et al. (2013) [31] reported that inflow frequency has little to no effect on performance, consistent with this study. McIntosh et al. (2008) [29] observed frequency effects most pronounced near peak efficiency, similar here, though they reported a positive influence, whereas this study suggests a slight negative trend. Danao et al. (2013) [31] predicted performance reductions with increasing amplitude, whereas this study observed a small, though uncertain, improvement.

Several limitations influenced the results and highlight areas for improvement. Environmental factors such as seasonal temperature shifts and proximity to the WindShape system may have increased local turbulence during sinusoidal tests, impacting torque measurements. Structural vibrations and potential sensor calibration errors also introduced uncertainty.

Future work should focus on improving measurement accuracy through careful sensor calibration and repeated testing to increase statistical confidence. Baseline inertial tests and vibration monitoring are also essential to isolate aerodynamic effects from mechanical influences.

7. Overall Conclusion

This work focused on characterizing the WindAI test section, designing and constructing a vertical-axis wind turbine (VAWT), and investigating the effects of sinusoidal inflow conditions typical of floating offshore environments. The central research question addressed was:

> *How do periodic wind velocities impact the energy output of vertical-axis wind turbines, and how can this be optimized using the tip speed ratio (λ)?*

Wind tunnel testing revealed that the TriSonica sensors couldn't fully capture turbulence intensity due to their limited temporal resolution, but we accounted for this during analysis. The mean flow in the central part of the tunnel was acceptably uniform. At a nominal speed of 5 m/s, the measured components were:

$$U = 4.83 \pm 0.21\,\mathrm{m/s}, \quad V = 0.054 \pm 0.15\,\mathrm{m/s}, \quad W = -0.049 \pm 0.039\,\mathrm{m/s},$$

with a turbulence intensity of

$$TI \approx 9\%.$$

Unfortunately, the tunnel's geometry and control system poorly reproduced sinusoidal wind patterns in the test section. To overcome this, we developed a novel solution: using a hexapod to oscillate the turbine and indirectly simulate the sinusoidal inflow.

Designing and constructing the custom single-blade H-Darrieus VAWT was a hands-on process that demanded numerous CAD revisions and practical modifications. The initial target solidity ratio of approximately 0.3 was adjusted after minor issues, such as bearing misalignment, led to unwanted vibration and noise. A subsequent reduction of the solidity ratio to 0.15, achieved by modifying the rods, successfully mitigated these issues at higher RPMs. Despite challenges in sourcing and modifying specific components, the final assembly proved mechanically robust and was successfully integrated with the hexapod for dynamic testing.

Sinusoidal wind experiments revealed subtle trends, though with limited statistical certainty. The dimensionless frequency ω^* showed that waves had a minimal effect on efficiency, except for a nonlinear influence on efficiency near peak performance. However, these changes remained within the standard error. Similarly, the amplitude parameter A^* did not show a large effect, although it hinted at a slight performance boost, but this remained inconclusive. Torque traces did show phase-dependent variations, reflecting dynamic blade-loading interactions. Still, these variations did not translate into meaningful gains in overall energy output.

In answer to the research question, periodic wind velocities, simulated through sinusoidal base motion, introduced subtle torque fluctuations and phase-dependent blade loading, but had little effect on overall energy output. Efficiency remained primarily governed by the tip speed ratio, with unsteady inflow effects emerging only near peak performance. In contrast to the 6.4% power increase reported by Wei and Dabiri (2022) [8] for HAWTs, similar benefits from unsteady inflow were not observed in the VAWT results presented here.

Several limitations influenced the experimental outcomes. Seasonal temperature variations and changes in the wind tunnel setup reduced the consistency of flow characterization. Meanwhile, structural vibrations and uncertainty in the torque sensor calibration introduced noise into the power output measurements, making precise efficiency estimates more challenging.

Building on this foundation, future research should tackle both experimental and analytical gaps. Enhanced flow characterization, using multi-hole probes like Oxford probes, and more stable inflow conditions would enable finer resolution of turbulence and angle-of-attack dynamics. Upgrading to a calibrated rotary torque transducer and precision-aligned bearings would boost torque and efficiency measurement accuracy. On the modeling side, focusing on tip speed ratios between 2.0 and 2.5 appears most promising for capturing key interactions between sinusoidal motion and turbine behavior. Finally, longer test durations and increased measurement cycles would reduce noise and sharpen phase-resolved data clarity.

References

[1] Gobierno de España. (2024) Actualización de datos del gobierno de españa. Accessed: 2024-12-17. [Online]. Available: https://www.lamoncloa.gob.es/info-dana/Paginas/2024/231124-datos-seguimiento-actuaciones-gobierno.aspx

[2] World Meteorological Organization. (2024) Devastating rainfall hits spain in yet another flood-related disaster. Accessed: 2024-12-17. [Online]. Available: https://wmo.int/media/news/devastating-rainfall-hits-spain-yet-another-flood-related-disaster

[3] United Nations. (2024) Causes and effects of climate change. Accessed: 2024-12-17. [Online]. Available: https://www.un.org/en/climatechange/science/causes-effects-climate-change

[4] H. Yousefi, A. Abbaspour, and H. Seraj, "Worldwide development of wind energy and co2 emission reduction," *Environmental Energy and Economic Research*, vol. 3, no. 1, pp. 1–9, 2019. [Online]. Available: https://www.eeer.ir/article_86034_150949adf5f2e7bb16b7078eb4e85e62.pdf

[5] X. Zhu, Z. Guo, Y. Zhang, X. Song, C. Cai, Y. Kamada *et al.*, "Numerical study of aerodynamic characteristics on a straight-bladed vertical axis wind turbine with bionic blades," *Energy*, vol. 239, p. 122453, 2022. [Online]. Available: https://www.sciencedirect.com/science/article/pii/S036054422102702X

[6] M. Hansen, P. Enevoldsen, and M. Abkar, "Energy harvesting via co-locating horizontal- and vertical-axis wind turbines," *Preprint*, February 2020. [Online]. Available: https://www.researchgate.net/publication/338387576

[7] D. Wood, *Small Wind Turbines*, ser. Green Energy and Technology. London, UK: Springer, 2011. [Online]. Available: https://link.springer.com/book/10.1007/978-1-84996-175-2

[8] N. J. Wei and J. O. Dabiri, "Phase-averaged dynamics of a periodically surging wind turbine," *Journal of Renewable and Sustainable Energy*, vol. 14, no. 1, p. 013305, 2022. [Online]. Available: https://pubs.aip.org/aip/jrse/article-abstract/14/1/013305/2848624/Phase-averaged-dynamics-of-a-periodically-surging?redirectedFrom=fulltext

[9] T. Ackermann, Ed., *Wind Power in Power Systems*. Chichester, West Sussex, England: John Wiley & Sons, Ltd, 2005.

[10] J. F. Manwell, J. G. McGowan, and A. L. Rogers, *Wind Energy Explained: Theory, Design and Application*, 2nd ed. Chichester, West Sussex, United Kingdom: John Wiley & Sons Ltd, 2009.

[11] A. Betz, "Das maximum der theoretisch möglichen ausnutzung des windes durch windmotoren," *Zeitschrift für das gesamte Turbinenwesen*, vol. 26, pp. 307–309, 1920.

[12] M. Blackwood, "Maximum efficiency of a wind turbine," *Undergraduate Journal of Mathematical Modeling: One + Two*, vol. 6, no. 2, 2016. [Online]. Available: https://digitalcommons.usf.edu/ujmm/vol6/iss2/2

[13] S. Gudmundsson, *General Aviation Aircraft Design: Applied Methods and Procedures*, 2nd ed. Oxford, United Kingdom: Butterworth-Heinemann, an imprint of Elsevier, 2022. [Online]. Available: https://www.sciencedirect.com/book/9780128184653/general-aviation-aircraft-design

[14] M. A. Kabir, S. Chowdhury, M. J. I. Munna, and M. Islam, "Numerical assessment of the backward facing step for naca 0015 airfoil using computational fluid dynamics," in *Proceedings of the 1st International Conference on Advances in Science, Engineering and Robotics Technology (ICASERT 2019)*. Dhaka, Bangladesh: IEEE, 2019. [Online]. Available: https://www.researchgate.net/publication/333045321_Numerical_Assessment_of_the_Backward_Facing_Step_for_NACA_0015_Airfoil_using_Computational_Fluid_Dynamics

[15] S. Ali and C.-M. Jang, "Effects of tip speed ratios on the blade forces of a small h-darrieus wind turbine," *Energies*, vol. 14, no. 13, p. 4025, 2021. [Online]. Available: https://doi.org/10.3390/en14134025

[16] P. C. Pujari, A. Jain, D. S. Nath, and N. Kumar, "Performance enhancement of savonius turbine with the application of reorienting blade mechanism," *Energy Sources, Part A: Recovery, Utilization and Environmental Effects*, July 2021. [Online]. Available: https://www.researchgate.net/publication/353197898_Performance_enhancement_of_savonius_turbine_with_the_application_of_reorienting_blade_mechanism

[17] Q. Liu, W. Miao, C. Li, W. Hao, H. Zhu, and Y. Deng, "Effects of trailing-edge movable flap on aerodynamic performance and noise characteristics of vawt," *Energy*, vol. 189, p. 116271, 2019. [Online]. Available: https://www.sciencedirect.com/science/article/pii/S0360544219319668

[18] A. Wirth and B. Chapron, "Empirical evidence of a fluctuation theorem for the wind mechanical power input into the ocean," *Nonlinear Processes in Geophysics*, vol. 28, no. 3, pp. 371–378, 2021. [Online]. Available: https://npg.copernicus.org/articles/28/371/2021/

[19] Q. Li, T. Maeda, Y. Kamada, J. Murata, K. Furukawa, and M. Yamamoto, "Effect of number of blades on aerodynamic forces on a straight-bladed vertical axis wind turbine," *Energy*, vol. 90, pp. 784–795, 2015. [Online]. Available: https://www.sciencedirect.com/science/article/pii/S0360544215010105

[20] J. O. Dabiri, "Potential order-of-magnitude enhancement of wind farm power density via counter-rotating vertical-axis wind turbine arrays," *Journal of Renewable and Sustainable Energy*, vol. 3, p. 043104, July 2011. [Online]. Available: https://pubs.aip.org/aip/jrse/article-abstract/3/4/043104/284824/Potential-order-of-magnitude-enhancement-of-wind?redirectedFrom=fulltext

[21] F. Castellani, D. Astolfi, M. Peppoloni, F. Natili, D. Buttà, and A. Hirschl, "Experimental vibration analysis of a small scale vertical wind energy system for residential use," *Machines*, vol. 7, no. 2, p. 35, 2019. [Online]. Available: https://www.mdpi.com/2075-1702/7/2/35

[22] S. Bhuyan and A. Biswas, "Investigations on self-starting and performance characteristics of simple h and hybrid h-savonius vertical axis wind rotors," *Energy Conversion and Management*, vol. 87, pp. 859–867, 2014. [Online]. Available: https://www.sciencedirect.com/science/article/pii/S0196890414006876

[23] A. A. Ayati, K. Steiros, M. A. Miller, S. Duvvuri, and M. Hultmark, "A double-multiple streamtube model for vertical axis wind turbines of arbitrary rotor loading," *Wind Energy Science*, vol. 4, pp. 653–662, 2019. [Online]. Available: https://www.researchgate.net/publication/337900287_A_double-multiple_streamtube_model_for_vertical_axis_wind_turbines_of_arbitrary_rotor_loading

[24] A.-J. Buchner, J. Soria, D. Honnery, and A. J. Smits, "Dynamic stall in vertical axis wind turbines: scaling and topological considerations," *Journal of Fluid Mechanics*, vol. 841, p. 746–766, 2018. [Online]. Available: https://www.cambridge.org/core/journals/journal-of-fluid-mechanics/article/dynamic-stall-in-vertical-axis-wind-turbines-scaling-and-topological-considerations/1DC59C2F9D2D13666EEADB3144699282

[25] AirfoilTools, "Naca 0015 airfoil – xfoil polar data," http://airfoiltools.com/airfoil/details?airfoil=naca0015-il, 2025, accessed: 2025-08-08.

[26] S. Joo, H. Choi, and J. Lee, "Aerodynamic characteristics of two-bladed h-darrieus at various solidities and rotating speeds," *Energy*, vol. 90, pp. 439–451, 2015. [Online]. Available: https://www.sciencedirect.com/science/article/pii/S0360544215009469

[27] A. Sagharichi, M. Maghrebi, and A. Arabgolarcheh, "Variable pitch blades: An approach for improving performance of darrieus wind turbine," *Journal of Renewable and Sustainable Energy*, vol. 8, pp. 53 305–953, 10 2016. [Online]. Available: https://www.researchgate.net/publication/308878936_Variable_pitch_blades_An_approach_for_improving_performance_of_Darrieus_wind_turbine

[28] R. E. Gormont, "A mathematical model of unsteady aerodynamics and radial flow for application to helicopter rotors," The Boeing Company, Vertol Division, Fort Eustis, Virginia, Tech. Rep. USAAMRDL Technical Report 72-67, May 1973.

[29] S. C. McIntosh, H. Babinsky, and T. Bertényi, "Unsteady power output of vertical axis wind turbines operating within a fluctuating free-stream," in *46th AIAA Aerospace Sciences Meeting and Exhibit*. Reno, Nevada: American Institute of Aeronautics and Astronautics (AIAA), January 2008, aIAA Paper 2008-1324. [Online]. Available: https://arc.aiaa.org/doi/10.2514/6.2008-1324

[30] L. A. Danao and R. Howell, "Effects on the performance of vertical axis wind turbines with unsteady wind inflow: A numerical study," in *50th AIAA Aerospace Sciences Meeting including the New Horizons Forum and Aerospace Exposition*. American Institute of Aeronautics and Astronautics, January 2012, copyright © 2012 by the American Institute of Aeronautics and Astronautics, Inc. All rights reserved. [Online]. Available: https://arc.aiaa.org/doi/10.2514/6.2012-1067

[31] L. A. Danao, J. Edwards, O. Eboibi, and R. Howell, "A numerical investigation into the influence of unsteady wind on the performance and aerodynamics of a vertical axis wind turbine," *Applied Energy*, vol. 116, pp. 111–124, 2013. [Online]. Available: https://www.sciencedirect.com/science/article/pii/S0306261913009513

[32] R. Howell, N. Qin, J. Edwards, and N. Durrani, "Wind tunnel and numerical study of a small vertical axis wind turbine," *Renewable*

Energy, vol. 35, no. 2, pp. 412–422, 2010. [Online]. Available: https://www.sciencedirect.com/science/article/pii/S0960148109003048

[33] D. W. Wekesa, C. Wang, Y. Wei, and L. A. M. Danao, "Influence of operating conditions on unsteady wind performance of vertical axis wind turbines operating within a fluctuating free-stream: A numerical study," *Journal of Wind Engineering and Industrial Aerodynamics*, vol. 135, pp. 76–89, 2014. [Online]. Available: https://www.sciencedirect.com/science/article/pii/S0167610514002189

[34] W.-H. Chen, J.-S. Wang, M.-H. Chang, A. T. Hoang, S. S. Lam, E. E. Kwon, and V. Ashokkumar, "Optimization of a vertical axis wind turbine with a deflector under unsteady wind conditions via taguchi and neural network applications," *Energy Conversion and Management*, vol. 254, p. 115209, 2022. [Online]. Available: https://doi.org/10.1016/j.enconman.2022.115209

[35] N. J. Wei and J. O. Dabiri, "Power-generation enhancements and upstream flow properties of turbines in unsteady inflow conditions," *J. Fluid Mech.*, vol. 966, p. A30, 2023. [Online]. Available: https://doi.org/10.1017/jfm.2023.454

[36] N. J. Wei, A. E. Makdah, J. Hu, F. Kaiser, D. E. Rival, and J. O. Dabiri, "Wake dynamics of wind turbines in unsteady streamwise flow conditions," *Journal of Fluid Mechanics*, vol. 1000, p. A66, 2024. [Online]. Available: https://www.cambridge.org/core/journals/journal-of-fluid-mechanics/article/wake-dynamics-of-wind-turbines-in-unsteady-streamwise-flow-conditions/F51D1C7B1CE457CCD467E978C16483F4

[37] WindShape, "Windshape - digital wind facilities," 2025, accessed: 2025-01-12. [Online]. Available: https://windshape.com/

[38] R. Putzu, R. Boulandet, B. Rutschmann, T. Bujard, F. Noca, G. Catry, and N. Bosson, "Aeroacoustic measurements on a free-flying drone in a windshaper wind tunnel," in *Proceedings of the International e-Symposium on UAV/UAS Noise*. Remote from Paris: HES-SO Genève, October 2020.

[39] A. Van Vondelen, D. Van Der Hoek, S. Navalkar, and J. Van Wingerden, "Synchronized dynamic induction control: An experimental investigation," *Journal of Physics: Conference Series*, vol. 2767, no. 3, p. 032027, jun 2024. [Online]. Available: https://iopscience.iop.org/article/10.1088/1742-6596/2767/3/032027

[40] B. D. Vos, B. M. Harder, T. A. Huisman, J. Gutknecht, and J. W. V. Wingerden, "Mimicking the helix with a porous disc for wind tunnel testing," *Journal of Physics: Conference Series*, vol. 2767, no. 9, p. 092063, 2024. [Online]. Available: https://doi.org/10.1088/1742-6596/2767/9/092063

[41] A. S. Morris and R. Langari, "Chapter 16 - flow measurement," in *Measurement and Instrumentation (Second Edition)*, A. S. Morris and R. Langari, Eds. Boston: Academic Press, 2016, pp. 493–529. [Online]. Available: https://www.sciencedirect.com/science/article/pii/B9780128008843000162

[42] N. Nait Bouda, C. Rey, J. Rosant, and T. Benabid, "Turbulent wall jet interaction with a backward facing step," in *Engineering Turbulence Modelling and Experiments 6*, W. Rodi and M. Mulas, Eds. Amsterdam: Elsevier Science B.V., 2005, pp. 471–480. [Online]. Available: https://www.sciencedirect.com/science/article/pii/B9780080445441500455

[43] S. Harmand, J. Pellé, S. Poncet, and I. Shevchuk, "Review of fluid flow and convective heat transfer within rotating disk cavities with impinging jet," *International Journal of Thermal Sciences*, vol. 67, pp. 1–30, 2013. [Online]. Available: https://www.sciencedirect.com/science/article/pii/S1290072912003171

[44] G. Comte-Bellot, "Hot-wire anemometry," *Annual Review of Fluid Mechanics*, vol. 8, pp. 209–231, 1976. [Online]. Available: https://www.annualreviews.org/content/journals/10.1146/annurev.fl.08.010176.001233

[45] T. Yasa and G. Paniagua, "Robust procedure for multi-hole probe data processing," *Flow Measurement and Instrumentation*, vol. 26, pp. 46–54, 2012. [Online]. Available: https://www.sciencedirect.com/science/article/pii/S0955598612000210

[46] B. F. Hall and T. Povey, "The oxford probe: an open access five-hole probe for aerodynamic measurements," *Measurement Science and Technology*, vol. 28, no. 3, p. 035004, 2017. [Online]. Available: https://iopscience.iop.org/article/10.1088/1361-6501/aa53a8

[47] LI-COR Inc., "Li-560 sphere," 2025, accessed: 2025-01-15. [Online]. Available: https://www.licor.com/products/trisonica/LI-560-sphere

[48] P. Bachant and M. Wosnik, "Effects of reynolds number on the energy conversion and near-wake dynamics of a high solidity vertical-axis cross-flow turbine," *Energies*, vol. 9, no. 2, p. 73, 2016. [Online]. Available: https://doi.org/10.3390/en9020073

[49] L. Du, G. Ingram, and R. G. Dominy, "Experimental study of the effects of turbine solidity, blade profile, pitch angle, surface roughness, and aspect ratio on the h-darrieus wind turbine self-starting and overall performance," *Energy Science and Engineering*, vol. 7, no. 6, pp. 2421–2436, 2019. [Online]. Available: https://scijournals.onlinelibrary.wiley.com/doi/full/10.1002/ese3.430

[50] Y. Yan, E. Avital, J. Williams, and J. Cui, "Aerodynamic performance improvements of a vertical axis wind turbine by leading-edge protuberance," *Journal of Wind Engineering & Industrial Aerodynamics*, vol. 211, p. 104535, 2021. [Online]. Available: https://www.sciencedirect.com/science/article/pii/S0167610521000210

[51] A.-J. Buchner, M. Lohry, L. Martinelli, J. Soria, and A. Smits, "Dynamic stall in vertical axis wind turbines: Comparing experiments and computations," *Journal of Wind Engineering and Industrial Aerodynamics*, vol. 146, pp. 163–171, 2015. [Online]. Available: https://www.sciencedirect.com/science/article/pii/S0167610515002159

[52] J. M. Edwards, L. Angelo Danao, and R. J. Howell, "Novel experimental power curve determination and computational methods for the performance analysis of vertical axis wind turbines," *Journal of Solar Energy Engineering, Transactions of the ASME*, vol. 134, no. 3, 2012. [Online]. Available: https://asmedigitalcollection.asme.org/solarenergyengineering/article-abstract/134/3/031008/464821/Novel-Experimental-Power-Curve-Determination-and?redirectedFrom=fulltext

[53] O. Eboibi, L. A. M. Danao, and R. J. Howell, "Experimental investigation of the influence of solidity on the performance and flow field aerodynamics of vertical axis wind turbines at low reynolds numbers," *Renewable Energy*, vol. 92, pp. 474–483, 2016. [Online]. Available: https://www.sciencedirect.com/science/article/pii/S096014811630129X

[54] A. Kassimali, *Structural Analysis*, 6th ed. Cengage, 2017.

[55] S. F. Hoerner, *Fluid-Dynamic Drag: Practical Information on Aerodynamic Drag and Hydrodynamic Resistance*. Hoerner Fluid Dynamics, 1965.

[56] *Draft National Annex to BS EN 1990: Basis of Structural Design*, British Standards Institution (BSI) Std., 2003, dPC: 03/700353 DC. [Online]. Available: https://www.newsteelconstruction.com/wp/eurocode-design-factors-and-limits/

[57] D. Duty, M. K. Johan, Y. Samy, M. E. R. Indarah, M. S. S. Shaharudin, D. H. Didane, and B. Manshoor, "Performance analysis of vawt with h-darrieus rotor using 2d cfd modelling," *Journal of Design for Sustainable and Environment*, vol. 5, no. 1, pp. 5–10, 2023.

[58] R. E. Castillo and E. M. Rojas, "Revisiting the hilbert transform of periodic functions," *Mathematische Semesterberichte*, vol. 72, pp. 29–49, 2025. [Online]. Available: https://doi.org/10.1007/s00591-025-00390-z

[59] R. Holyst and A. Poniewierski, *Thermodynamics for Chemists, Physicists and Engineers*, 1st ed. Springer Dordrecht, 2012. [Online]. Available: https://doi.org/10.1007/978-94-007-2999-5

[60] Wolfram Resource System, "Sutherland's formula," Available online at https://resources.wolframcloud.com/FormulaRepository/resources/Sutherlands-Formula, 2021, original publication date: April 10, 2021. Accessed: July 31, 2025.

[61] S. B. Pope, *Turbulent Flows*. Cambridge University Press, 2000.

[62] Y. A. Cengel and J. M. Cimbala, *Fluid Mechanics: Fundamentals and Applications*. McGraw-Hill Education, 2014.

[63] G. I. Taylor, "The spectrum of turbulence," *Proceedings of the Royal Society of London. Series A, Mathematical and Physical Sciences*, vol. 164, no. 916, pp. 476–490, 1938. [Online]. Available: https://royalsocietypublishing.org/doi/epdf/10.1098/rspa.1938.0032

[64] L. Battisti, "Design options to improve the dynamic behavior and the control of small h-darrieus vawts," *Applied Sciences*, vol. 11, no. 19, 2021. [Online]. Available: https://www.mdpi.com/2076-3417/11/19/9222

[65] P. G. Remya, S. Vishnu, B. Praveen Kumar, T. M. Balakrishnan Nair, and B. Rohith, "Teleconnection between the north indian ocean high swell events and meteorological conditions over the southern indian ocean," *Journal of Geophysical Research: Oceans*, vol. 121, no. 10, pp. 7476–7494, 2016.

[Online]. Available: https://agupubs.onlinelibrary.wiley.com/doi/abs/10.1002/2016JC011723

[66] L. Wu, E. Sahlée, E. Nilsson, and A. Rutgersson, "A review of surface swell waves and their role in air–sea interactions," *Ocean Modelling*, vol. 190, p. 102397, 2024. [Online]. Available: https://www.sciencedirect.com/science/article/pii/S1463500324000842

A. Setup Configuration

To prepare the setup, follow these steps:

Hardware Setup

1. Adjust the WindShape to the correct height.
2. Turn on the main switch (on the wall) by rotating it **90° clockwise**.
3. Push the lever in the right WindShape chamber to the **green side (right)**.
    - If it does not move easily, first push it completely to the **left** and then back to the **right**.
4. Press the **white power button** in the left WindShape chamber to turn on the power.
5. Allow the computer in the left chamber at least **one minute** to boot up.
    - If it does not turn on automatically, press the power button on the computer manually.

Software Setup

1. Open the web interface at `https://robotgui/`.
2. Log in using the provided credentials by the lab staff:
    - **Username:** ******
    - **Password:** **********
3. Click **"Start Drivers"**.
4. Click **"Switch to WindShape"** (this will open a new tab).
5. In the new tab, **turn on WindShape**.
6. Click **"Switch to PowerBox"** (another new tab will open).
7. Under **"Robot Power"**, click **"All On"**.
8. Return to the **"XYZ Robot Control Panel"** tab.

B. Turbulence vs Temperature

To assess whether a 2°C temperature variation influences turbulence intensity in the wind tunnel, we analyze its impact on air properties relevant to flow dynamics, using [59].

B.1 Air Density

Using the ideal gas law at constant pressure, air density ρ is approximated as:

$$\rho = \frac{p}{RT}$$

where:

- $p = 101325\,\text{Pa}$ (atmospheric pressure),
- $R = 287\,\text{J}/(\text{kg}\cdot\text{K})$ (specific gas constant for air),
- T is absolute temperature in Kelvin.

Calculating density at:

$$T_1 = 22°C = 295.15\,K, \quad T_2 = 23°C = 296.15\,K,$$

we find:

$$\rho_1 = \frac{101325}{287 \times 295.15} = 1.196\,\text{kg/m}^3,$$
$$\rho_2 = \frac{101325}{287 \times 296.15} = 1.192\,\text{kg/m}^3.$$

The relative change in density is:

$$\frac{\Delta\rho}{\rho_2} = \frac{1.196 - 1.192}{1.192} \approx 0.0034 = 0.34\%.$$

B.2 Dynamic Viscosity

Dynamic viscosity μ varies with temperature according to Sutherland's formula [60]:

$$\mu = \mu_0 \frac{(T/T_0)^{3/2}(T_0 + S)}{T + S},$$

with reference values:

$$T_0 = 291.15\,K, \quad \mu_0 = 18.27 \times 10^{-6}\,\text{Pa} \cdot \text{s}, \quad S = 120\,K.$$

Evaluating μ at T_1 and T_2:

$$\mu_1 \approx 18.47 \times 10^{-6}\,\text{Pa} \cdot \text{s},$$

$$\mu_2 \approx 18.52 \times 10^{-6}\,\text{Pa} \cdot \text{s}.$$

The relative change in dynamic viscosity is:

$$\frac{\Delta\mu}{\mu_1} = \frac{18.52 - 18.47}{18.47} \approx 0.003 = 0.3\%.$$

B.3 Kinematic Viscosity and Reynolds Number

Kinematic viscosity ν is defined as:

$$\nu = \frac{\mu}{\rho}.$$

Calculating ν at both temperatures:

$$\nu_1 = \frac{18.47 \times 10^{-6}}{1.196} = 1.544 \times 10^{-5}\,\text{m}^2/\text{s},$$

$$\nu_2 = \frac{18.52 \times 10^{-6}}{1.192} = 1.554 \times 10^{-5}\,\text{m}^2/\text{s}.$$

The relative change in kinematic viscosity is:

$$\frac{\Delta\nu}{\nu_1} = \frac{1.554 - 1.544}{1.544} \approx 0.0065 = 0.65\%.$$

Since Reynolds number $Re = \frac{UL}{\nu}$ (with velocity U and characteristic length L constant), it changes inversely with ν:

$$\frac{\Delta Re}{Re} \approx -\frac{\Delta\nu}{\nu} \approx -0.65\%.$$

B.4 Conclusion

A 2°C temperature increase causes roughly a 0.65% change in kinematic viscosity and Reynolds number, which translates to a negligible effect on turbulence intensity for the conditions studied. Therefore, temperature variation of this magnitude can be safely ignored in the analysis.

C. Measurement Process

The following steps outline the data collection procedure:

1. Open **Anaconda PowerShell Prompt**.
2. Navigate to the Python script's directory (ask the lab staff for the script that extracts the data):

   ```
   cd C:\Users\YourName\Documents\Project\Data
   ```

3. Start the monitoring script and save the output:

   ```
   python monitor.py --output test1
   ```

4. Use the **XYZ Robot** tab in the browser to move the robot.
5. To stop data recording, return to the **Anaconda PowerShell Prompt** and press:

   ```
   Ctrl + C
   ```

6. Open **VS Code** to verify the recorded file.

D. Ending of Experiment

Once the experiment has concluded, it is important to follow the proper shutdown procedure to ensure all equipment is safely powered off and the system is securely shut down. The process can be divided into two main phases: shutting down the system through the browser interface and physically powering off the equipment.

1. Shutdown via the Browser Interface:

1. Open the 'Powerbox' tab in the browser to begin the shutdown process.
2. Switch off the Robot power to ensure it is no longer active.
3. Once the Robot has been powered off, close the 'PowerBox' tab to confirm the shutdown.
4. Proceed to the 'WindShape' tab in the browser and turn off the WindShape system.
5. After WindShape has been powered off, close the 'WindShape' tab to finalize this step.
6. Navigate to the 'XYZ Robot Control' tab in the browser in preparation for the final shutdown phase.
7. Click 'Turn off drivers' to deactivate the robot's driving mechanisms.
8. Finally, close the website by navigating to `https://robotgui/` and shutting it down.

2. Physical Equipment Shutdown:

1. Verify that the WindShape computer is turned off in the left chamber.
2. Press the button located below the white button in the left chamber to turn off the power.
3. In the right chamber, move the lever to the red side (left) to cut off power.
4. Turn off the main power switch on the wall by rotating it 90° counterclockwise.
5. Finally, lower the WindShape system to the floor to complete the shutdown process.

E. Biases Background Noise

Background velocity biases in the x-, y-, and z-directions are shown in Figures E.1–E.3.

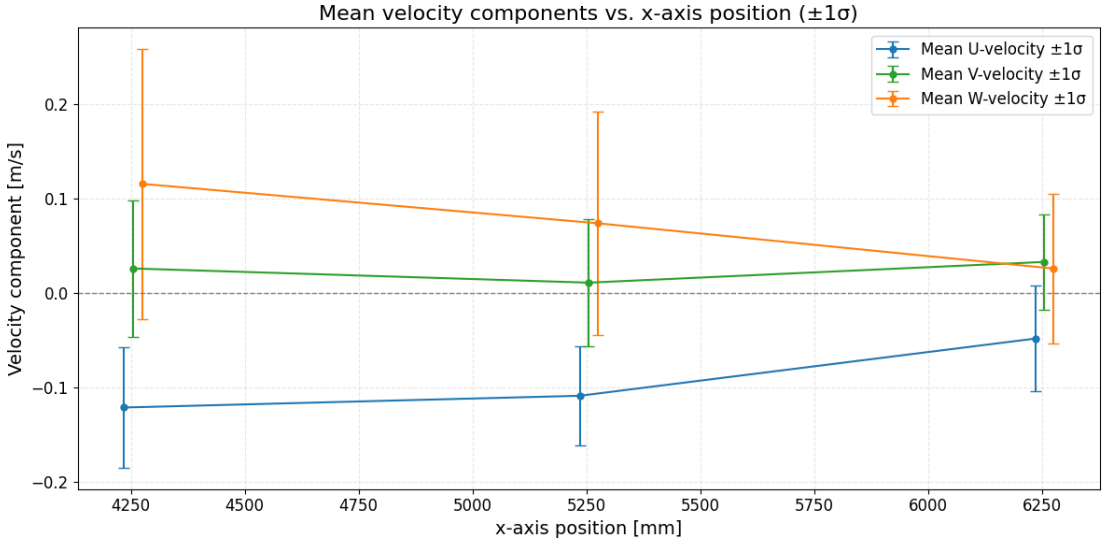

Figure E.1: Velocity bias in the x-direction. Minor deviations are small relative to the standard deviation. Horizontal axis slightly shifted for clarity.

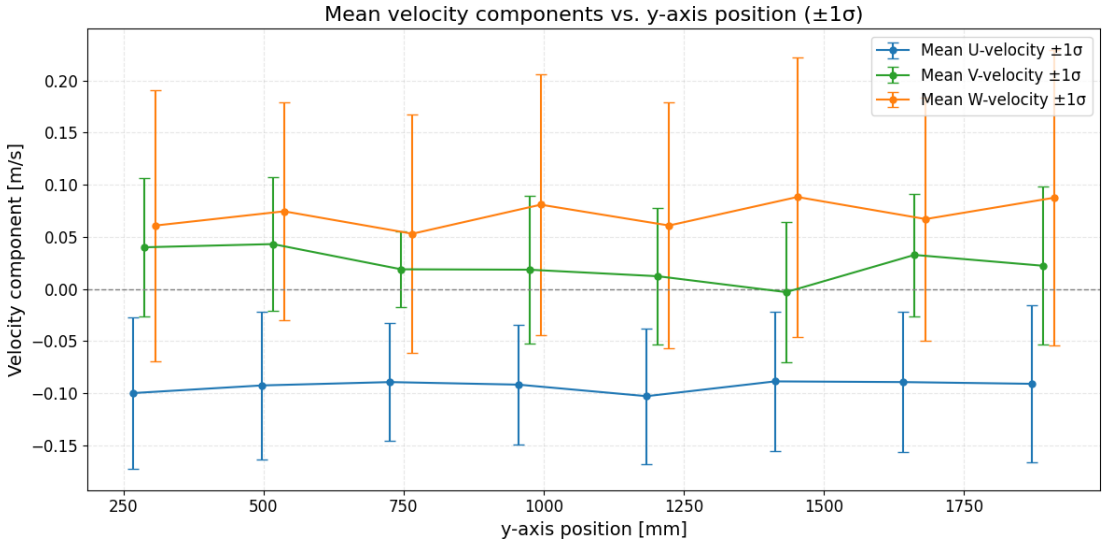

Figure E.2: Velocity bias in the y-direction. No clear trend; deviations within expected uncertainty. Axis slightly shifted for clarity.

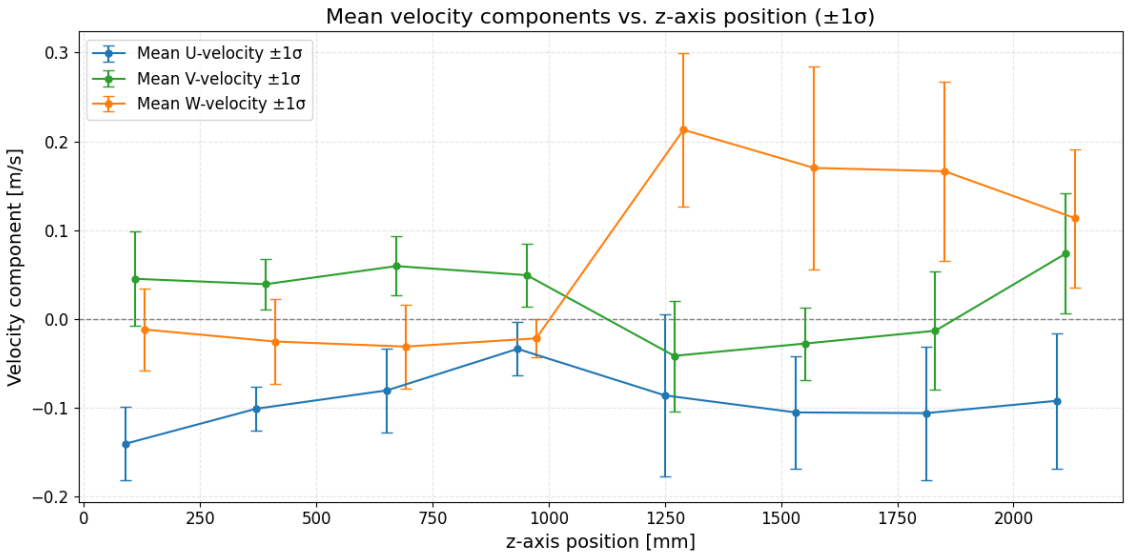

Figure E.3: Velocity bias in the z-direction. Small vertical offset relative to the standard deviation. Axis slightly shifted for clarity.

These plots show the spatial variation of background velocity biases in each coordinate direction. Although minor deviations can be observed, their magnitude relative to the measurement uncertainty suggests they have a limited impact on the baseline flow characterization. This indicates generally stable and unbiased background conditions in the wind tunnel.

F. Turbulence Spectrum Limits

In turbulent flows, the inertial subrange, where energy cascades from large to small eddies, typically begins at a frequency associated with the turnover timescale of the energy-containing eddies. In this case, the fans generating the flow are estimated to have a characteristic length scale of about 10 cm (diameter of the fans). With a mean flow velocity of approximately 5 m/s, the characteristic timescale is:

$$\tau = \frac{L}{\bar{U}} = \frac{0.1 \text{ m}}{5 \text{ m/s}} = 0.02 \text{ s} \quad \Rightarrow \quad f_L = \frac{1}{\tau} = 50 \text{ Hz}$$

This frequency, $f_L \approx 50$ Hz, represents the approximate onset of the inertial subrange, beyond which the turbulent energy cascade is expected to follow the Kolmogorov $-5/3$ scaling. However, the data are sampled at 100 Hz, imposing a Nyquist limit of 50 Hz. As a result, turbulent fluctuations above this frequency cannot be resolved, and the measurement system is unable to capture the inertial subrange or the dissipation range. As shown in Figure F.1, the measured spectrum remains relatively flat up to the Nyquist limit. This flattening is primarily due to the spectral cutoff imposed by the sampling rate, but finite sensor bandwidth, anti-aliasing filters, and high-frequency noise may also contribute.

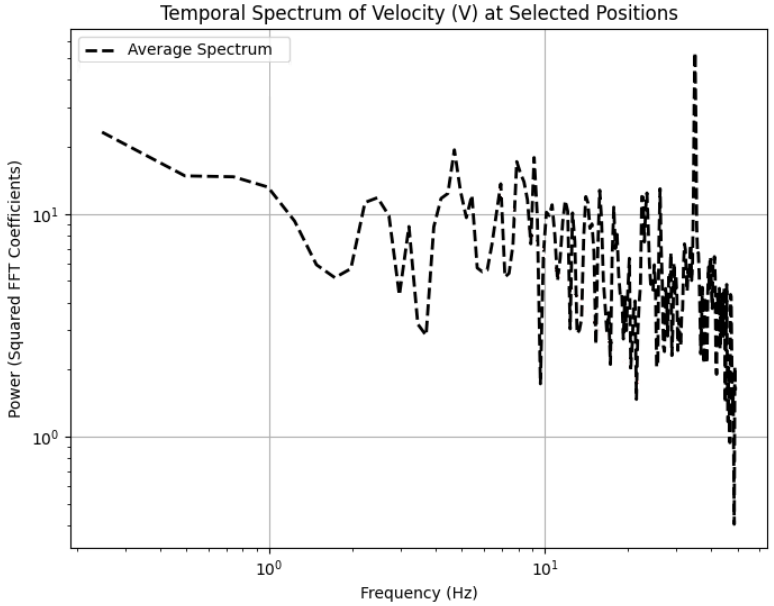

Figure F.1: Temporal velocity spectrum at SX = 4255.0. The red line shows the theoretical $-5/3$ slope, which the measured flat spectrum does not follow, indicating that the inertial subrange is unresolved.

To visualize this more clearly, Figure F.2 presents an idealized turbulent energy spectrum on a log-log scale, divided into distinct regions: the energy-containing range, the inertial subrange, and the dissipation range. The curve includes noise in the low-frequency range and follows the characteristic $-5/3$ slope in the inertial subrange, ending at the Kolmogorov frequency f_η. Annotations below the curve indicate which parts of the spectrum are captured by the sensor and which are not. The unmeasured portion, primarily in the higher-frequency range, represents turbulent energy that must be estimated to account for the full energy spectrum.

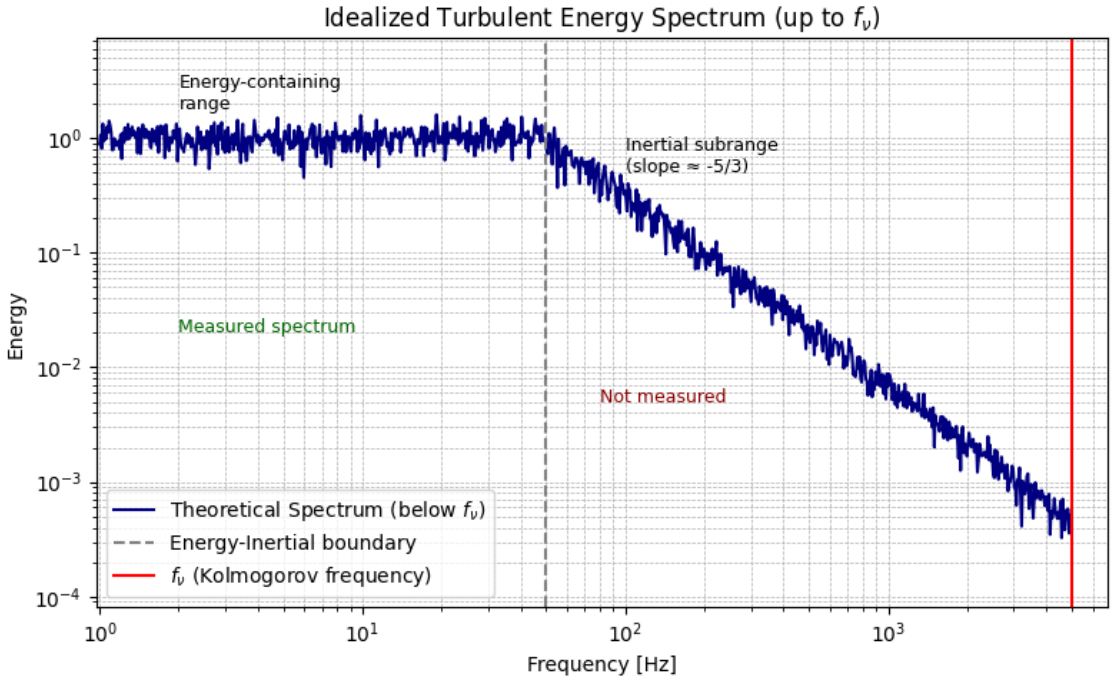

Figure F.2: Example of idealized turbulent energy spectrum shown on a log-log scale. The energy-containing range is approximately constant with noise until 50 Hz, followed by an inertial subrange exhibiting the characteristic $-5/3$ slope. The spectrum ends at the Kolmogorov frequency $f_\eta \approx 3.7$ kHz. The lower portion of the plot indicates which regions are measured and which are not captured by the sensor, highlighting the portion of turbulent energy that must be estimated.

To estimate how much turbulent energy is missing, we assume that the inertial subrange of the turbulence spectrum begins at 50 Hz and continues up to the Kolmogorov scale. In the inertial subrange, the classical 1D Kolmogorov spectrum applies [61]:

$$E(k) = C\varepsilon^{2/3}k^{-5/3},$$

where:

- $E(k)$ is the spectral energy density as a function of wavenumber,
- ε is the turbulent dissipation rate,
- $C \approx 0.5$ is the Kolmogorov constant for the 1-D longitudinal spectrum [61]

We begin by estimating the dissipation rate using [61] (order-of-magnitude):

$$\varepsilon = \frac{u'^3}{L}$$

Assuming a mean velocity $\bar{U} = 5$ m/s, a measured TI of 8% ($u' = 0.4$ m/s), and an integral length scale $L = 0.1$ m, we find:

$$\varepsilon = \frac{(0.4)^3}{0.1} = 0.64 \text{ m}^2/\text{s}^3$$

The Kolmogorov length scale η is [61]:

$$\eta = \left(\frac{\nu^3}{\varepsilon}\right)^{1/4}$$

with the kinematic viscosity of air $\nu \approx 1.5 \times 10^{-5}$ m^2/s [62]. Substituting:

$$\eta = \left(\frac{(1.5 \times 10^{-5})^3}{0.64}\right)^{1/4} \approx 0.00027 \text{ m}$$

Using Taylor's hypothesis [63], we convert this to a frequency:

$$f_\eta = \frac{\bar{U}}{2\sqrt{2\pi}\eta} \approx 3.7 \text{ kHz}$$

The integration bounds for the missing energy are estimated using Taylor's frozen turbulence hypothesis [63], which assumes that turbulent structures are advected past the sensor without significant evolution. This common approximation is reasonable here, given the moderate turbulence intensity ($TI \approx 8\%$), and allows us to convert temporal frequencies to spatial wavenumbers:

$$k = \frac{2\sqrt{2\pi}\, f}{\bar{U}}.$$

This gives the bounds for integration:

$$k_L = \frac{2\sqrt{2\pi} \cdot 50}{5} \approx 50 \text{ m}^{-1}, \quad k_\eta = \frac{2\sqrt{2\pi} \cdot 3700}{5} \approx 3700 \text{ m}^{-1}.$$

The energy in the unresolved range is then calculated by integrating the Kolmogorov spectrum in wavenumber space:

$$E_{\text{missing}} = \int_{k_L}^{k_\eta} E(k)\, dk = \frac{3}{2} C \varepsilon^{2/3} \left(k_L^{-2/3} - k_\eta^{-2/3} \right).$$

Substituting the values:

$$\varepsilon^{2/3} \approx 0.743, \quad k_L^{-2/3} \approx 0.0737, \quad k_\eta^{-2/3} \approx 0.0042,$$

$$E_{\text{missing}} \approx \frac{3}{2} \cdot 0.5 \cdot 0.743 \cdot (0.0743 - 0.0042) \approx 0.04 \text{ m}^2/\text{s}^2.$$

The measured turbulent energy is:

$$u'^2_{\text{measured}} = (0.4)^2 = 0.16 \text{ m}^2/\text{s}^2$$

Thus, the fraction of turbulent energy that is missing due to the unresolved spectrum is:

$$\frac{E_{\text{missing}}}{u'^2_{\text{measured}} + E_{\text{missing}}} = \frac{0.04}{0.16 + 0.04} \approx 20\%$$

This means that the measured turbulence intensity underestimates the true turbulence by approximately 20%. Correcting for this, the true velocity variance becomes:

$$u'^2_{\text{true}} = \frac{u'^2_{\text{measured}}}{1 - 0.2} = \frac{0.16}{0.8} \approx 0.2 \text{ m}^2/\text{s}^2$$

$$u'_{\text{true}} = \sqrt{0.2} \approx 0.447 \text{ m/s}, \quad \Rightarrow \quad TI_{\text{true}} = \frac{0.447}{5} \approx 9\%$$

Conclusion: The estimated 20% of unresolved turbulent energy per component translates to an increase of about 1 percentage point in the turbulence intensity, raising TI from 8% to approximately 9%. This highlights the importance of considering spectral resolution limitations in truncated or noise-contaminated measurements.

G. RMS Error Maps Across the Measurement Volume

Figure G.1 shows RMS error maps for different streamwise positions, visualizing how the measured flow deviates from ideal sinusoidal patterns across the y-z plane.

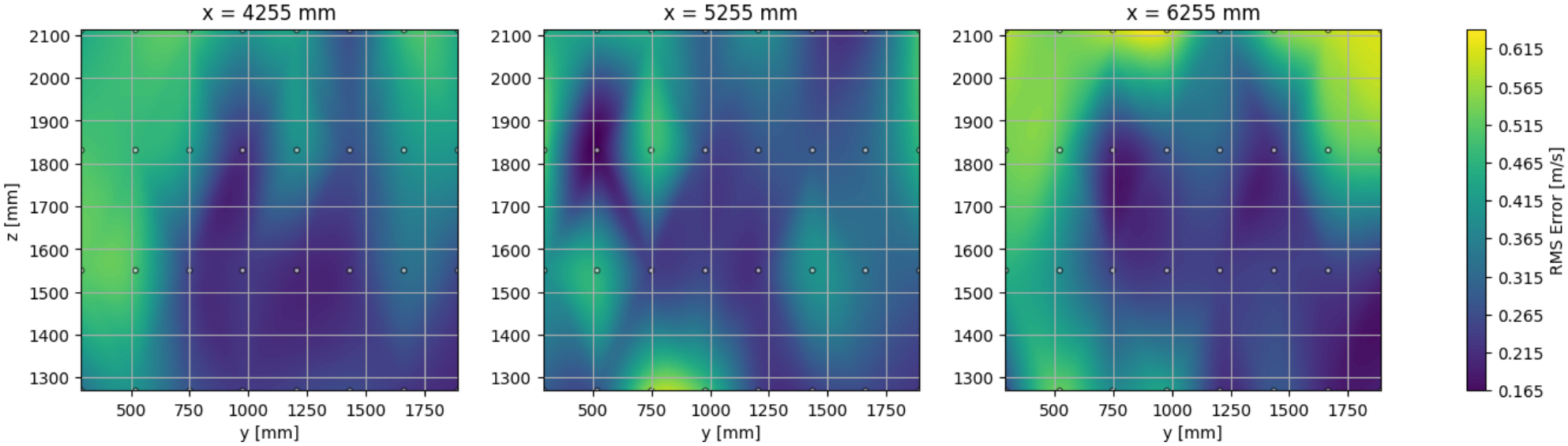

Figure G.1: RMS error maps over the y-z plane at $x = 4255.0$, 5255.0, and 6255.0, showing deviation from ideal 0.2 Hz sinusoids with amplitudes of 1 m/s.

H. Hexapod Instructions

Pre-Calculated Motion Instructions

A. System Initialization

1. Power on the hexapod system.
2. Turn on the PC.
3. Ensure the emergency stop button is released (OFF).

B. Software Setup

4. Launch MATLAB 2020 or 2021.
5. Navigate to:

   `C:/Users/Public/Documents/Hexapod software 2025 02 05 - Copy/`

6. Run the script `setup_hexapod2.m`.

C. Driver Deployment

7. Open the Simulink model `Hexapod2_Driver_kin_a.slx`
   Note: The "_a" suffix denotes AI/O modifications.
8. Build and deploy the model.
9. Verify the model is running in QUARC.

D. Calibration and Homing

10. Open and deploy `Hexapod2_Controller_Calibration_a.slx`.
11. Open and deploy `Hexapod2_Controller_Homing_a.slx`.

E. Motion File Creation

12. Navigate to the folder `ImposedMotion6Dof`.
13. Run a motion script, e.g., `MAKE_sine_6dof_SingleDof_xMilo.m`.
14. This generates a `.mat` file saved in a subfolder.

F. Load Motion File

15. Return to the main folder:
    `C:/Users/Public/Documents/Hexapod software 2025 02 05 - Copy/`
16. Import the generated `.mat` file into MATLAB workspace using the *Import Data* tool (Home tab). Navigate to `ImposedMotion6dof/Tables` and select the desired file.

G. Execute Motion

17. Open the Simulink model `Hexapod2_Controller_ImposedMotion6Dof_a.slx`.
18. Run the model and monitor the motion.
19. Wait until the simulation completes.

H. Repeat Procedure (if needed)

20. To run a different motion, repeat steps 12–19.

I. Software Setup & Measurement

The following steps outline the full experimental workflow, divided into one-time software initialization and the repeated measurement process used for each test case.

Software Initialization (performed once per session):

1. Launch **MATLAB 2020** and open the Simulink model available at the following 4TU.ResearchData repository:

   `This PC/Documents/MATLAB/untitled.slx`

2. Ensure the MicroLabBox (dSPACE RTI 1202) is connected and recognized.

3. Press **Ctrl+B** to build the model.

4. Launch **ControlDesk 6.4** and open the project file at:

   `C:/Users/Milodeleeuw/dSPACE/Project_001/Experiment_001`

5. Load the layout file `Layout1.lay` to monitor and control the system.

Measurement Procedure (repeated for each test case):

1. Activate the wind tunnel to establish steady airflow.

2. Start the turbine and adjust the duty cycle to reach the desired RPM.

3. Initiate hexapod motion to apply the prescribed sinusoidal movement.

4. Record measurement data during the experiment.

5. Manually stop the recording; the hexapod will automatically stop.

6. Stop turbine rotation and shut down the wind tunnel.

J. Rotational Wave Frequencies

J.1 Rotational Speed Range for VAWTs

The rotational speed of vertical-axis wind turbines (VAWTs) can vary widely depending on their design, size, and intended application. Values typically range from as low as 27 rpm up to 620.5 rpm, as shown in the literature overview provided in Table A1 of [64]. For the purposes of this study, a narrower range between 30 rpm and 150 rpm is selected for VAWTs, also due to Hexapod limitations.

To express this range in terms of rotational frequency, the following conversion is applied:

$$f = \frac{\text{rpm}}{60}$$

This yields a frequency range of approximately 0.5 Hz to 2.5 Hz.

J.2 Frequency Range of Swell Waves

Swell waves generally exhibit lower frequencies than locally generated wind-driven waves, as they originate from distant storm systems and travel long distances across the ocean. Frequencies between 0.04 and 0.10 Hz are typically associated with these low-frequency swell components, whereas frequencies in the range of 0.10 to 0.50 Hz correspond to higher-frequency wind sea components [65]. Since swell waves dominate in the open ocean, the frequency range of 0.04 to 0.10 Hz is adopted to represent typical ocean wave frequencies [66]. This range will therefore be used as the representative average wave frequency in this study.

J.3 Dimensionless Frequency Ratio

The dimensionless ratio between wave frequency and turbine rotation frequency, w^*, is given by:

$$w^* = \frac{f_{\text{wave}}}{f_{\text{rotor}}}$$

Using the ranges above:

$$f_{\text{wave}} \in [0.04, 0.10]\,\text{Hz}, \quad f_{\text{rotor}} \in [0.5, 2.5]\,\text{Hz}$$

The resulting range for w^* is approximately:

$$w^* \in [0.016, 0.2]$$

K. Blade Phase-Binned Torque

The flowchart of the Blade Phase-Binned TOrque calculated is shown in Figure K.1.

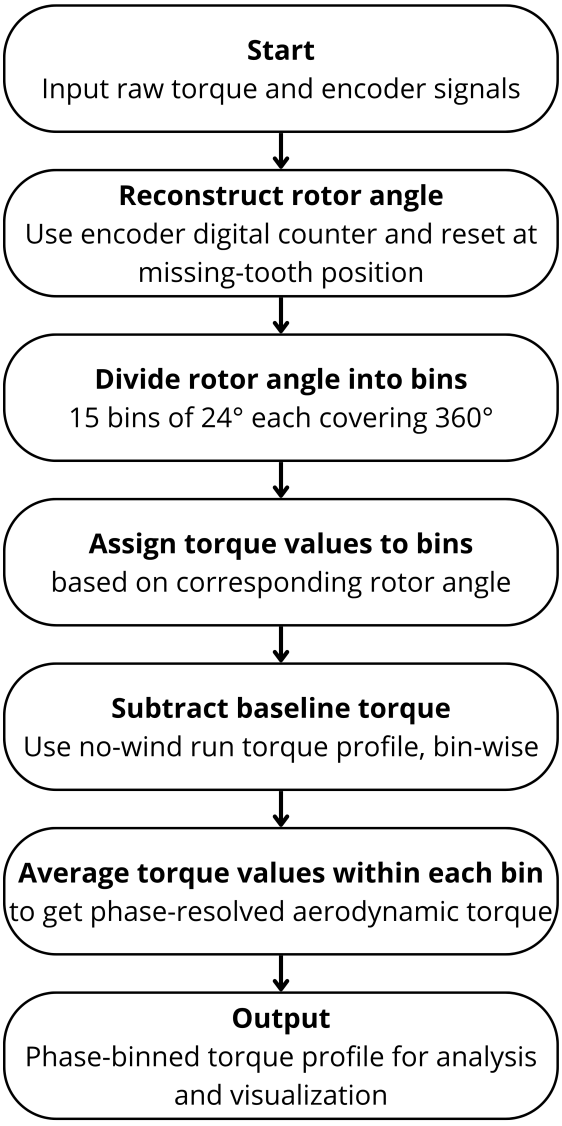

Figure K.1: Flowchart of the Blade Phase-Binned Torque calculation process.

L. Blade Azimuthal Offset

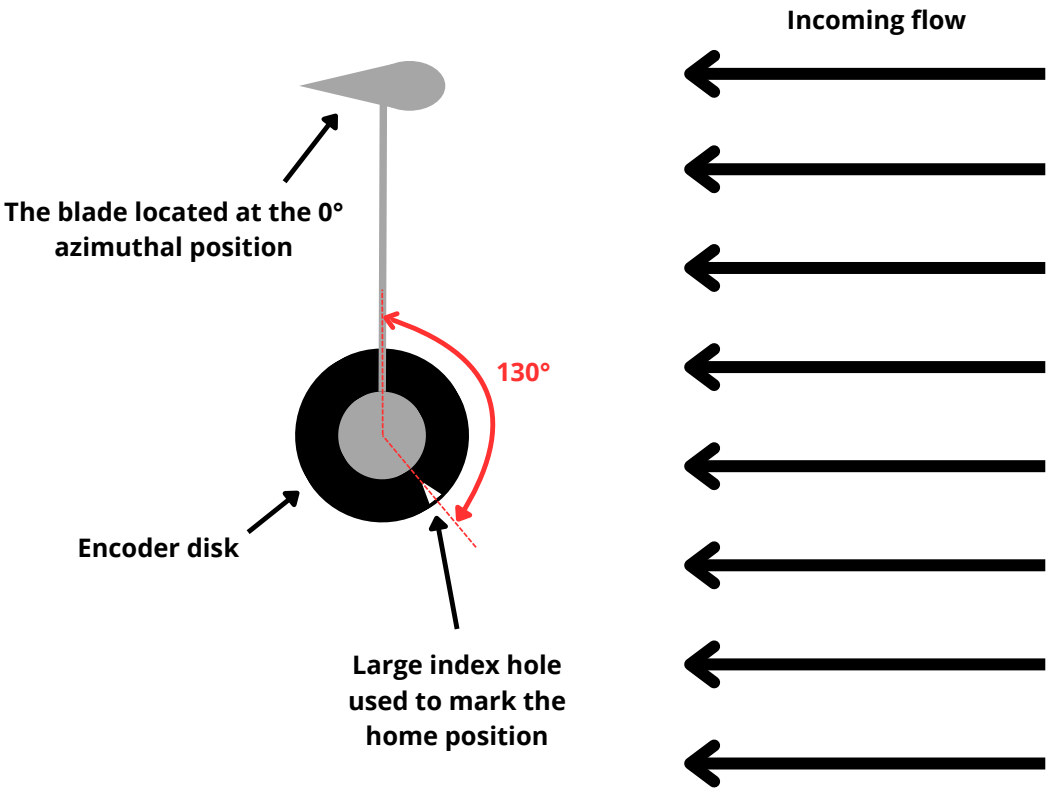

Figure L.1: Blade positioned at zero azimuthal angle (facing upstream) and encoder disk showing the large reference hole (home position). The encoder zero is offset by 130° relative to the blade zero, necessitating a phase correction during processing.

M. Sampling Pattern in Heatmaps

To assess the sampling density across blade and hexapod phase bins, the number of torque samples per bin was analyzed at two resolutions. The 15×15 binning reveals some bins with very low counts, while the coarser 10×10 binning ensures all bins have at least around 4000 samples, reducing potential noise from under-sampling.

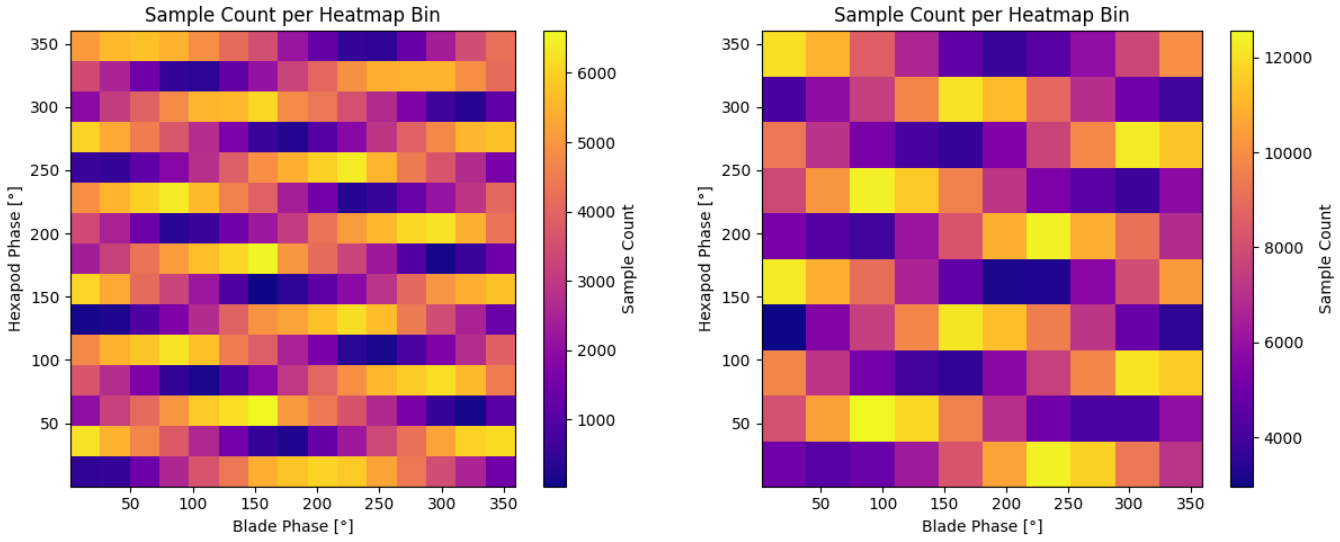

(a) Sample count at 15×15 bins

(b) Sample count at 10×10 bins

Figure M.1: Comparison of sampling density across blade and hexapod phase bins at different resolutions. The finer 15×15 binning suffers from sparse sampling in some bins, while the coarser 10×10 binning ensures more uniform coverage and reduces spurious fluctuations in torque estimates.

These patterns arise from the incommensurate frequencies of blade rotation and hexapod oscillation, producing quasi-periodic sampling and uneven phase-space coverage. The 10×10 binning reduces artifacts from under-sampled bins, but higher resolution maps may require longer or de-phased measurement runs for more uniform sampling.

N. Heatmaps for Different Tip Speed Ratios (10x10 boxes)

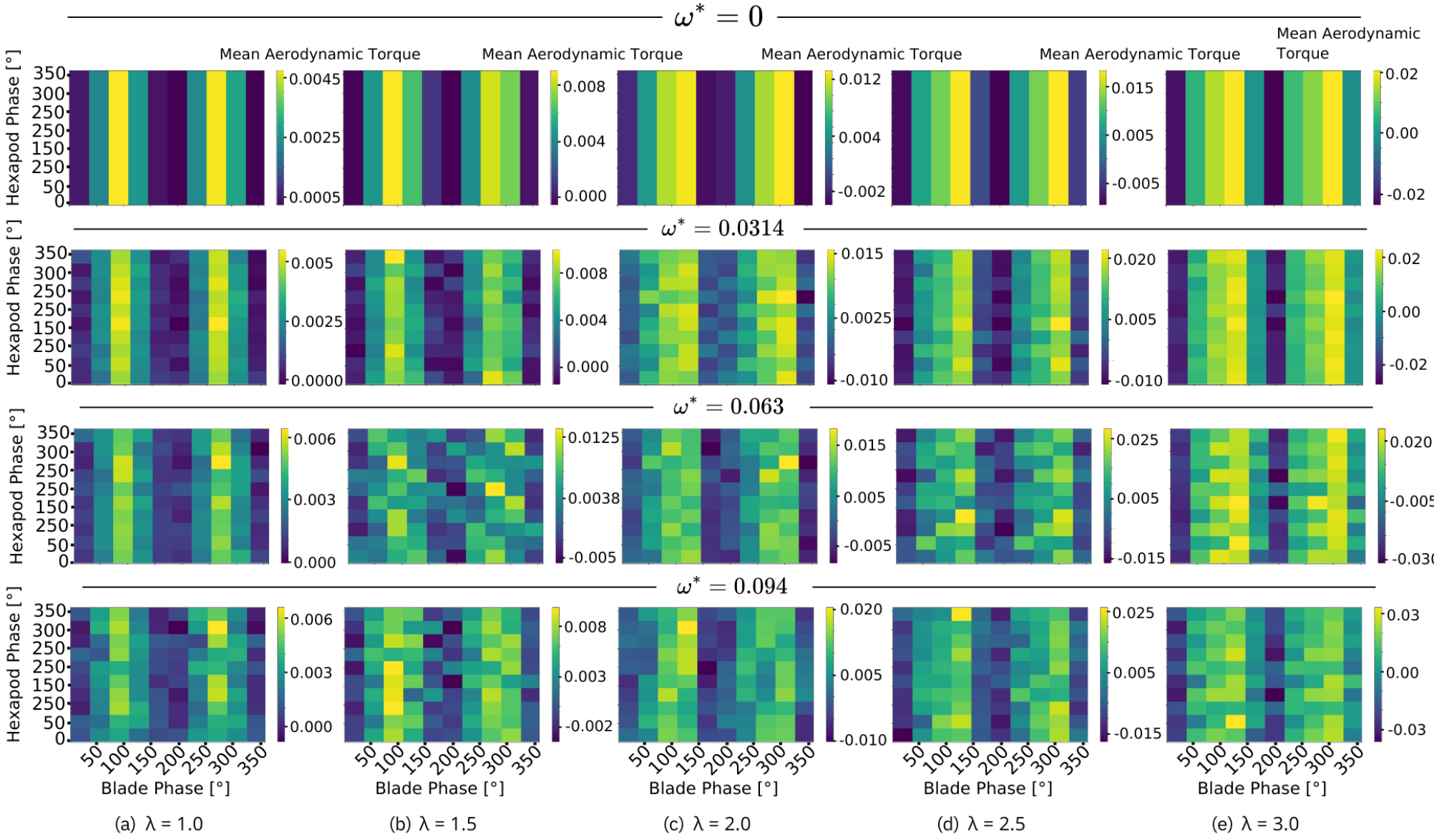

Figure N.1: Heatmaps of force distribution showing aerodynamic force variation over blade azimuth and hexapod phase, for different tip-speed ratios λ and normalized frequencies $\omega^* = 0,\ 0.0314,\ 0.063,\ 0.094$ under steady inflow conditions.

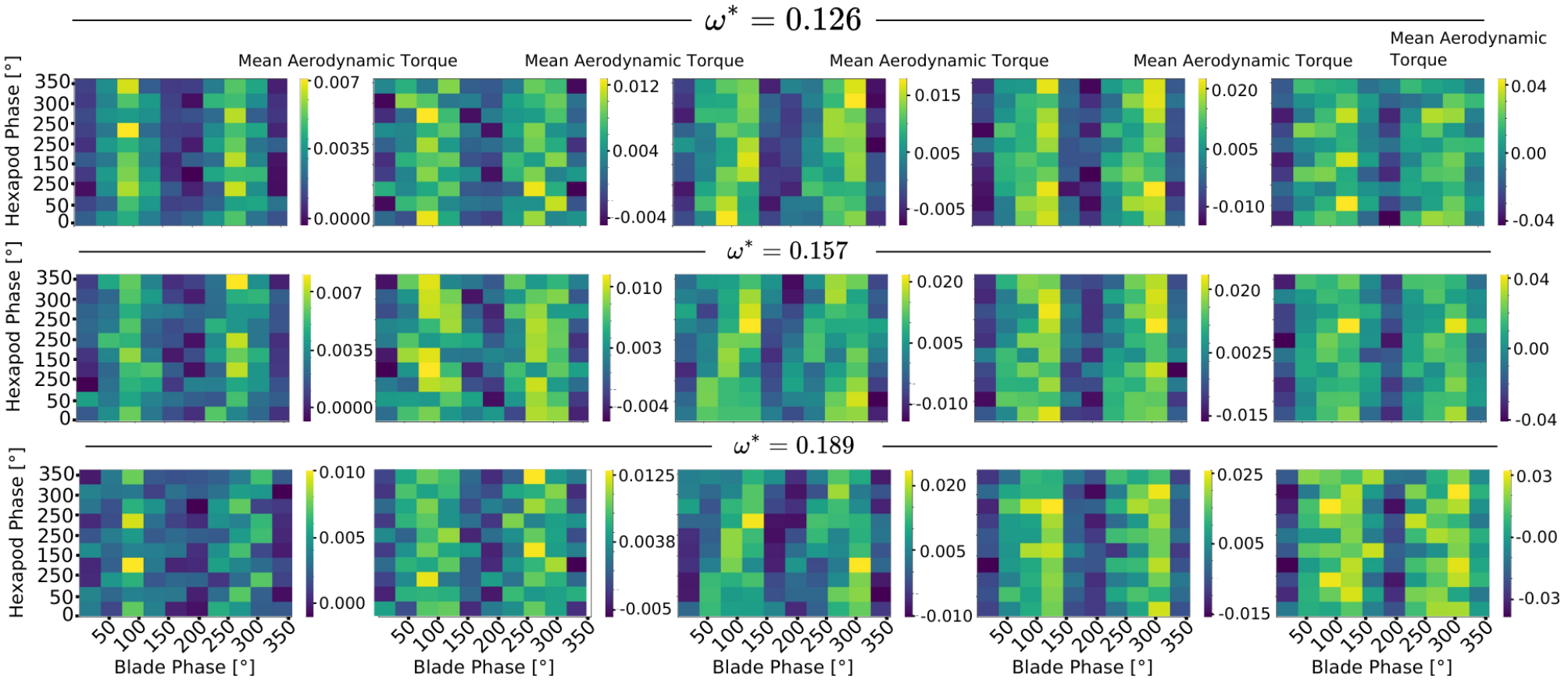

Figure N.2: Heatmaps of force distribution showing aerodynamic force variation over blade azimuth and hexapod phase, for different tip-speed ratios λ and normalized frequencies $\omega^* = 0.189,\ 0.157,\ 0.126$ under steady inflow conditions.